241

PRELIMINARY PERMEABILITY AND WATER-RETENTION DATA FOR NONWELDED AND BEDDED TUFF SAMPLES, YUCCA MOUNTAIN AREA, NYE COUNTY, NEVADA

U.S. GEOLOGICAL SURVEY

Open-File Report 90-569

Prepared in cooperation with the
NEVADA OPERATIONS OFFICE,
U.S. DEPARTMENT OF ENERGY, under
Interagency Agreement DE-AI08-78ET44802

8.3.1.2.2.3

PRELIMINARY PERMEABILITY AND WATER-RETENTION DATA FOR NONWELDED AND BEDDED TUFF SAMPLES, YUCCA MOUNTAIN AREA, NYE COUNTY, NEVADA

By Lorraine E. Flint, Raytheon Services of Nevada, and
Alan L. Flint, U.S. Geological Survey

U.S. GEOLOGICAL SURVEY

Open-File Report 90-569

Prepared in cooperation with the
NEVADA OPERATIONS OFFICE,
U.S. DEPARTMENT OF ENERGY, under
Interagency Agreement DE-AI08-78ET44802

Denver, Colorado
1990

U.S. DEPARTMENT OF THE INTERIOR

MANUEL LUJAN, JR., Secretary

U.S. GEOLOGICAL SURVEY

Dallas L. Peck, Director

For additional information
write to:

Chief, Yucca Mountain Project Branch
U.S. Geological Survey
Box 25046, Mail Stop 421
Denver Federal Center
Denver, CO 80225-0046

Copies of this report can
be purchased from:

U.S. Geological Survey
Books and Open-File Reports Section
Federal Center, Building 810
Box 25425
Denver, CO 80225-0425

CONTENTS

FIGURES

TABLES

CONVERSION FACTORS

Multiply	*By*	*To obtain*
bars	14.50	pounds per square inch (lb/in^2)
centimeter per second (cm/s)	0.03281	foot per second (ft/s)
centipoise (0.01 g/cm-s)	6.72E-4	pound per foot-second (lb/ft-s)
cubic centimeter (cm^3)	3.531E-5	cubic foot (ft^3)
cubic centimeter per second (cm^3/s)	3.531E-5	cubic foot per second (ft^3/s)
darcies (D)	1.05E-5	square foot (ft^2)
gram per cubic centimeter (gm/cm^3)	62.43	pound per cubic foot (lb/ft^3)
gram per liter (g/L)	0.008345	pound per gallon (lb/gal)
millidarcies (mD)	1.05E-8	square foot (ft^2)
millimeters (mm)	0.03937	inch (in.)
poise (1 g/cm-s)	6.72E-6	pound per foot-second (lb/ft-s)
radian per second (rad/s)	57.29	degree per second
square centimeter (cm^2)	0.001076	square foot (ft^2)

Temperature in degree Fahrenheit (°F) as follows:

$$°F = 9/5\ (°C) + 32$$

PRELIMINARY PERMEABILITY AND WATER-RETENTION DATA FOR NONWELDED AND BEDDED TUFF, YUCCA MOUNTAIN AREA, NYE COUNTY, NEVADA

By Lorraine E. Flint and Alan L. Flint

ABSTRACT

Measurements of rock-matrix hydrologic properties at Yucca Mountain, a potential site for a high-level nuclear waste repository, are needed to predict rates and direction of water flow in the unsaturated zone. The objective of this study is to provide preliminary data on intrinsic and relative permeability and moisture retention on rock core samples and to present the methods used to collect these data.

Four methods were used to measure intrinsic, or saturated permeability: Air, Klinkenberg, specific permeability to oil, and specific permeability to water. Two methods yielded data on relative permeability (gas-drive and centrifuge), and three methods (porous plate, centrifuge, and mercury intrusion porosimetry) were used to measure water-retention properties (matric potential compared to water-content curves). Standard measurements of grain density, bulk density, and porosity for the core samples were included.

Results of this study showed a large range of intrinsic permeability values among rock types and high variability within rock types. For example, permeability values for samples from the tuffaceous beds of Calico Hills (hereafter referred to as Calico Hills) were, on the average, three orders of magnitude smaller than all others. The four methods yield intrinsic permeability values that are different but are highly correlated (coefficient of determination greater than 0.94).

INTRODUCTION

Yucca Mountain, Nevada (fig. 1) is being studied as a potential site for a high-level radioactive waste repository. The U.S. Geological Survey is responsible for characterizing the hydrologic flow properties of the unsaturated zone matrix for the Matrix Hydrologic Properties program which is part of study plan entitled "Percolation of the Deep Unsaturated Zone."

The objective of this study is to present methods used for measuring intrinsic permeability, relative permeability, and water retention (matric potential compared to water content) on samples of rock core; and to provide data collected by these methods. Evaluations of these standard methods, most of which have been developed for application in the petroleum industry, eventually will be coupled with additional methods currently being developed for

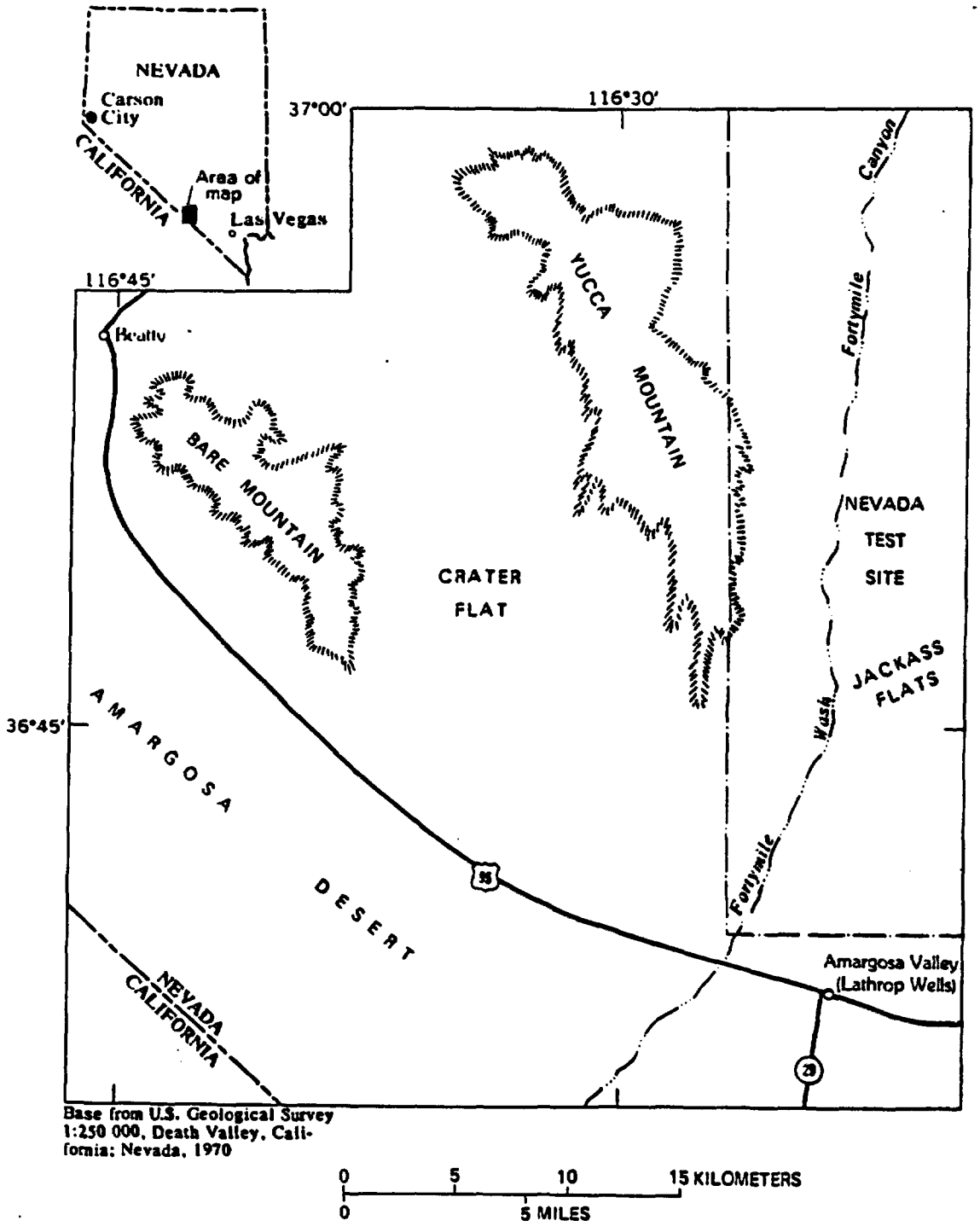

Figure 1.--Map of southern Nevada showing location of study area.

use in unsaturated-zone studies. The prototype methods are techniques or concepts commonly used in agriculture for soils, and the attempt is being made to adapt them for use on rock core samples. As part of this study, samples were collected from nonwelded and bedded tuffs. This report presents information on the permeability and water-retention characteristics of these samples.

Purpose and Scope

The purpose of this report is to provide preliminary data needed for the data bases used in the development of hydrologic models for the Yucca Mountain project. The methods used for collecting these data, standard laboratory-measurement techniques, also are presented in this report. Measurements of core grain density, bulk density, and porosity were made because these measurements are needed to define the characteristics of individual cores and supply information needed for the calculations of the hydrologic properties.

Core samples were obtained from nine boreholes (fig. 2) that penetrated various lithostratigraphic units of the late Tertiary Paintbrush Tuff and the Calico Hills (fig. 3). These were chosen for measurement to represent the possible range of permeability values that would be encountered. This would help define the methodology required to establish the upper and lower limits of permeability determination. The study was limited to samples of nonwelded tuffs that have large porosity values and relatively large saturated hydraulic-conductivity values compared to welded tuff.

Study Site and Sampling Locations

Yucca Mountain is an eastward-tilted volcanic plateau consisting of a thick sequence of ash-fall tuffs, pumice-fall tuffs, and reworked tuffs of late Tertiary age. Most of the ash-flow tuffs consist of welded, compositionally zoned, and compound cooling units, but nonwelded, compositionally homogeneous, or simple cooling units are also present. In addition, minor intervals of bedded tuffs are located between ash-flow tuff members or formations (Scott and Castellanos, 1984). Many of the tuffs also are diagenetically altered, containing zeolites, clays, and other minerals of secondary origin. In particular, smectite clays are closely associated with the zeolites in the altered tuffs. These clay minerals might interact with water and affect the permeability of the tuffs to water.

Seventy-three core samples were collected and analyzed. These samples were used to compare measurement methods and are listed in table 1. Samples were collected from boreholes (fig. 2) continuously cored using an air-coring method. Original cores were 6 cm in diameter and undercored to provide 2.5-cm-diameter vertical and horizontal cores for the matrix permeability tests. These vertical and horizontal cores were analyzed at Core Laboratories, Inc.[1], in Aurora, Colo. Two and five-tenths centimeter core samples were also analyzed by the U.S. Geological Survey petrophysics laboratory in Golden, Colo., and were undercored from adjacent 6-cm-diameter cores.

[1]The use of brand, trade, or firm names in this report is for identification purposes only and does not constitute endorsement by the U.S. Geological Survey, or impute responsibility for any present or potential effects on the natural resources.

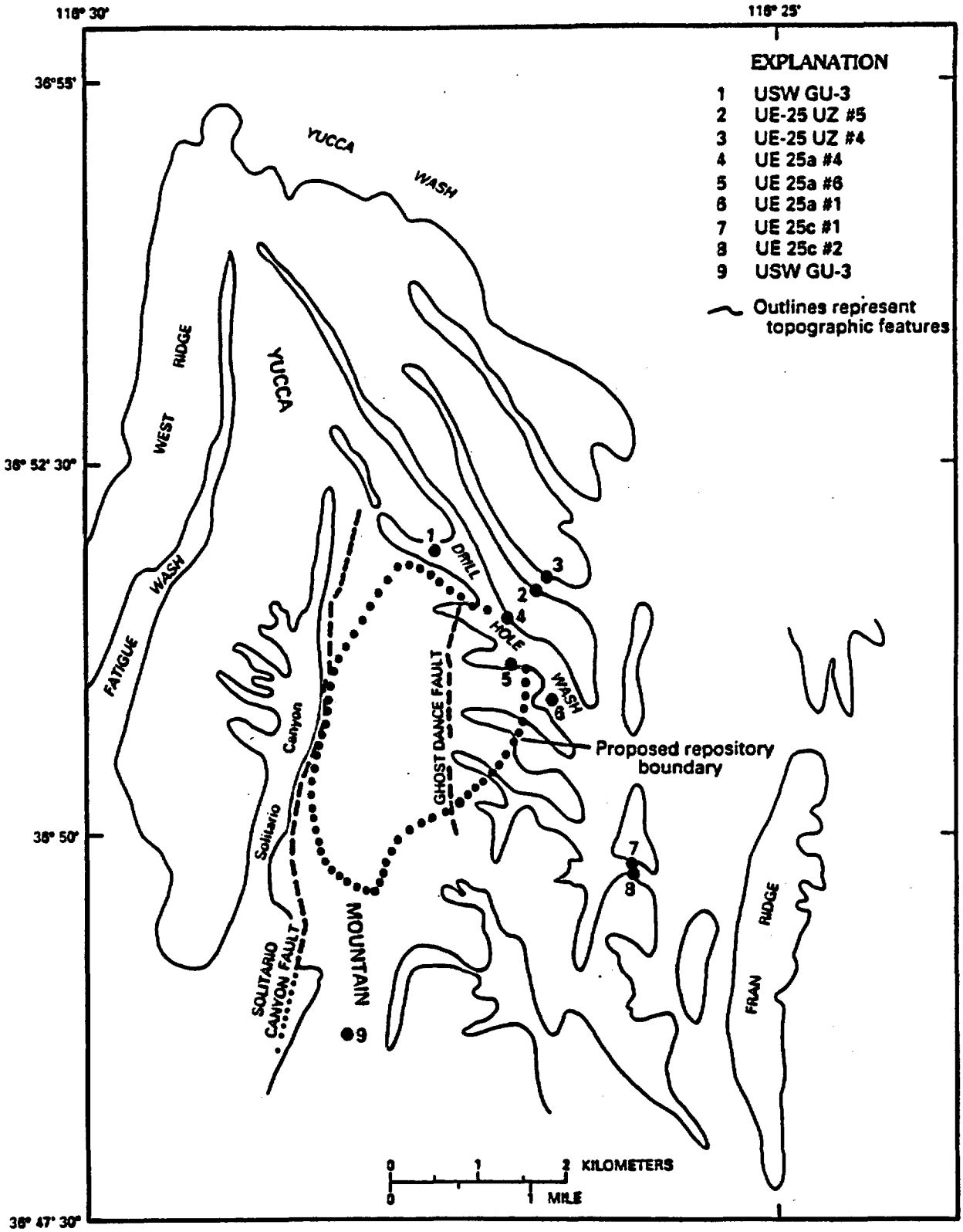

Figure 2.--Map of Yucca Mountain area showing location of boreholes from which core samples were obtained.

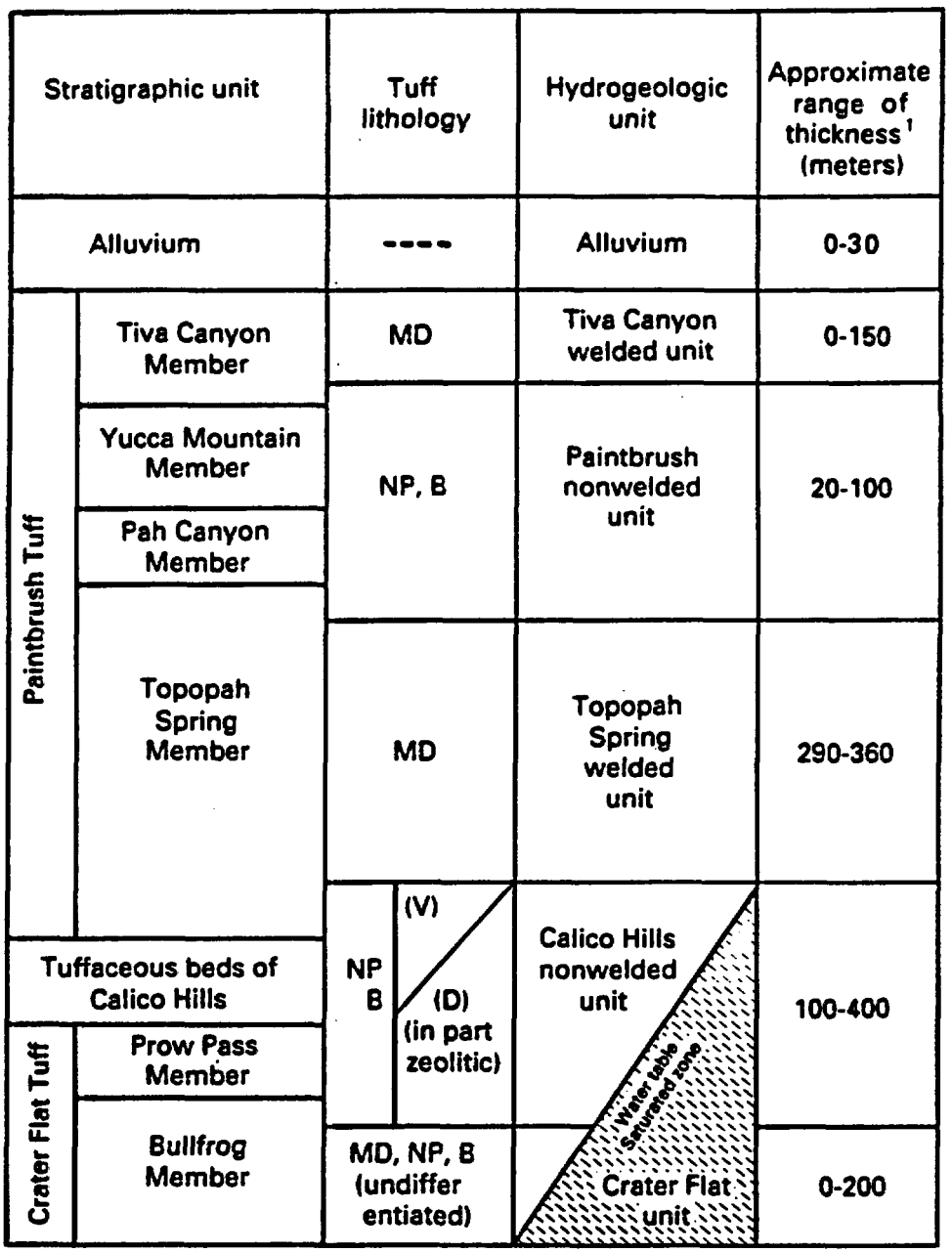

Figure 3.--Idealized stratigraphic column showing relations between stratigraphic (geologic) units, lithology, and hydrogeologic units (from Montazer and Wilson, 1984).

Table 1.--*Sample identifications, locations, and descriptions*

["H" in sample ID indicates horizontally oriented core sample. All other samples are vertical. "P" indicates samples measured by U.S. Geological Survey petrophysics laboratory, Golden, Colo. All other samples measured by Core Laboratories, Aurora, Colo. Individual sample labels represent individual core samples.]

Sample label	Well or borehole (fig. 2)	Depth interval (meters)	Geologic unit	Core matrix description
1U,1UH	USW GU-3	432.36-432.51	Calico Hills	Vitric
2U,2UH	USW GU-3	456.96-457.20	Calico Hills	Vitric
1P,1PH	UE-25c #2	405.08-405.20	Calico Hills	Devitrified, zeolitized
2P,2PH	UE-25c #2	426.17-426.48	Calico Hills	Devitrified, zeolitized
3P,3PH	UE-25c #1	462.17-462.50	Calico Hills	Devitrified, zeolitized
20A,20AP	USW G-1	487.86-488.02	Calico Hills	Zeolitized
12A,12AP	USW G-1	535.50-535.66	Calico Hills	Zeolitized
13A,13AP	USW G-1	546.29-546.45	Calico Hills	Zeolitized
14A,14AP	USW G-1	573.12-573.27	Calico Hills	Zeolitized
16A,16AP	USW G-1	589.03-589.18	Calico Hills	Zeolitized
15A,15AP	USW G-1	623.83-623.99	Calico Hills	Zeolitized
17A,17AH,17AP	USW G-1	632.80-632.98	Calico Hills	Zeolitized
18A,18AH,18AP	USW G-1	660.99-661.14	Calico Hills	Zeolitized
19A,19AH,19AP	USW G-1	439.95-440.10	Calico Hills	Zeolitized, partially argillic
8A,8AP	USW G-1	505.39-505.54	Calico Hills	Zeolitized, partially argillic
11A,11AP	USW G-1	518.16-518.31	Calico Hills	Zeolitized, partially argillic
1A,1AP	USW G-1	544.25-544.40	Calico Hills	Zeolitized, partially argillic
7A,7AP	UE-25a #1	431.96-432.15	Calico Hills	Devitrified, slightly zeolitized
9A,9AH,9AP	UE-25a #1	470.92-471.10	Calico Hills	Vitric
10A,10AP	UE-25a #1	549.10-549.25	Bedded-reworked tuff	
4A,4AP	UE-25a #6	40.75-40.87	Base of Tiva Canyon Member	Vitric
5A,5AP	UE-25a #4	43.16-43.25	Base of Tiva Canyon Member	Vitric
2A,2AP	UE-25a #1	65.07-65.23	Base of Tiva Canyon Member	Vitric, partially argillic
6A,6AP	UE-25a #4	47.15-47.46	Yucca Mountain Member	Vitric
3A,3AH,3AP	UE-25a #4	47.79-47.98	Yucca Mountain Member	Vitric
IV,IVP	UE-25a #6	50.81-50.93	Yucca Mountain Member	Vitric
5-2,5-2H	UE-25 UZ #5	42.43-42.58	Yucca Mountain Member	Vitric
5-1B	UE-25 UZ #5	38.44-38.62	Yucca Mountain Member	Vitric
4-4,4-4H	UE-25 UZ #4	72.97-73.12	Pah Canyon Member	Vitric
4-5,4-5H	UE-25 UZ #4	84.49-84.64	Pah Canyon Member	Vitric
5-6	UE-25 UZ #5	70.65-40.33	Pah Canyon Member	Vitric
5-7	UE-25 UZ #5	79.74-79.89	Pah Canyon Member	Vitric
4-6,4-6H	UE-25 UZ #4	93.94-94.06	Bedded-reworked tuff	
4-7,4-7H	UE-25 UZ #4	101.68-101.83	Bedded-reworked tuff	
5-1	UE-25 UZ #5	32.28-32.43	Bedded-reworked tuff	
5-1A	UE-25 UZ #5	34.29-34.44	Bedded-reworked tuff	
5-8	UE-25 UZ #5	96.80-96.93	Bedded-reworked tuff	
5-9	UE-25 UZ #5	105.55-105.64	Topopah Spring Member	Vitric

Definitions and Relations Between Properties

The following section defines the properties that were measured for the core samples. Relations between calculated and measured values also are discussed.

Core Physical Properties

Physical properties are those defining mass and volume relations. Grain density, ρ_s, is defined as the mass of the solids, M_s, divided by the volume of the solids, V_s. Dry bulk density, ρ_b, is M_s divided by the volume of the total sample, V_t (solids and pores together). Porosity is the relative pore volume in the soil or core, or the volume of air plus water divided by V_t. Porosity, ϕ, is calculated in cm^3/cm^3 as:

$$\phi = 1 - (\rho_b/\rho_s). \quad (1)$$

Porosity is the fractional volume of water and air that a given volume of soil or rock can accommodate.

Intrinsic Permeability and Saturated Hydraulic Conductivity

Permeability (or intrinsic permeability) is the capacity of a porous medium for transmitting fluid. Permeability is a property of the porous medium and its pore geometry alone, which includes factors such as size, shape, and distribution and tortuosity of pores. The measurement of intrinsic permeability is a measure of the fluid conductivity of the particular medium. If a porous body is not chemically inert and physically stable (nondeformable), there are matrix-water interactions such that fluid transmittance is best discussed in terms of hydraulic conductivity. Saturated hydraulic conductivity depends on the properties of the porous medium and the fluid. Permeability, k, is related to hydraulic conductivity, K, by:

$$k = K\eta/\rho g, \quad (2)$$

where η = dynamic viscosity of the fluid [Mass (M)/Length (L) * Time (T)],
ρ = density of the fluid (M/L^3), and
g = acceleration due to gravity (L/T^2).

Permeability measurements are necessary because attempts to establish empirical correlations between permeability and physical properties have been unsatisfactory. If permeability is determined using a specific liquid, such as the water occurring in the formation, then the specific intrinsic permeability to liquid and the hydraulic conductivity should be the same except for differences in the units of measurement. Standard techniques for the measurement of hydraulic conductivity on rock core are based on Darcy's law:

$$q = Q/A = -K\ (\Delta H/L), \quad (3)$$

where q = water flux (L/T),
Q = volumetric water flow rate (L^3/T),
A = cross-sectional area of core sample (L^2),
K = hydraulic conductivity (L/T),
ΔH = change in hydraulic head (L), and
L = core length (L).

Darcy's law is valid only for fluxes low enough to ensure that viscosity forces dominate within the pores and is assumed valid for the low fluxes measured in this study.

Combining equations 2 and 3 yields

$$k = - \frac{q\eta}{\rho g}(L/\Delta H). \quad (4)$$

The units of k are those of area; however, k is often given in units of darcies or millidarcies (1 darcy = 9.87E-3 cm^2 for water at 25 °C). For the above equations, it is necessary to express L in centimeters, A in square centimeters, ΔH in atmospheres, Q in cubic centimeters per second, η in centipoises, and g in centimeters per second squared in order to obtain k in darcies.

Relative Permeability

Given an incompressible porous medium at constant temperature and pressure, factors such as fluid density and viscosity, porosity, and pore geometry can be considered constant under saturated conditions. However, in partially saturated media, pore-geometry factors and water-filled porosity change and k becomes a function of water content, when only the properties of the porous media are considered. This functional relation defines the relative permeability, k_r. As the water content of a sample decreases, its permeability also decreases as a function of the water potential (Richards, 1931). When the viscosity and density of the fluid are considered, the function is called unsaturated conductivity. Darcy's law usually is assumed to be valid for unsaturated flow conditions, but it may not apply at very low flow rates (Hillel, 1982). For a rock sample, Darcy's law can be written:

$$q = -K(\theta)\, dH/dL, \quad (5)$$

where θ = volumetric water content (cm^3/cm^3), and
$K(\theta)$ = hydraulic conductivity as a function of water content.

Water-Retention Curves

Another important rock matrix property is the water-retention function, $\psi(\theta)$, which expresses the dependence of matric potential (ψ) as a function of water content (θ). Matric potential, ψ, is a measure of the energy with which water is held in pores. Measurements of $\psi(\theta)$ are needed independently of $K(\theta)$ to predict water flow in transient conditions. As the water content of a porous medium decreases, water is removed from progressively smaller pores, and the water potential becomes more negative. At equilibrium, water content

is a function of the water potential. Water-retention curves obtained for desorption (drying) and sorption (wetting) conditions are not identical because of hysteresis effects. Hysteresis is attributed to: (1) The contact angle of the wetting fluid being greater during sorption than during desorption; (2) the geometric nonuniformity of pores (the "ink-bottle" effect, Hillel, 1982); and (3) entrapped air that decreases the water content of newly wetted media (Hillel, 1982). The water contents at various water potentials are a function of pore-size distribution and geometry, which are a function of texture, porosity, compaction, and structure (Hillel, 1982). The finer the texture, the greater the water retention at any particular potential, and the more gradual the slope of the curve. In a matrix containing a high fraction of large pores, once these pores are emptied, little water remains within the matrix.

METHODS OF MEASUREMENT FOR PHYSICAL PROPERTIES, PERMEABILITY, AND WATER RETENTION

Physical Property Measurements

Measurements of the static physical properties of the core samples were made. These measurements were used in the calculations and interpretations of the flow properties.

Porosity

Porosity was determined using air (or gas) pycnometry. Pycnometry is based on Boyle's gas law, $P_1 V_1 = P_2 V_2$, where the subscripts refer to initial (1) and final (2) pressure (P) and volume (V) of gas. In a closed sample chamber, the volume of gas in the system, V_2, after P_1 is increased to P_2, may be determined with and without a core sample in the chamber. The volume of solids and liquids in the sample is [V_2 (without sample) - V_2 (with sample)]. If this value is subtracted from the sample bulk volume, the result is the volume of gas-filled pores in the sample.

Bulk Density

Bulk density, ρ_b, is determined by measuring the weight and volume of a core sample. This is dependent on an accurate measurement of undisturbed sample volume.

The volume of the core is computed from measurements of size and shape. The core is ovendried and weighed. Then it is coated with a water-repellent substance, weighed in air, then submersed again. By using Archimedes' principle of volume displacement:

$$\rho_b = \frac{\text{ovendried weight of sample} \times \rho_w}{(\text{weight in air} - \text{weight in water})}, \qquad (6)$$

where ρ_w = the density of water.

The value of ρ_b computed by equation 6 is corrected for the weight and density of the water-repellent coating using the method described in Blake and Hartge (1986).

Grain Density

Grain (or particle) density, ρ_p, is measured with a water pycnometer (specific-gravity flask). A pycnometer is a glass flask fitted with a ground-glass stopper that is pierced lengthwise and has a capillary opening. A known weight of ovendried, crushed, or sieved media (maximum grain size <2 mm) is added to the flask and then weighed. Water then is added to the pycnometer, the stopper is inserted, and the flask is placed under a vacuum to extract all air from the pores. The flask is reweighed, then cleaned, filled with water only, and reweighed. Calculations are made using:

$$\rho_p = \frac{a \times \rho_w}{a - (b-c)}, \tag{7}$$

where a = weight of ovendried sample,
b = weight of pycnometer with sample and water, and
c = weight of pycnometer with water,

and corrections are made for temperature (ASTM, 1985).

The submersion method uses Archimedes' principle in which surface water is lightly wiped from a vacuum-saturated core sample, the sample is weighed in air, and then suspended from a scale and reweighed while submersed. The calculation of ρ_p is the same as that given in equation 6. In addition, any one of the three properties--grain density, bulk density, or porosity--can be calculated using equation 1 if the other two properties are known.

Intrinsic Permeability Measurements

Preliminary measurements of permeability were made using four different methods. These methods were: (1) Air permeability, (2) Klinkenberg permeability, (3) specific permeability to oil, and (4) specific permeability to water.

Air Permeability

Air permeability, k_a, is the coefficient governing convective transmission of air through a porous medium in response to a total pressure gradient (Hillel, 1982). This measurement can provide information on the effective sizes and the continuity of air-filled pores representing permeability with no fluid-matrix interactions. Air permeability is a simple, inexpensive method. Both constant-pressure (steady-state) and falling-pressure (nonsteady-state) measurement techniques commonly are used. Samples are prepared by extracting any hydrocarbons using cool toluene and leaching salts that may be present from using methyl alcohol. The samples then are dried in a humidity-controlled oven at 40- to 45-percent relative humidity and 60 °C until sample weights stabilize. Cores are placed in a rubber or latex collar, gas is forced through the core, and air permeability, k_a, is calculated using the following equation (Corey, 1986):

$$k_a = - \frac{(\eta_a)(q_a)(dx)}{d(p_a)}, \qquad (8)$$

where η_a = dynamic viscosity of air (M/LT),

q_a = volume flux per unit area measured (L^3/L^2T), and

dp_a/dx = measured air pressure gradient (M/T^2L).

Klinkenberg Permeability

Klinkenberg permeability measurements were performed to evaluate the effect of nonideal gas behavior on air permeability measurements. Air permeability for a dry medium is always larger than fluid permeability in water-saturated conditions. Klinkenberg (1941) reported differences in permeability between measurements using gas as the flowing fluid and using nonwetting fluids. These variations were attributed to gas slippage. This effect can be evaluated by measuring k_a (permeability of air) at a range of mean pressures and plotting gas permeability versus the reciprocal of the mean pressure, and extrapolating the reciprocal pressure to 0 to estimate permeability at infinite pressures. The value of k_a found by extrapolation equals the value of k obtained with liquids that do not wet the solid matrix.

Applying the slip theory to simple capillary models of porous media, Klinkenberg (1941) derived the following relation between the measured permeability and the mean pressure:

$$k_l = k_a/(1+b/\bar{p}) = k_a - m\ (1/\bar{p}), \qquad (9)$$

where k_l = permeability of the medium to a single liquid phase component filling the pores of the medium, computed,

k_a = permeability of the medium to a gas component filling the pores of the medium, measured,

$\bar{p}$ = mean flowing pressure of the gas at which k_g was measured,

$b = m/k_l$, which is a constant for a given gas in a given medium,

m = slope of the curve of k_a versus reciprocal mean pressure.

The constant, b, increases with decreasing permeability, k_a, as slippage effects become proportionally greater for smaller openings (Amyx and others, 1960). The term $b/\bar{p}$ is derived from the observation that the phenomenon of slip occurs when the diameter of a pore approaches the mean free path of the gas molecules, which is inversely proportional to the mean pressure, $\bar{p}$, at the surface of the sample. This method has the disadvantage of requiring many measurements to calculate a final permeability value, which is time consuming and causes additional expense.

Specific Permeability to Oil

Specific permeability to oil, also a nonwetting fluid, is used to interpolate between Klinkenberg permeability measurements and water. Oil is used because it does not have the polar properties of water. Cores were pressure saturated with a light mineral oil that has a dynamic viscosity of approximately 1.5 centipoise at ambient conditions (room temperature and atmospheric pressure). Fully saturated cores were placed into a hydrostatic core holder at an effective overburden pressure of 67 bars and specific permeability to oil was obtained in the same manner as air permeability. Measurements were made at a confining pressure of 67 bars, which is representative of the in-situ conditions within the formation prior to removal of core. This step is needed because consolidation of the core due to in-situ overburden pressure may cause as much as a 60-percent reduction in the specific permeability to oil (Amyx and others, 1960, p. 95).

Specific Permeability to Water

Specific permeability to water is used to determine permeability to the formation water. Cores were pressure saturated with a simulated formation water containing approximately 276 ppm (parts per million) total dissolved solids. The simulated formation water was prepared based on analyses of Calico Hills water samples and contained the following constituents:

Constituent	Grams per liter
NaCl	0.01
$MgCl_2 \cdot 6H_2O$	.01
Na_2SO_4	.04
$CaCl_2$	.04
$NaHCO_3$	.19
KCl	.01

The viscosity of water with this composition is approximately 0.98 centipoise at ambient conditions. This is 50 percent lower than the viscosity of the oil used in the measurement of specific permeability to oil. Cores were placed into a hydrostatic core holder that maintained an effective overburden pressure of 67 bars, and specific liquid permeability was determined.

Relative Permeability Measurements

There are four types of methods by which relative permeability data can be obtained:

1. Direct measurement in the laboratory by a steady-state, fluid flow process;
2. Measurement in the lab by displacement or nonsteady-state processes;
3. Estimations of relative permeability from water-retention curves; and
4. Inferences from field performance data.

In this data report, we discuss only the first two types.

Steady-State Methods

Steady-state methods all essentially depend on the same technique. A core sample is enclosed in lucite or a pressurized rubber sleeve, and a high flow rate and a large pressure differential is imposed across the core sample. Both ends of the sample are in contact with porous disks or test sections, or both, of materials similar to the sample to minimize capillary "end effects."

End effects refer to pressure gradients occurring at the ends of the sample because of the saturation discontinuity at the outflow face of the sample. At this face, all fluids are at the same pressure; yet, within the pores adjacent to the sample face, the saturation of the wetting phase approaches 100 percent. A saturation gradient, therefore, is established in the fluid phase within the sample. For a theoretical development of the principles that cause end effects, see Amyx and others (1960, p. 193). End effects either must be accounted for or minimized in all methods used.

The phases--gas-oil, oil-water, or gas-water--are injected simultaneously at the inlet end. Most tests start with saturated samples, which are desaturated during the measurement. The fluids are introduced at a particular ratio, and flow through the core is continued until the outflow ratio is equal to the injected ratio, thus, establishing steady-state conditions.

Percent saturation can be measured directly by core resistivity or tensiometry. Gravimetric measurements of percent saturation can be made by weighing the core, and volumetric methods require measuring all fluids injected into and produced from the sample.

Once saturation has been determined, the relative permeability can be calculated. The injected ratio is increased, removing more of the wetting phase, until steady-state conditions again are reached. The process is repeated until a complete curve is obtained. A resaturation curve can be obtained by using a core saturated with a nonwetting phase, which provides direct measurements of hysteretic effects. None of the data included in this report were generated using steady-state methods; however, steady-state methods will be compared at a later date.

Nonsteady-State Methods

A nonsteady-state method involves a sample in which only one fluid enters the sample and two fluids are discharged. Such methods include gas drive and centrifuge.

Gas-drive method

The sample is saturated with the wetting phase, and gas is injected at one end of the core. In order to reduce the data, three conditions must be met: (1) The flow rate must be high enough, and the pressure gradient across the sample large enough, to make capillary end effects negligible; (2) the gas-saturation-pressure drop must be linear; and (3) the flow must be horizontal, the core must be small, and the test time short enough to prevent gravitational redistribution of fluid within the core. Gas injected and liquid produced over time are measured with pressures at inlet and outlet constant, as indicated in the following equation:

$$G = \frac{2\, G_i\, P_i}{V_p\, (P_i + P_o)}, \tag{10}$$

where G = cumulative injected gas as pore volume (cm^3/cm^3),
G_i = cumulative injected gas at inlet pressure (cm^3),
V_p = total pore volume of sample (cm^3),
P_i = inlet pressure ($dynes/cm^2$), and
P_o = outlet pressure ($dynes/cm^2$).

Cumulative fluid produced is plotted against fluid produced in pore volume. The slope of a fitted line represents the fraction of the total outflow volume from the sample that is liquid at any given time, which defines the following:

$$f = d(S_a)/dG, \tag{11}$$

where f = the fractions of the total outflow that is fluid, and
$d(S_a)/dG$ = the slope of the line of gas saturation.

The air-to-water permeability ratio, or relative permeability of gas, k_a, to fluid, k_w, can be calculated:

$$\frac{k_a}{k_w} = \frac{1-f}{f(\eta_a/\eta_w)}, \tag{12}$$

where η_a and η_w = viscosity values of the gas and fluid (water).

This particular value of the ratio applies at the gas saturation at the outflow face. Gas saturation at the outflow face, o, is:

$$(S_a)_o = S_a - Gf. \tag{13}$$

Thus, relative permeability ratios are obtained as a function of saturation. Actual values of relative permeability require that one of the phases be measured for a saturated permeability value. The detailed calculations are discussed in Amyx and others (1960, p. 190).

In comparison with steady-state methods described above, the gas-drive method uses considerably less apparatus, is very simple, and can be performed rapidly on small core samples. A disadvantage is that it cannot determine relative permeability ratios at low values of gas saturation. End effects are not important due to the high pressure gradients created across the core sample (Owens and others, 1956).

Centrifuge method

Relative permeability can be determined by a transient outflow centrifuge method (Hagoort, 1980; Van Spronsen, 1982). An advantage of this method is the ability to obtain values at low gas saturations. First, cores are pressure saturated with the simulated formation water. The core then is placed into a centrifuge and spun at 11,750 rpm. The quantity of fluid produced versus time is monitored continuously for approximately 275,000 seconds. The production of fluid as a function of time usually is measured by taking photographs of a transparent graduated collection tube using stroboscopic illumination. The volume of water for each sample is used to calculate the values of unsaturated hydraulic conductivity. These values then are converted to relative permeability by inverting equation 2, thereby taking into account the viscosity and density of the formation water and acceleration of gravity. Example calculations are shown in the section on measuring water-retention curves with a centrifuge.

The capillary end effects can be minimized by using a high centrifugal acceleration; the centrifugal force on the liquid phases still will be small compared with the capillary forces on a pore scale. If the centrifugal forces on a pore scale become important, the end points and the shape of the relative permeability curve change (Van Spronsen, 1982).

The advantage of the centrifugal method is that it works independently of matric potential gradients. This can be important for unsaturated porous media or rocks where matric potential gradients can cause gradients of water content and conductivity, thus, introducing an often undesirable complexity (Nimmo and others, 1987).

Methods also have been developed to measure unsaturated conductivity using steady-state outflow of water from an unsaturated sample spinning in a centrifuge (Nimmo and others, 1987; Conca and Lane, 1988).

Water-Retention Measurements

The quantity of water remaining in a porous medium at a specified water content is a function of the sizes and volumes of the water-filled pores and, hence, is a function of the matric potential. Water-retention relations, expressing the dependence of saturation on matric potential, are needed to establish a known matric potential for each core sample matrix of interest.

Porous Plate Methods

Several methods involve using a porous plate, a type of membrane through which water but not air will flow owing to pressure or vacuum. Such methods include vacuum, pressure extractor, and submersible-pressure-outflow cell. Porous plates usually are made of ceramic materials with pore-size distributions selected to retain water over various pressure or vacuum ranges. The smaller the pores, the higher the pressure required, and the longer it takes to reach matric potential equilibrium.

Vacuum

In the vacuum method, a water-saturated core sample is placed in contact with a water-saturated porous plate to establish a continuous water column. The upper end of the sample is at atmospheric pressure. A pressure differential can be created across the core sample and controlled by applying a vacuum at the bottom of the porous plate by using a vacuum pump or a hanging water column. The pressure differential forces water out of the sample until a known pressure is established, which, at equilibrium, is the matric potential, ψ, in the sample. The water released from the sample is measured, or the sample is weighed to determine water content, θ. The disadvantage of this method is that the lower value of matric potential is limited to about -0.8 bar (Klute, 1986).

Pressure extractor

In a pressure extractor, the sample is placed on a porous plate with a sheet-rubber backing. An outlet through the plate keeps the bottom of the plate and bulk water at atmospheric pressure. The range of matric potential for pressure plates is determined by the safe working pressure of the chamber and the pressure differential at which air will bubble through the pores in the plate. Once water is pushed out of the saturated samples and allowed to equilibrate at a given pressure, the samples are removed from the chamber and gravimetric water content is determined. Samples and plates are resaturated to determine additional $\psi(\theta)$ points in order to construct the water-retention curve. Disadvantages of this method include problems with determining when equilibrium is established. There also are problems because of changes in core water potential when pressure is released from the extractor as a result of backflow of water into the core from the plate or as a result of production of air bubbles in the core, or both, causing redistribution of water into larger size pores (Klute, 1986).

Submersible-pressurized-outflow cell

A porous plate method that helps to solve some of these problems is the submersible-pressurized-outflow cell (SPOC) (Constantz and Herkelrath, 1984). This method encloses a single sample on a porous plate in a cell with a pressure inflow port on top connected to a quick-release compression fitting. Water outflow is through the bottom of the plate. The cell is then suspended in a constant-temperature water bath and pressure is applied to remove water from the sample. The entire cell is weighed, suspended in water, while hanging from the bottom of a scale. The difference in weights is equal to the quantity of water lost. Equilibrium can be determined by cessation of water loss, and samples are weighed without pressure loss eliminating backflow and bubble formations. Sorption measurements, which are complicated by the presence of air under the plate in a pressure extractor that tends to break the continuous water columns, are easily accomplished in a SPOC because water flows directly into the sample through the porous plate that is in contact at all times with the water in the bath.

Centrifugation

Saturated core samples are placed on a permeable, wet membrane and located in a holder in a centrifuge rotor. The water is expelled from the core at increasing rates of rotation and is viewed in a chamber in the holder below the core through a port with a stroboscope during centrifuge action. It is essential to take readings of expelled water volume during rotation and to increase the rate of rotation without any decrease, in order to prevent redistribution of the fluid in the sample. The volume of water remaining in the sample then is divided by the total pore volume of the samples. Calculations of the water-retention curve are as follows:

1. The extracted volume reading, V (at each angular velocity) is converted to average saturation for the core, S_c, using the total pore volume of the core, V_{tot}, by:

$$S_c = 1 - (V/V_{tot}). \tag{14}$$

2. Angular velocity, ω, is converted to pressure, P, by:

$$P = [(\rho_w - \rho_g)\omega^2/2] \cdot (re^2 - r^2), \tag{15}$$

where ρ_w = density of water (g/cm),
ρ_g = density of gas (g/cm),
ω = angular velocity (radians/second),
r = distance from the center of rotation (cm), and
r_e = radius of the core bottom (cm), calculated as

$$\omega(\text{rad/sec}) = \text{RPM} \cdot \frac{2\pi(\text{rad/rev})}{60(\text{sec/min})}. \tag{16}$$

3. PS_c is plotted against P. Assuming capillary pressure is equal to P, then the water-retention curve can be generated from this plot.

4. The water-retention curve is derived from the curve in step 3 using:

$$\psi(\theta) = \frac{d(PS-c)}{dP}. \tag{17}$$

Good agreement between centrifugation and porous plate methods has been found by Slobod and others (1951) and by Hoffman (1963). The porous plate method may require weeks, whereas the centrifuge method may require only a few days to complete. The centrifuge generally is nondestructive and provides reproducible results. Both desorption and sorption curves can be produced (Skuse, 1984).

Mercury Intrusion Porosimetry

Because mercury is a nonwetting liquid, it will not enter pores by capillary action. Mercury can, however, be forced into pores by intruding it under the application of external pressure. The size of the pores that are intruded is inversely proportional to the applied pressure (ASTM, 1985):

$$d = (4\gamma\,|\cos\alpha|)/P, \tag{18}$$

where d = diameter of the pore (cm),
γ = surface tension of mercury (dynes/cm^2),
α = contact angle of mercury with the surface of the porous media (°), and
P = absolute pressure (dynes/cm^2).

The volume of mercury injected at each pressure determines the nonwetting-phase saturation. This is a very fast method that was developed to accelerate the process of water-retention determination. Disadvantages of this method are (1) the difference in wetting properties between mercury and water, and (2) the permanent loss of the core sample (Amyx and others, 1960).

Amyx and others (1960) claim that the porous plate method is superior to other methods because it is closer to simulating actual wetting conditions and, hence, is used as a standard method for comparison. This idea may have merit for several reasons. The contact angle for mercury against rock surfaces is 140°, while that of water is approximately 0°, and the ratio of mercury capillary pressure to water-air capillary pressure is about 5 (Amyx and others, 1960). Purcell (1949) showed graphically that the agreement of data between the two methods is good when corrected by this ratio. However, a question exists as to whether the contact angle can be used as the only basis of the pressure ratio [as used in mercury porosimetry standard methods in ASTM (1985)]. The mean curvature of an interface in rock is a unique function of fluid saturation defining the pressure ratio as 6.57 rather than 5 (Amyx and others, 1960). Brown (1951) reported the correlating factor between the two methods to be a function of the porous medium and defined the ratio as 7.5 for sandstone or 5.8 for limestone. Therefore, uncertainty about the value of the correlating factor between mercury and water wetting properties introduces doubt regarding the accuracy of the method.

RESULTS OF PHYSICAL PROPERTY, PERMEABILITY, AND WATER-RETENTION MEASUREMENTS

The methods described were used to measure properties of 73 rock core samples. There were both vertically and horizontally oriented samples from many of the borehole depth intervals.

Core Physical Properties

Measured values of porosity, grain density, and bulk density for core samples are summarized in table 2. Measurements for each property were made at the U.S. Geological Survey petrophysics laboratory in Golden, Colo. (USGS-P); or at Core Laboratories, Inc., in Aurora, Colo. (CLI), or both. USGS-P used both Archimedes' principle and air pycnometry to measure porosity and grain density, while CLI used only helium pycnometry. Bulk density was measured by USGS-P using Archimedes' principle and the caliper measurement technique.

Intrinsic Permeability

Measured values for saturated permeability using the air permeability method and three types of liquid permeability methods are listed in table 3. Air permeability values were obtained using helium pycnometry. Permeability to specific liquid was measured using the simulated formation water method (detailed in the "Methods" section) and hence referred to as specific permeability to water. The entry "0.00" indicates that the permeability was <0.01 millidarcies (mD). It was suggested by CLI that sample 2U may have developed a fracture during testing and the measurement values may be considered invalid. It also may be possible that the entire original section of core from which the samples came may have been fractured. For this reason, data from 2U, 2UH, and 2UP were not used in analyses of permeability.

Relative Permeability and Unsaturated Hydraulic Conductivity

Relative permeability and the corresponding calculated unsaturated hydraulic-conductivity values are listed in table 4 for 10 samples; 9 samples were analysed using the centrifuge method; and 3 of these 9 samples, plus an additional sample, were analyzed using the gas-drive method. The conversions for the unsaturated hydraulic conductivity calculations are as follows:

Saturated hydraulic conductivity (cm/s) = saturated permeability (mD) × 980 (cm/s) × 9.87×10^{-12}/0.01002 (poise); unsaturated hydraulic conductivity (cm/s) = [saturated permeability (mD) × relative permeability fraction] × 9.87×10^{-12} × 980 (cm/s)/0.01002 (poise). Related graphical representations are shown in appendix I.

Water-Retention Curves

Water retention, or matric potential versus water content, is listed in tables 5 and 6. Volumetric water content at various matric potentials for 11 core samples is listed in table 5. All tests were run by CLI. Porous plate (pressure plate) values were obtained using a *pressure extractor*. Water-retention values listed in table 6 were obtained by USGS-P using *mercury intrusion porosimetry* on nine vertical core samples. Related graphical representations of water-retention data are shown in appendix II.

Table 2.--*Physical properties of core samples: Porosity, grain density, and bulk density*

[All porosity and grain density measured by gas pycnometry unless otherwise noted; A, value obtained by Archimedes' principle; M, volume of sample measured by caliper and calculated; cm^3/cm^3, cubic centimeter per cubic centimeter; g/cm^3, grams per cubic centimeter; --, no data]

Sample label	Porosity (cm^3/cm^3)	Grain density (g/cm^3)	Bulk density (g/cm^3)
1U	0.363	2.30	--
	.364	2.30	
1UH	.387	2.30	--
	.391	2.32	
2U	.351	2.29	--
	.354	2.30	
2UH	.381	2.24	--
1P	.145	2.30	--
	.149	2.30	
1PH	.141	2.31	--
2P	.227	2.25	--
	.231	2.25	
2PH	.266	2.25	--
3P	.362	2.32	--
	.335	2.30	
	.336	2.31	
3PH	.347	2.30	--
20A	.212	2.29	--
	.228	2.21	
20AP	.260 A	2.29 A	1.69 A
			1.71 M
12A	.271	2.29	--
12AP	.309 A	2.38 A	1.64 A
			1.65 M
13A	.333	2.29	--
13AP	.334 A	2.35 A	1.56 A
			1.58 M
14A	.324	2.29	--
14AP	.349 A	2.21 A	1.44 A
			1.44 M
16A	.364	2.23	--
16AP	.333 A	2.23 A	1.49 A
			1.49 M
15A	.284	2.28	--
15AP	.266 A	2.24 A	1.65 A
			1.65 M
17A	.304	2.34	--
	.266	2.31	
	.280	2.26	
17AH	.276	2.25	--
17AP	.274 A	2.29 A	1.66 A
			1.67 M

Table 2.--*Physical properties of core samples: Porosity, grain density, and bulk density*--Continued

Sample label	Porosity (cm^3/cm^3)	Grain density (g/cm^3)	Bulk density (g/cm^3)
18A	0.278	2.30	--
	.248	2.28	
18AH	.236	2.29	--
18AP	.275 A	2.32 A	1.68 A
			1.70 M
19A	.363	2.35	--
	.272	2.25	
19AH	.283	2.22	--
19AP	.327 A	2.32 A	1.56 A
			1.57 M
8A	.299	2.26	--
8AP	.331 A	2.32 A	1.55 A
			1.57 M
11A	.313	2.32	--
11AP	.326 A	2.33 A	1.57 A
			1.58 M
1A	.228	2.61	--
1AP	.277	2.58 A	1.87 M
7AP	.287 A	2.27 A	1.62 A
	.254	2.27 A	1.63 M
9A	.285	2.35	--
	.282	2.32	
9AH	.271	2.31	--
9AP	.297 A	2.35 A	1.66 A
	.274	2.29	1.67 M
10A	.316	2.42	--
	.311 A	2.36 A	1.62 A
	.291	2.31	1.64 M
4AP	.431 A	2.41 A	1.37 A
	.423	2.40	1.38 M
5A	.414	2.34	--
	.416	2.33	
	.427	2.36	
5AP	.440 A	2.36 A	1.33 A
	.441	2.33	1.30 M
2A	.510	2.34	--
	.490	2.33	
	.473	2.31	
	.485	2.34	
2AP	.504 A	2.35 A	1.17 A
	.502	2.34	1.16 M

Table 2.--*Physical properties of core samples: Porosity, grain density, and bulk density*--Continued

Sample label	Porosity (cm^3/cm^3)	Grain density (g/cm^3)	Bulk density (g/cm^3)
6A	0.364	2.33	--
		2.35	
6AP	.437 A	2.30 A	1.30 A
	.454	2.32	1.26 M
3A	.443	2.33	--
	.441	2.34	
	.443	2.34	
3AH	.440	2.33	--
3AP	.440 A	2.33 A	1.31 A
	.454	2.32	1.27 M
1V	.436	2.44	--
	.405	2.32	
1VP	.419 A	2.34 A	1.36 A
	.418	2.32	1.35 M
5-2	.321	2.28	--
	.311	2.26	
	.326	2.29	
5-2H	.320	2.25	--
5-1B	.423	2.33	--
4-4	.399	2.37	--
	.408	2.40	
4-4H	.412	2.36	--
4-5	.472	2.37	--
	.482	2.40	
4-5H	.470	2.35	--
5-6	.464	2.25	--
5-7	.455	2.34	--
4-6	.281	2.28	--
	.287	2.29	
4-6H	.336	2.24	--
4-7	.355	2.27	--
	.362	2.29	
4-7H	.408	2.42	--
5-1	.396	2.31	--
5-1A	.411	2.35	--
5-8	.345	2.33	--
5-9	.287	2.26	--
	.308	2.23	
	.289	2.25	

Table 3.--*Intrinsic permeability values for core samples*

[All values in millidarcies; --, no data]

Sample label	Air permeability	Klinkenberg permeability	Specific permeability to nonpolar oil	Specific permeability to water
1U	0.17	0.24	--	0.01
	.07			1.10
	2.80			1.30
1UH	1.20	.26	0.35	.22
			.25	.27
2U	.35	30.50	--	.01
	.29			1.70
	68.00			47.00
2UH	46.00	--	--	--
2UP	--	.35	37.00	9.90
1P	.00	.00	--	.00
	.02			.00
	.01			
1PH	.00	--	--	--
2P	.22	.03	--	.03
	.18	.04		.04
	.09			.03
2PH	.30	.05	.02	.01
3P	.26	.02	--	.01
	.36	.02		.04
	.53			.05
	.20			
3PH	.25	.20	.05	.03
20A	.02	.03	--	.00
	.47			.00
20AP	--	--	--	.07
12A	.18	.04	--	.00
12AP	--	--	--	.02
13A	.10	.02	--	.00
13AP	--	--	--	.02
14A	.22	.01	--	.01
14AP	--	--	--	.03
16A	.20	.02	--	.02
16AP	--	--	--	.03
15A	.18	--	--	.01
15AP	--	--	--	.02

Table 3.--*Intrinsic permeability values for core samples*--Continued

Sample label	Air permeability	Klinkenberg permeability	Specific permeability to nonpolar oil	Specific permeability to water
17A	0.06		--	0.01
	.17	0.03		
	.08			
17AH	.09	.02	0.01	.01
17AP	--	--	--	.02
18A	.03	.03	--	.00
	.07			
18AH	.01	.01	.00	.01
				.00
18AP	--	--	--	.006
19A	.19	--	--	.00
	.14	.05		.00
19AH	.28	.04	.02	.01
			.07	
19AP	--	--	--	.02
8A	.07	--	.00	.00
11A	.06	.02	--	.00
11AP	--	--	--	.02
1A	.23	.04	--	.00
7AP	--	--	--	.06
9A	.05	.01	--	.00
				.00
9AH	.04	.01	.00	--
9AP	--	--	--	.00
				.00
10A	.09	.02	.00	.00
	.12	.01		
		.05		
10AP	--	--	--	.01
				.005
4AP	--	--	--	.02
				.00
5A	132.00	--	--	41.00
	142.00			100.00
5AP	129.00	--	--	159.00
2A	290.00	--	--	64.00
	264.00			198.00
	368.00			192.50
	374.00			129.50

Table 3.--*Intrinsic permeability values for core samples*--Continued

Sample label	Air permeability	Klinkenberg permeability	Specific permeability to nonpolar oil	Specific permeability to water
6A	--	--	--	242.40
3A	267.00	--	--	90.00
	247.00			195.00
3AH	293.00	312.00	282.00	--
	315.00			
3AP	--	--	--	220.00
				287.50
IV	30.00	22.00	--	14.00
	34.00			17.00
IVP	--	--	--	19.20
5-2	5.50	3.21	--	2.10
	5.30			
	5.20			
5-2H	9.50	9.16	6.90	3.30
5-1B	117.00	90.00	--	.76
4-4	2.30	1.26	--	.86
4-4H	4.80	3.52	3.40	1.90
4-5	90.00	33.00	--	20.00
	92.00	89.00		51.00
	93.00			
4-5H	111.00	111.30	94.00	74.00
5-6	35.00	33.00	--	20.00
5-7	32.00	29.00	--	.69
4-6	53.00	58.00	--	29.00
	78.00			
	152.00			
4-6H	29.00	23.40	19.00	8.70
4-7	21.00	21.00	--	.46
	17.00			
4-7H	27.00	3.00	--	2.20
5-1	42.00	43.00	--	14.00
	45.00			
5-1H	--	--	--	2.20
5-1A	247.00	210.00	--	.67
5-8	2.40	.60	--	.46
5-9	223.00	308.00	--	140.00
	362.00			184.00
	350.00			

Table 4.--*Relative permeability and corresponding calculated unsaturated hydraulic-conductivity values*

[mD, millidarcies; cm/s, centimeter per second; relative permeability (fraction), relative permeability to water, fraction]

Sample label	Hydraulic conductivity saturated (cm/s)	Permeability saturated (mD)	Percent saturation	Relative permeability (fraction)	Hydraulic conductivity unsaturated (cm/s)
			GAS-DRIVE METHOD RESULTS		
5-2	5.31×10^{-6}	5.5	100.0	1.0	5.31×10^{-6}
			88.8	.124	6.58×10^{-7}
			87.0	.088	4.67×10^{-7}
			85.9	.069	3.66×10^{-7}
			84.9	.056	2.97×10^{-7}
			82.7	.033	1.75×10^{-7}
			80.7	.019	1.01×10^{-7}
			79.0	.013	6.90×10^{-8}
			77.7	.0084	4.46×10^{-8}
			76.4	.0050	2.65×10^{-8}
			74.7	.0035	1.86×10^{-8}
			73.2	.0019	1.01×10^{-8}
			71.8	.00078	4.14×10^{-9}
			70.9	.00039	2.07×10^{-9}
3P	2.90×10^{-8}	.03	100.0	1.0	2.90×10^{-8}
			87.8	.541	1.57×10^{-8}
			83.7	.421	1.22×10^{-8}
			78.7	.300	8.69×10^{-9}
			72.3	.162	4.69×10^{-9}
			68.4	.097	2.81×10^{-9}
			65.6	.063	1.82×10^{-9}
			63.2	.040	1.16×10^{-9}
			61.4	.026	7.53×10^{-10}
			59.9	.017	4.92×10^{-10}
			58.3	.0097	2.81×10^{-10}
			57.2	.0057	1.65×10^{-10}
			56.4	.0036	1.04×10^{-10}
IV	1.75×10^{-5}	18.1	100.0	1.0	1.75×10^{-5}
			89.4	.075	1.31×10^{-6}
			88.1	.052	9.09×10^{-7}
			87.4	.043	7.51×10^{-7}
			86.8	.037	6.46×10^{-7}
			86.2	.031	5.42×10^{-7}
			84.8	.019	3.32×10^{-7}
			83.5	.012	2.10×10^{-7}
			82.7	.0088	1.54×10^{-7}
			81.5	.0062	1.08×10^{-7}
			79.3	.0022	3.84×10^{-8}
			78.4	.0015	2.62×10^{-8}
			76.9	.00066	1.15×10^{-8}
			76.1	.00038	6.64×10^{-9}

Table 4.--*Relative permeability and corresponding calculated unsaturated hydraulic-conductivity values*--Continued

Sample label	Hydraulic conductivity saturated (cm/s)	Permeability saturated (mD)	Percent saturation	Relative permeability (fraction)	Hydraulic conductivity unsaturated (cm/s)
			GAS-DRIVE METHOD RESULTS--Continued		
1U	9.65×10^{-9}	0.01	100.0	1.0	9.65×10^{-9}
			76.7	.172	1.66×10^{-9}
			74.2	.137	1.32×10^{-9}
			72.5	.121	1.17×10^{-9}
			67.1	.070	6.76×10^{-10}
			63.6	.037	3.57×10^{-10}
			62.0	.029	2.80×10^{-10}
			59.0	.017	1.64×10^{-10}
			57.1	.010	9.65×10^{-11}
			56.0	.008	7.72×10^{-11}
			52.8	.0036	3.48×10^{-11}
			51.3	.0014	1.35×10^{-11}
			CENTRIFUGE METHOD RESULTS		
	5.31×10^{-6}	5.5	100.0	1.0	5.31×10^{-6}
			72.0	.034	1.81×10^{-7}
			71.8	.033	1.75×10^{-7}
			70.5	.024	1.27×10^{-7}
			68.2	.020	1.06×10^{-7}
			65.5	.010	5.31×10^{-8}
			63.0	.0061	3.24×10^{-8}
			59.9	.0034	1.81×10^{-8}
			58.6	.0027	1.43×10^{-8}
			57.2	.0017	9.03×10^{-9}
			56.0	.0014	7.43×10^{-9}
			52.6	.00066	3.50×10^{-9}
			51.1	.00038	2.02×10^{-9}
			50.4	.00034	1.81×10^{-9}
			46.3	.00016	8.49×10^{-10}
			44.2	.000082	4.35×10^{-10}
			43.1	.000067	3.56×10^{-10}
			42.9	.000061	3.24×10^{-10}
			41.7	.000053	2.81×10^{-10}
			39.4	.000028	1.49×10^{-10}

Table 4.--*Relative permeability and corresponding calculated unsaturated hydraulic-conductivity values*--Continued

Sample label	Hydrauiic conductivity saturated (cm/s)	Perme-ability saturated (mD)	Percent satu-ration	Relative perme-ability (fraction)	Hydraulic conductivity unsaturated (cm/s)
		CENTRIFUGE METHOD RESULTS--Continued			
2A	1.46×10^{-4}	151.5	100.0	1.0	1.46×10^{-4}
			86.0	.053	7.75×10^{-6}
			85.0	.046	6.73×10^{-6}
			83.6	.033	4.83×10^{-6}
			82.6	.024	3.51×10^{-6}
			81.5	.017	2.49×10^{-6}
			80.7	.014	2.05×10^{-6}
			79.5	.010	1.46×10^{-6}
			78.0	.0064	9.36×10^{-7}
			77.0	.0049	7.17×10^{-7}
			75.7	.0034	4.97×10^{-7}
			74.2	.0021	3.07×10^{-7}
			72.9	.0012	1.75×10^{-7}
			71.8	.00068	9.94×10^{-8}
			71.0	.00040	5.85×10^{-8}
			70.2	.00021	3.07×10^{-8}
			69.5	.000072	1.05×10^{-8}
18A	2.90×10^{-9}	.003	100.0	1.0	2.90×10^{-9}
			97.3	.305	8.83×10^{-10}
			96.4	.222	6.43×10^{-10}
			95.3	.129	3.74×10^{-10}
			94.3	.079	2.29×10^{-10}
			93.1	.031	8.98×10^{-11}
			92.1	.011	3.19×10^{-11}
			91.7	.0014	4.05×10^{-12}
4-5H	7.14×10^{-5}	74	100.0	1.0	7.14×10^{-5}
			64.1	.039	2.79×10^{-6}
			62.4	.032	2.29×10^{-6}
			59.0	.019	1.36×10^{-6}
			57.5	.014	1.00×10^{-6}
			57.1	.013	9.29×10^{-7}
			51.9	.0045	3.21×10^{-7}
			50.5	.0031	2.21×10^{-7}
			49.9	.0024	1.71×10^{-7}
			49.0	.0020	1.43×10^{-7}
			48.3	.0014	1.00×10^{-7}

Table 4.--*Relative permeability and corresponding calculated unsaturated hydraulic-conductivity values*--Continued

Sample label	Hydraulic conductivity saturated (cm/s)	Permeability saturated (mD)	Percent saturation	Relative permeability (fraction)	Hydraulic conductivity unsaturated (cm/s)
			CENTRIFUGE METHOD RESULTS--Continued		
17A	1.45×10^{-8}	0.015	100.0	1.0	1.45×10^{-8}
			95.8	.578	8.37×10^{-9}
			94.3	.506	7.33×10^{-9}
			92.3	.377	5.46×10^{-9}
			90.0	.297	4.30×10^{-9}
			88.4	.221	3.20×10^{-9}
			85.3	.157	2.27×10^{-9}
			80.2	.034	4.92×10^{-10}
			80.0	.030	4.34×10^{-10}
			78.8	.020	2.90×10^{-10}
			77.0	.0061	8.83×10^{-11}
			76.1	.0022	3.19×10^{-11}
			75.7	.00028	4.05×10^{-12}
5-9	1.78×10^{-5}	184	100.0	1.0	1.78×10^{-5}
			76.9	.026	4.62×10^{-7}
			72.5	.0097	1.72×10^{-7}
			71.5	.0081	1.44×10^{-7}
			68.9	.0053	9.41×10^{-8}
			67.5	.0034	6.04×10^{-8}
			65.8	.0028	4.97×10^{-8}
			63.4	.0014	2.49×10^{-8}
			61.3	.0010	1.78×10^{-8}
			60.1	.00047	8.35×10^{-9}
			59.1	.00042	7.46×10^{-9}
			55.8	.00013	2.31×10^{-9}
			50.9	.0000077	1.37×10^{-10}
1UH	2.12×10^{-7}	.22	100.0	1.0	2.12×10^{-7}
			81.4	.338	7.18×10^{-8}
			78.9	.292	6.20×10^{-8}
			74.7	.218	4.63×10^{-8}
			70.8	.164	3.48×10^{-8}
			65.1	.099	2.10×10^{-8}
			63.2	.077	1.64×10^{-8}
			60.1	.057	1.21×10^{-8}
			58.4	.044	9.34×10^{-9}
			54.2	.029	6.16×10^{-9}
			51.6	.016	3.40×10^{-9}
			47.8	.0094	2.00×10^{-9}
			45.9	.0049	1.04×10^{-9}
			43.6	.0035	7.43×10^{-10}

Table 4.--*Relative permeability and corresponding calculated unsaturated hydraulic-conductivity values*--Continued

Sample label	Hydraulic conductivity saturated (cm/s)	Permeability saturated (mD)	Percent saturation	Relative permeability (fraction)	Hydraulic conductivity unsaturated (cm/s)
			CENTRIFUGE METHOD RESULTS--Continued		
1UH--Continued			39.7	0.0014	2.97×10^{-10}
			38.0	.00063	1.34×10^{-10}
			37.3	.00056	1.19×10^{-10}
			34.8	.00023	4.88×10^{-11}
			34.7	.00021	4.46×10^{-11}
			33.8	.00018	3.82×10^{-11}
			30.8	.000027	5.73×10^{-12}
4-6H	8.40×10^{-6}	8.7	100.0	1.0	8.40×10^{-6}
			81.8	.061	5.12×10^{-7}
			81.2	.057	4.79×10^{-7}
			80.3	.047	3.95×10^{-7}
			78.3	.034	2.86×10^{-7}
			76.5	.020	1.68×10^{-7}
			75.3	.017	1.43×10^{-7}
			74.5	.013	1.09×10^{-7}
			73.9	.012	1.01×10^{-7}
			72.3	.0079	6.63×10^{-8}
			71.6	.0067	5.63×10^{-8}
			70.0	.0044	3.70×10^{-8}
			69.4	.0033	2.77×10^{-8}
			66.9	.0017	1.43×10^{-8}
			65.7	.0014	1.18×10^{-8}
			64.7	.00094	7.89×10^{-9}
			63.7	.00810	6.80×10^{-9}
			62.4	.00047	3.95×10^{-9}
			62.0	.00045	3.78×10^{-9}
			61.9	.00033	2.77×10^{-9}
			61.3	.00031	2.60×10^{-9}
			57.8	.000096	8.06×10^{-10}
			57.3	.000066	5.54×10^{-10}
			56.7	.000050	4.20×10^{-10}
			55.3	.000019	1.60×10^{-10}

Table 4.--*Relative permeability and corresponding calculated unsaturated hydraulic-conductivity values*--Continued

Sample label	Hydraulic conductivity saturated (cm/s)	Permeability saturated (mD)	Percent saturation	Relative permeability (fraction)	Hydraulic conductivity unsaturated (cm/s)
			CENTRIFUGE METHOD RESULTS--Continued		
IV	1.75×10^{-5}	18.1	100.0	1.0	1.75×10^{-5}
			95.3	.308	5.38×10^{-6}
			93.8	.230	4.02×10^{-6}
			92.4	.193	3.37×10^{-6}
			90.5	.126	2.20×10^{-6}
			88.7	.093	1.62×10^{-6}
			86.6	.046	8.04×10^{-7}
			85.8	.039	6.81×10^{-7}
			85.1	.028	4.89×10^{-7}
			83.8	.021	3.67×10^{-7}
			81.9	.0057	9.96×10^{-8}
			81.1	.0045	7.86×10^{-8}
			80.2	.0022	3.84×10^{-8}
			79.3	.0010	1.75×10^{-8}
3P	2.90×10^{-8}	.03	100.0	1.0	2.90×10^{-8}
			88.5	.588	1.71×10^{-8}
			88.1	.582	1.69×10^{-8}
			84.5	.443	1.28×10^{-8}
			78.2	.248	7.19×10^{-9}
			75.2	.156	4.52×10^{-9}
			74.8	.152	4.41×10^{-9}
			70.2	.096	2.78×10^{-9}
			66.6	.047	1.36×10^{-9}
			63.7	.033	9.57×10^{-10}
			60.1	.014	4.06×10^{-10}
			58.5	.0078	2.26×10^{-10}
			57.2	.0055	1.60×10^{-10}
			54.5	.0016	4.64×10^{-11}

Table 5.--*Water retention for pressure plate and*

[Water retention, in percent volumetric water content; matric

Sample label	Method	Matric								
		0.03	0.07	0.14	0.28	0.34	0.55	0.69	1.03	1.38
IV	PLATE	0.93	0.91	0.86	0.76	--	0.66	--	0.57	--
	CENT.	--	.95	.87	--	0.75	--	0.68	--	0.61
	CENT.	--	1.00	.98	--	.81	--	.69	--	--
2A	PLATE	--	1.00	.86	.67	--	.63	--	.60	--
	CENT.	--	.91	.77	--	.65	--	.53	--	.41
4-5	PLATE	--	.98	.98	.94	--	.61	--	.50	--
	CENT.	--	1.00	1.00	--	.58	--	.40	--	.30
4-5H	CENT.	--	1.00	.90	--	.60	--	.38	--	.28
4-6	PLATE	--	1.00	1.00	.97	--	.94	--	.91	--
	CENT.	--	1.00	1.00	--	.97	--	.92	--	.86
4-6H	CENT.	--	1.00	1.00	--	.76	--	.68	--	.60
4-7	PLATE	--	.97	.92	.82	--	.71	--	.67	--
	CENT.	--	.94	.78	--	.69	--	.63	--	.55
4-7H	PLATE	.96	.95	.91	.79	--	.59	--	.50	--
5-9	PLATE	--	.83	.74	.62	--	.58	--	.55	--
	CENT.	--	.95	.87	--	.63	--	.53	--	.45
1U	PLATE	--	--	--	--	--	--	.78	--	.68
	CENT.	--	1.00	1.00	--	1.00	--	.98	--	--
1UH	PLATE	.98	.98	.96	.83	--	.71	--	.63	--
	CENT.	--	1.00	1.00	--	.84	--	.70	--	.63
5-2	CENT.	--	1.00	1.00	--	.91	--	.84	--	.75
	PLATE	--	--	--	--	--	--	.59	--	.47
	CENT.	--	--	--	--	--	--	1.00	--	--
17A	CENT.	--	1.00	1.00	--	1.00	--	.98	--	.97
	CENT.	--	--	--	--	--	--	1.00	--	--
	PLATE	--	--	--	--	--	--	.91	--	.85
18A	CENT.	--	--	--	--	--	--	1.00	--	--
	PLATE	--	--	--	--	--	--	.98	--	.93
3P	CENT.	--	--	--	--	--	--	1.00	--	--
	PLATE	--	--	--	--	--	--	.91	--	.78

centrifuge methods on vertical and horizontal core samples

potential in bars; PLATE, pressure plate; CENT., centriufge; --, no data]

potential										
1.72	2.41	2.76	3.45	4.14	5.52	6.90	8.28	13.79	34.48	68.97
--	0.47	--	--	--	--	0.41	--	--	--	--
--	--	0.55	--	0.51	--	.48	--	--	--	--
0.49	--	--	--	--	--	--	--	--	--	--
--	.50	--	--	--	--	--	--	--	--	--
--	--	.32	--	.29	--	--	--	--	--	--
--	.32	--	--	--	--	--	--	--	--	--
--	--	.23	--	.19	--	--	--	--	--	--
--	--	--	--	--	--	--	--	--	--	--
--	.73	--	--	--	--	--	--	--	--	--
--	--	.78	--	.74	--	--	--	--	--	--
--	--	.50	--	.45	--	--	--	--	--	--
--	.61	--	--	--	--	--	--	--	--	--
--	--	.47	--	.44	--	--	--	--	--	--
--	.42	--	--	--	--	.37	--	--	--	--
--	.52	--	--	--	--	--	--	--	--	--
--	--	.38	--	.33	--	--	--	--	--	--
--	--	.57	--	--	0.44	.42	0.40	--	--	--
.77	--	--	0.58	--	--	.47	--	0.40	0.35	--
--	.53	--	--	--	--	.45	--	--	--	--
--	--	.56	--	.52	--	--	--	--	--	--
--	--	.65	--	.58	--	.51	--	--	--	--
--	--	.36	--	--	.27	.26	.24	--	--	--
.73	--	--	.65	--	--	.51	--	.36	.28	0.21
--	--	.92	--	.89	--	.82	--	--	--	--
1.00	--	--	1.00	--	--	.75	--	.63	.40	.33
--	--	.78	--	--	.70	.69	.68	--	--	--
1.00	--	--	1.00	--	--	1.00	--	1.00	.65	.54
--	--	.88	--	--	.84	.82	.81	--	--	--
.80	--	--	.64	--	--	.58	--	.46	.30	.22
--	--	.64	--	--	.56	.55	.53	--	--	--

Table 6.--*Water retention for mercury intrusion porosimetry method*

[Water retention, θ_v, in percent volumetric water content; matric potential, ψ_m, in bars. Tests done at U.S. Geological Survey petrophysics laboratory, in Golden, Colo.]

Sample 20AP		Sample 18AP	
θ_v	ψ_m	θ_v	ψ_m
0.2594	0.055	0.2747	0.088
.2589	.061	.2742	.711
.2578	.070	.2737	.984
.2574	.081	.2733	1.499
.2567	.103	.2723	2.399
.2559	.112	.2718	3.816
.2548	.129	.2705	4.770
.2536	.141	.2695	6.815
.2531	.152	.2685	8.177
.2523	.165	.2676	10.900
.2514	.179	.2636	15.330
.2487	.191	.2619	20.440
.2375	.301	.2551	24.530
.2255	.436	.2481	29.980
.2194	.572	.2191	37.480
.2149	.708	.1848	44.980
.2079	.981	.1686	49.060
.2039	1.253	.1577	51.790
.2003	1.499	.1500	54.520
.1983	1.772	.1436	57.240
.1956	2.181	.1424	61.330
.1907	2.590	.1385	63.380
.1886	3.135	.1324	68.150
.1866	3.680	.1257	74.960
.1837	4.634	.1235	81.770
.1822	5.452	.1192	87.230
.1795	6.815	.1183	95.400
.1733	14.310	.1087	102.200
.1716	17.720	.1067	109.000
.1702	20.440	.1050	115.800
.1678	27.260	.1017	122.700
.1643	40.890	.0999	129.500
.1604	51.790	.0982	136.300
.1481	59.970		
.1364	66.780		

Table 6.--*Water retention for mercury intrusion porosimetry method*--Continued

Sample 20AP	
θ_v	ψ_m
0.1318	72.230
.1254	79.050
.1193	87.230
.1156	92.680
.1114	102.200
.1090	109.000
.1066	115.800
.1043	124.000
.1026	129.500
.1012	136.300

Sample 8A		Sample 13A		Sample 19A	
θ_v	ψ_m	θ_v	ψ_m	θ_v	ψ_m
0.3306	0.057	0.3338	0.130	0.3265	0.053
.3300	.122	.3335	.302	.3256	.074
.3299	.174	.3318	.438	.3249	.089
.3296	.193	.3300	.574	.3245	.104
.3280	.329	.3281	.711	.3239	.115
.3252	.452	.3254	.847	.3231	.126
.3224	.574	.3243	.983	.3227	.142
.3204	.710	.3215	1.256	.3218	.152
.3147	.996	.3176	.567	.3209	.172
.3116	1.256	.3106	1.908	.3206	.182
.3088	1.499	.3057	2.290	.3168	.191
.3057	1.772	.2990	2.671	.3109	.301
.3031	2.072	.2962	2.889	.2950	.437
.3000	2.453	.2943	3.135	.2881	.573
.2972	2.862	.2900	3.544	.2836	.709
.2935	3.407	.2879	3.816	.2762	.845
.2905	3.952	.2842	4.361	.2694	1.363
.2865	4.770	.2820	4.770	.2628	1.935
.2836	5.452	.2798	5.179	.2592	2.453
.2798	6.406	.2771	5.806	.2561	3.135
.2777	6.951	.2732	6.815	.2517	4.116
.2749	8.177	.2711	7.251	.2491	4.770
.2713	9.540	.2673	8.859	.2467	5.452
.2681	10.900	.2620	11.580	.2436	6.815
.2630	13.630	.2593	13.630	.2383	10.900
.2586	16.350	.2526	17.040	.2362	13.630
.2546	19.080	.2479	19.080	.2334	17.720
.2493	23.170	.2422	21.810	.2314	21.810
.2442	27.260	.2350	24.530	.2292	27.260
.2369	32.710	.2286	27.260	.2267	32.710

Table 6.--*Water retention for mercury intrusion porosimetry method*--Continued

Sample 8A		Sample 13A		Sample 19A	
θ_v	ψ_m	θ_v	ψ_m	θ_v	ψ_m
0.2304	38.160	0.2181	30.670	0.2236	39.520
.2216	43.610	.2014	34.070	.2195	45.660
.2123	47.700	.1897	36.120	.2131	49.750
.2061	50.430	.1781	38.160	.2031	54.520
.1954	54.520	.1700	40.210	.1894	57.240
.1889	57.240	.1653	42.250	.1861	59.970
.1811	59.970	.1606	44.980	.1791	62.690
.1765	62.690	.1559	47.700	.1717	68.150
.1713	66.780	.1512	51.110	.1646	72.920
.1667	70.870	.1466	54.520	.1599	78.370
.1620	74.960	.1434	58.610	.1567	81.770
.1558	80.410	.1387	62.690	.1505	88.590
.1496	87.230	.1341	68.150	.1458	95.400
.1450	95.400	.1309	74.960	.1427	102.200
.1403	103.600	.1263	81.770	.1349	109.700
.1341	111.800	.1231	88.590	.1318	122.700
.1326	118.600	.1200	95.400	.1286	129.500
.1295	124.000	.1169	102.200	.1255	136.300
.1264	129.500	.1153	109.000		

Sample 14A		Sample 16A		Sample 11A	
θ_v	ψ_m	θ_v	ψ_m	θ_v	ψ_m
0.3476	0.046	0.3287	0.189	0.3259	0.057
.3459	.055	.3259	.302	.3253	.084
.3430	.070	.3230	.438	.3250	.121
.3402	.086	.3200	.574	.3246	.137
.3327	.103	.3172	.765	.3244	.154
.3284	.119	.3110	.982	.3241	.159
.3257	.125	.3077	1.132	.3238	.179
.3215	.138	.3044	1.255	.3235	.193
.3179	.152	.3004	1.417	.3222	.329
.3153	.164	.2951	1.635	.3211	.438
.3125	.178	.2931	1.772	.3190	.574
.3101	.191	.2910	1.908	.3158	.710
.2989	.299	.2887	2.058	.3133	.847
.2886	.435	.2852	2.208	.3106	1.011
.2817	.571	.2817	2.453	.3081	1.174
.2771	.707	.2779	2.617	.3043	1.363
.2674	.979	.2747	2.753	.3001	1.635
.2625	1.116	.2717	2.889	.2960	1.908
.2542	1.363	.2656	3.216	.2924	2.181
.2509	1.499	.2565	3.571	.2881	2.453

Table 6.--*Water retention for mercury intrusion porosimetry method*--Continued

Sample 14A		Sample 16A		Sample 11A	
θ_v	ψ_m	θ_v	ψ_m	θ_v	ψ_m
0.2477	1.635	0.2528	3.789	0.2858	2.726
.2409	1.908	.2482	4.143	.2817	3.135
.2339	2.181	.2467	4.416	.2778	3.544
.2295	2.453	.2407	4.770	.2732	4.089
.2239	2.726	.2333	5.343	.2694	4.634
.2187	3.135	.2303	5.724	.2666	5.179
.2150	3.407	.2244	6.188	.2619	6.133
.2107	3.816	.2184	6.706	.2589	6.815
.2069	4.089	.2110	7.373	.2511	9.540
.2035	4.498	.2035	8.177	.2438	12.270
.1991	5.179	.1902	9.540	.2383	14.990
.1948	5.997	.1693	11.580	.2330	18.400
.1905	6.815	.1619	13.630	.2270	21.810
.1818	7.496	.1530	17.040	.2195	26.580
.1790	10.220	.1455	20.440	.2099	31.350
.1732	12.270	.1336	24.530	.1965	36.800
.1689	14.310	.1172	28.620	.1826	40.890
.1660	16.350	.1038	34.070	.1725	42.930
.1602	20.440	.0934	39.520	.1658	44.980
.1530	25.900	.0845	45.660	.1579	47.700
.1415	32.710	.0770	51.790	.1516	50.430
.1271	37.480	.0726	57.240	.1453	53.150
.1127	40.890	.0666	65.420	.1422	55.880
.1040	43.610	.0636	72.230	.1375	58.610
.0982	46.340	.0607	79.050	.1328	61.330
.0910	50.430	.0562	88.590	.1281	65.420
.0867	54.520	.0547	95.400	.1233	69.510
.0824	58.610	.0532	102.200	.1202	73.600
.0795	64.060	.0502	109.000	.1155	79.050
.0752	70.870	.0487	115.800	.1108	84.500
.0708	79.050	.0487	122.700	.1076	90.630
.0680	87.230	.0473	129.500	.1029	98.130
.0651	95.400	.0458	136.300	.0982	107.700
				.0950	115.800
				.0919	122.700
				.0887	129.500
				.0872	136.300

STATISTICAL ANALYSES OF INTRINSIC PERMEABILITY DATA

For comparative analyses of permeability methods, it was indicated by using the Kolmogorov-Smirnoff test (Zar, 1984) that the intrinsic permeability data determined from the four methods were log-normally distributed. Correlations of the mean squared values and the variances squared gave coefficients of determination (r^2) >0.85. In addition, a fractile diagram of the data presented straight lines. Both of these analyses indicate log-normally distributed populations (Warrick and Nielsen, 1980). This distribution is skewed, as are the low-flow permeability data for all three methods. Determination of this distribution for these data indicates that the data are valid based on the idea that physical phenomena and parameters typically are characterized by distributions that are log normal. This is particularly true in geological settings and was shown to be true for permeability (Hammermeister, 1978). The geometric mean ($\bar{g}$):

$$[(X_1) \times (X_2) \times \ldots \times (X_n)]^{1/n}, \qquad (20)$$

weights the values so that one high value will not misrepresent the mean of the whole population.

In comparative analyses of subsamples involving very small sample sizes (n), arithmetic means ($\bar{x}$) are used for comparison along with standard deviations to illustrate the variation around the mean. In comparisons involving large sample sizes, the geometric mean ($\bar{g}$) and confidence intervals (standard deviations cannot be calculated for log-normally distributed populations) are used to compare permeability methods to more appropriately represent the populations. Because of uncertainties in the true distribution function for the data (for example, whether normal or log-normal), analyses based on the assumption of both normal and log-normal distributions are provided.

The difference between Calico Hills samples and the remaining samples is listed in table 3, which lists intrinsic permeability values for all samples. Calico Hills samples are designated as low flow. Also, using air permeability as an index, these samples exhibit a range of 0.01 (or 0.00) to 2.80 mD. This division is reasonable because the Calico Hills samples tend to have larger clay and zeolite contents and, therefore, probably have lower macroporosity. Also the clay and zeolites may interact with water and additionally contribute to the observed lower water flow rates. The only other sample indicating a lower flow rate is 10-A (0.09 mD), which has been classified as bedded-reworked tuff. Lithologic logs of the borehole from which the sample was taken describe this particular depth interval as argillic and zeolitic and include it as part of the Calico Hills to 1,835.7 feet. The remaining samples are considered to be high flow and exhibit a range of air permeability between 2.3 and 374.0 mD.

The permeability data listed in table 7 include means, standard deviations, and coefficient of variation (CV) of specific liquid permeability to water as a function of core-sample matrix description and provide a more detailed examination of the permeability data. Most noticeable is that the Calico Hills sample permeability values are, on the average, three orders of magnitude lower than all other sample permeability values.

When analyzed separately, the five different rock-unit types within the Calico Hills vary. This may indicate valid differences among rock-unit flows. Note also that vitric tuff samples exhibit the highest permeability values.

Table 7.--*Specific liquid permeability means, standard deviations, and coefficients of variation for core samples as a function of core matrix*

[n, number of samples used in analysis; CV, coefficient of variation; all analyses assume normally distributed populations]

Geologic unit	Core matrix description	n	Specific permeability to water (millidarcies)		
			Mean	Standard deviation	CV
Calico Hills	Vitric	2	0.291	0.290	0.997
	Devitrified, zeolitized	4	.030	.021	.690
	Zeolitized	8	.016	.007	.428
	Zeolitized, partially argillic	4	.006	.005	.428
	Bedded-reworked tuff	1	.010		
Base of Tiva Canyon Member	Vitric	2	50.01	49.99	1.00
	Vitric, partially argillic	1	145.90		
Yucca Mountain Member	Vitric	5	92.20	105.64	1.15
Pah Canyon Member	Vitric	4	17.59	19.35	1.10
Bedded-reworked tuff		5	5.89	7.09	1.20
Topopah Spring Member	Vitric	1	162.00		

The high-flow data in table 7 show much more variability as indicated by high coefficients of variation (CV), which is the standard deviation divided by the mean. Values of two samples from UE-25a #6 (see table 1), 4A and IV, although from samples in different formations, are much lower than the remaining sample values. In addition, there are three very low permeability values, two from UE-25 UZ #4: 4-4 from Pah Canyon Member and 4-7, bedded-reworked tuff from UE-25 UZ #5. No explanation for these low values can be offered at this time.

Statistical analyses of intrinsic permeability data are listed for four methods in table 8, including low- and high-flow samples, and under the assumption of both normally and log-normally distributed populations. The low-flow data are as expected, with the air permeability method measurements representing higher flow than the other three methods. The large variation in the high-flow data seems to complicate the arithmetic means, although the geometric means probably represent both the high- and low-flow data more accurately.

Table 8.--*Intrinsic permeability mean and standard deviation values*

[mD, millidarcies]

	Air permeability (mD)	Klinkenberg permeability (mD)	Nonpolar oil permeability (mD)	Specific permeability to water (mD)
		LOW FLOW		
Assumed normally distributed				
Mean ($\bar{x}$)	0.199	0.043	0.044	0.044
Standard deviation	.225	.056	.088	.124
Assumed log-normally distributed				
Mean ($\bar{g}$)	.129	.025	.007	.011
		HIGH FLOW		
Assumed normally distributed				
Mean ($\bar{x}$)	40.41	84.76	81.06	53.79
Standard deviation	111.78	105.55	105.76	76.99
Assumed log-normally distributed				
Mean ($\bar{g}$)	50.08	30.32	25.97	7.13

The Klinkenberg method for determining intrinsic permeability requires gas permeability measurements at each of several confining pressures. The change in permeability over the range of confining pressures used on 12 cores is listed in table 9. The values are related to core-matrix description. In the first six samples, there is a large percent change in permeability, 66 to 88 percent, over the range of confining pressures induced on those cores. The second six samples do not show large permeability changes. The integrity of the core matrix under pressure may be questioned when considering the large changes in sample permeability values. Zeolitized matrices occur in samples within the range of permeability changes whereas the three partially vitric cores all exhibited large changes in permeability with increased confining pressure. Differences in permeability values due to confining pressure may not pose a problem because this method accounts appropriately for in-situ overburden pressures.

Horizontal and vertical core intrinsic permeability values are listed in table 10. Means and standard deviations indicate little difference between data from vertical and horizontal core. The data also were regressed, and coefficients of determination (r^2) are listed. Correlations are fairly strong between the vertical and horizontal data for both the low- and high-flow samples.

Table 9.--*Reduction in Klinkenberg permeability values as a function of confining pressure for various rock matrix types*

Sample label	Depth (meters)	Confining pressure range (psi)	Percent change in permeability	Core matrix description
14A	1,880.3	300-900	88	Zeolitized
2P	1,398.2	300-900	82	Partially vitric
16A	1,932.5	300-400	80	Zeolitized
3P	1,516.3	300-900	70	Partially vitric
1P	1,329.0	300-900	67	Partially vitric
1A	1,785.6	50-200	66	Zeolitized, partially argillic
13A	1,792.3	50-200	29	Zeolitized
11A	1,700.0	300-900	22	Zeolitized, partially argillic
17A	2,076.0	300-750	19	Zeolitized
12A	1,756.9	300-900	17	Zeolitized
10A	1,801.5	300-900	9	Bedded, reworked
18A	2,168.6	300-750	7	Zeolitized

Table 10.--*Intrinsic permeability means and standard deviations, regression equations, coefficients of determination, and standard error of estimate for vertical permeability (y) for low- and high-flow core samples*

[Values represent all cores that had both vertical and horizontal measurements and include all determination methods; mD, millidarcies; n, number of samples; r^2, coefficient of determination; SEE, standard error of estimate for vertical permeability (y)]

		Vertical permeability (y) (mD)	Horizontal permeability (x) (mD)
Low flow	Mean	0.15	0.13
	Standard deviation	.26	.25
	n	19	8
High flow	Mean	40.96	42.78
	Standard deviation	61.88	74.30
	n	18	5

Regression equations		r^2	SEE
Low flow	$y = 0.006 + 0.841\ x$	0.730	0.140
High flow	$y = -3.161 + 1.122\ x$	0.873	28.230

Regressions established between the methods of intrinsic permeability determination for low- and high-flow samples are listed in table 11. Coefficient of determination (r^2) values express the proportion of the total variation in the values of the variable y that can be accounted for or explained by a linear relation with the random variable x. These values are very high for all regressions, which implies little need for expensive detailed measurements.

Table 11.--*Regressions of intrinsic permeability data for four methods of determination*

[Samples having data for all four methods were used, and all replicates were included. All values are in millidarcies]

Methods regressed (x versus y)	Regression equation	Coefficient of determination (r^2)	Standard error of estimate
Klinkenberg compared to air			
Low flow	y = -0.014 + 4.291 x	0.995	0.02
High flow	y = 17.247 + 0.861 x	.973	21.19
Klinkenberg compared to specific permeability to water			
Low flow	y = -0.074 + 2.489 x	.945	.05
High flow	y = -2.442 + 0.641 x	.999	3.24
Klinkenberg compared to nonpolar oil			
Low flow	y = -0.028 + 1.287 x	.983	.01
High flow	y = 1.291 + 0.909 x	.984	17.39
Specific permeability to water compared to air			
Low flow	y = 0.121 + 1.632 x	.944	.09
High flow	y = 20.938 + 1.335 x	.963	24.84
Specific permeability to water compared to nonpolar oil			
Low flow	y = 0.012 + 0.498 x	.967	.02
High flow	y = 4.609 + 1.421 x	.989	14.56

SUMMARY

The data obtained using four laboratory methods for the determination of permeability in rock cores showed considerable variability within the population. The variability probably was increased by the nature of sample selection There was, however, a significant difference between sample values from the Calico Hills formation and all other rock units. On the average, Calico Hills intrinsic permeability values were smaller by three orders of magnitude.

The mean intrinsic permeability data for the four methods showed expected trends. Air permeability values were highest because they are not affected by fluid properties and interactions. Klinkenberg permeability values, which demonstrate ideal fluid permeability, were the next highest mean values. Nonpolar oil permeability values (which introduce the density and viscosity factors of fluids) and specific liquid permeability to water (which shows influences of formation water viscosity, density, and formation water-matrix interactions) were the lowest values.

There was virtually no difference between the means in intrinsic permeability values of horizontal and vertical cores. Regressions of horizontal compared to vertical core permeability values resulted in high coefficient of determination (r^2) values.

SELECTED REFERENCES

Amyx, J.W., Bass, D.M., Jr., and Whiting, R.L., 1960, Petroleum Reservoir Engineering: New York, McGraw-Hill Book Co., 609 p. (NNA.870831.0014)

American Society for Testing and Materials, 1985, Standard test method for determination of pore volume and pore volume distribution of soil and rock by mercury intrustion porosimetry, D4404-84: Annual Book of ASTM Standards, section 4, Construction, v. 4.08, Soil and rock: Building stones, p. 860-867. (NNA.900710.0185)

Blake, G.R., 1965, Bulk density, *in* Black, C.A., ed., Methods of soil analysis--Part 1, Physical and mineralogical methods, 1st ed.: Madison, Wisc., American Society of Agronomy, p. 383-390. (NNA.900208.0031)

Blake, G.R., and Hartge, K.H., 1986, Bulk density, *in* Klute, Arnold, ed., Methods of soil analysis--Part 1, Physical and mineralogical methods, 2d ed.: Madison, Wisc., American Society of Agronomy, p. 363-375. (NNA.900227.0043)

Brown, H.W., 1951, Capillary pressure investigations: American Institute of Mining and Metallurgical Engineers Transactions, v. 192, p. 67-74. (NNA.900710.0187)

Childs, E.C., 1940, The use of soil moisture characteristics in soil studies: Soil Science, v. 50, p. 239-252. (NNA.900710.0196)

Conca, J.L., and Lane, D.L., 1988, Determination of unsaturated transport parameters in whole rock and unconsolidated materials: Battelle, Pacific Northwest Laboratory, Chemical Systems Analysis Section, Richland, Wash., 6 p. (NNA.900710.0199)

Constantz, James and Herkelrath, W.N., 1984, A submersible pressure outflow cell for measurement of soil water retention and diffusivity from 5 to 95 °C: Soil Science Society America Journal, v. 48, no. 1, p. 7-10. (HQS.880517.2642)

Corey, A.T., 1986, Air permeability, *in* Klute, Arnold, ed., Methods of soil analysis--Part 1, Physical and mineralogical methods, 2d ed.: Madison, Wisc., American Society of Agronomy, p. 1121-1136. (NNA.900227.0043)

Hagoort, J., 1980, Oil recovery by gravity drainage: Society of Petroleum Engineers Journal, v. 20, no. 3, p. 139-150. (NNA.900710.0189)

Hammermeister, D.P., 1978, Water and anion movement in selected soils of western Oregon: Ph.D. thesis, Oregon State University, Corvallis, Oreg., 270 p. (NNA.900710.0190)

Hillel, Daniel, 1982, Fundamentals of Soil Physics: New York, Academic Press, Inc., 413 p. (HQS.880517.1776)

Hoffman, R.N., 1963, A technique for the determination of capillary pressure curves using a constantly accelerated centrifuge: Society of Petroleum Engineers Journal, v. 3, no. 3, p. 227-235. (NNA.900710.0191)

Klinkenberg, L.J., 1941, The permeability of porous media to liquids and gases, *in* Drilling and Production Practices: New York American Petroleum Institute, p. 200. (HQS.880517.1787)

Klute, Arnold, 1986, Water retention--laboratory methods, *in* Klute, Arnold, ed., Methods of soil analysis--Part 1, Physical and mineralogical methods, 2d ed.: Madison, Wisc., American Society of Agronomy, p. 635-662. (NNA.900227.0043)

Montazer, P., and Wilson, W.E., 1984, Conceptual hydrologic model of flow in the unsaturated zone, Yucca Mountain, Nevada: U.S. Geological Survey Water-Resources Investigations Report 84-4345, 55 p. (NNA.870519.0109)

Nimmo, J.R., Rubin, Jacob, and Hammermeister, D.P., 1987, Unsaturated flow in a centrifugal field--Measurement of hydraulic conductivity and testing of Darcy's law: Water Resources Research, v. 32, no. 1, p. 124-134. (NNA.870729.0073)

Owens, W.W., Parrish, D.R., and Lamoreaux, W.E., 1956, An evaluation of a gas drive method for determining relative permeability relationships: American Institute of Mining and Metallurgical Engineers Transactions, v. 207, p. 275-280. (HQS.880517.2815)

Purcell, W.R., 1949, Capillary pressures--Their measurement using mercury and the calculation of permeability therefrom: American Institute of Mining and Metallurgical Engineers Transactions, v. 186, p. 39-46. (NNA.890522.0236)

Richards, L.A., 1931, Capillary conduction of liquids in porous mediums: Physics, v. 1, p. 318-333. (NNA.890522.0282)

Scheidegger, A.E., 1957: The Physics of Flow through Porous Media: New York, Macmillan, 353 p. (NNA.900710.0192)

Scott, R.B., and Castellanos, Mayra, 1984, Stratigraphic and structural relations of volcanic rocks in drill holes USW GU-3 and USW G-3, Yucca Mountain, Nye County, Nevada: U.S. Geological Survey Open-File Report 84-0491, 127 p. (NNA.890804.0017)

Skuse, Brian, 1984, Capillary pressure measurements in reservoir rock cores using the centrifuge: Palo Alto, Calif., Applications Data, Beckman Institute, Inc., 4 p. (NNA.900710.0193)

Slobod, R.L., Chambers, Adele, and Prehn, W.L., Jr., 1951, Use of centrifuge for determining connate water, residual oil and capillary pressure curves of small core samples: American Institute of Mining and Metallurgical Engineers Transactions, v. 192, p. 127-134. (NNA.900710.0188)

Van Spronsen, Engel, 1982, Three-phase relative permeability measurements using the centrifuge method, *in* 3rd Joint SPE/DOE Symposium on Enhanced Oil Recovery: Tulsa, Society of Petroleum Engineers, p. 217-240. (HQS.880517.2894)

Warrick, A.W., and Nielsen, D.R., 1980, Spatial variability of soil physical properties in the field, *in* Hillel, Daniel, Applications of Soil Physics: New York, Academic Press, p. 319-344. (NNA.900710.0194)

Zar, J.H., 1984, Biostatistical Analysis, 2d ed.: New Jersey, Prentice-Hall, 718 p. (NNA.900710.0195)

NOTE: Parenthesized numbers following each cited reference are for U.S. Department of Energy OCRWM Records Management purposes only and should not be used when ordering the publication.

APPENDIX I

Graphs of Relative Permeability Determined Using Centrifuge and Gas-Drive Methods

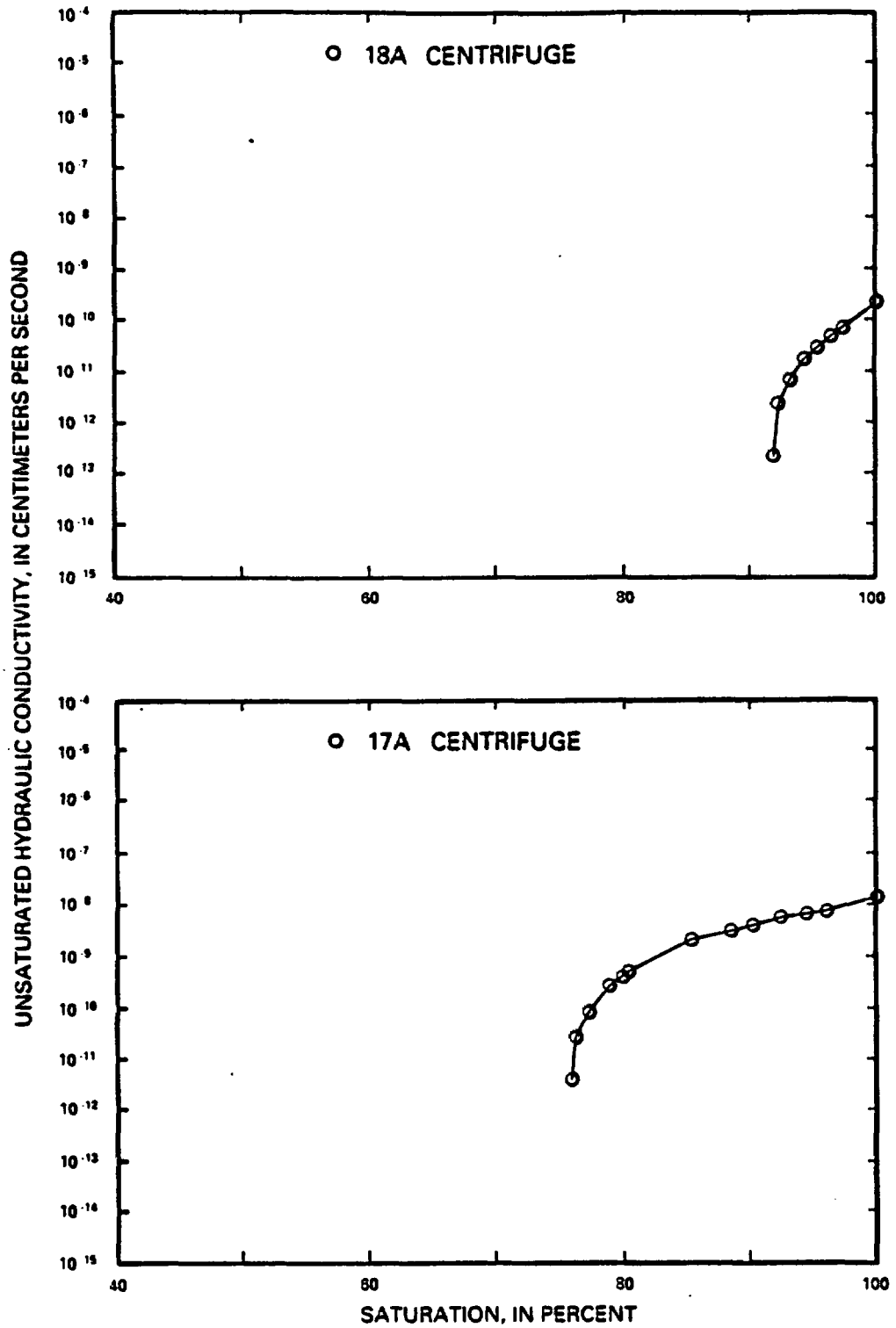

Figure I-1.--Relative permeability (unsaturated hydraulic conductivity) for samples 18A and 17A determined using centrifuge method.

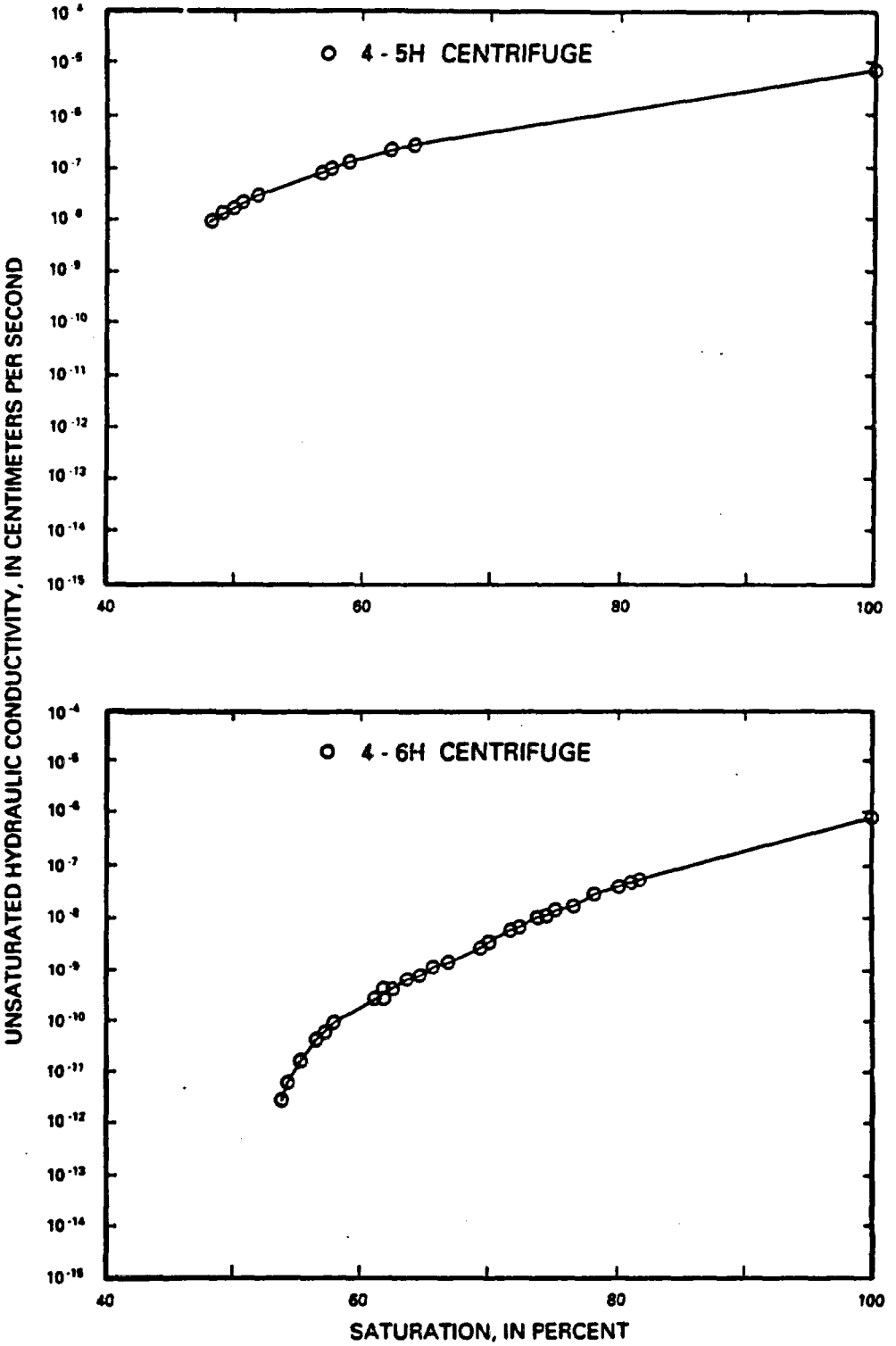

Figure I-2.--Relative permeability (unsaturated hydraulic conductivity) for samples 4-5H and 4-6H determined using centrifuge method.

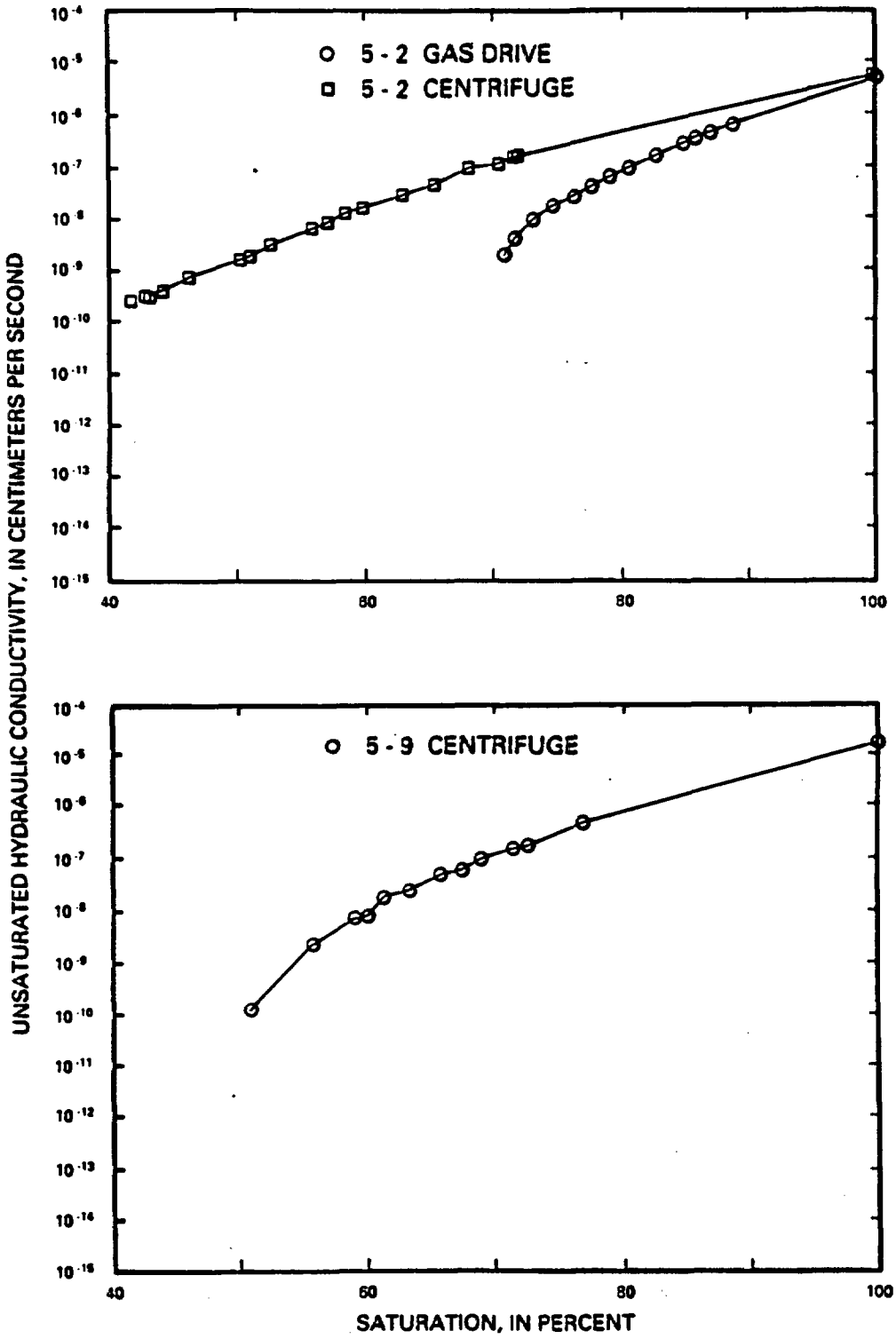

Figure I-3.--Relative permeability (unsaturated hydraulic conductivity) for sample 5-2 using centrifuge and gas-drive methods and for sample 5-9 determined using centrifuge method.

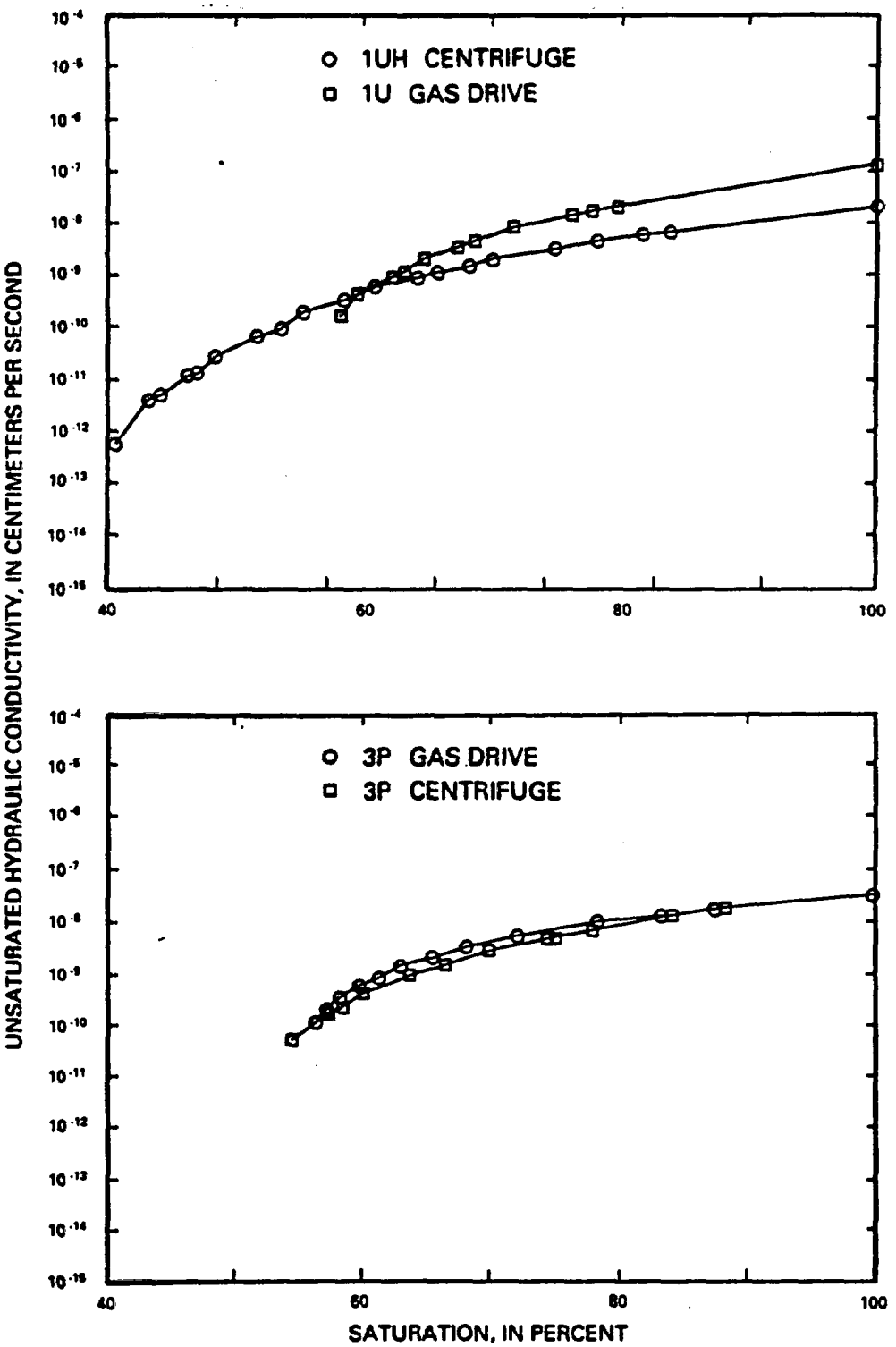

Figure I-4.--Relative permeability (unsaturated hydraulic conductivity) for samples 1UH and 3P determined using centrifuge method and for samples 1U and 3P using gas-drive method.

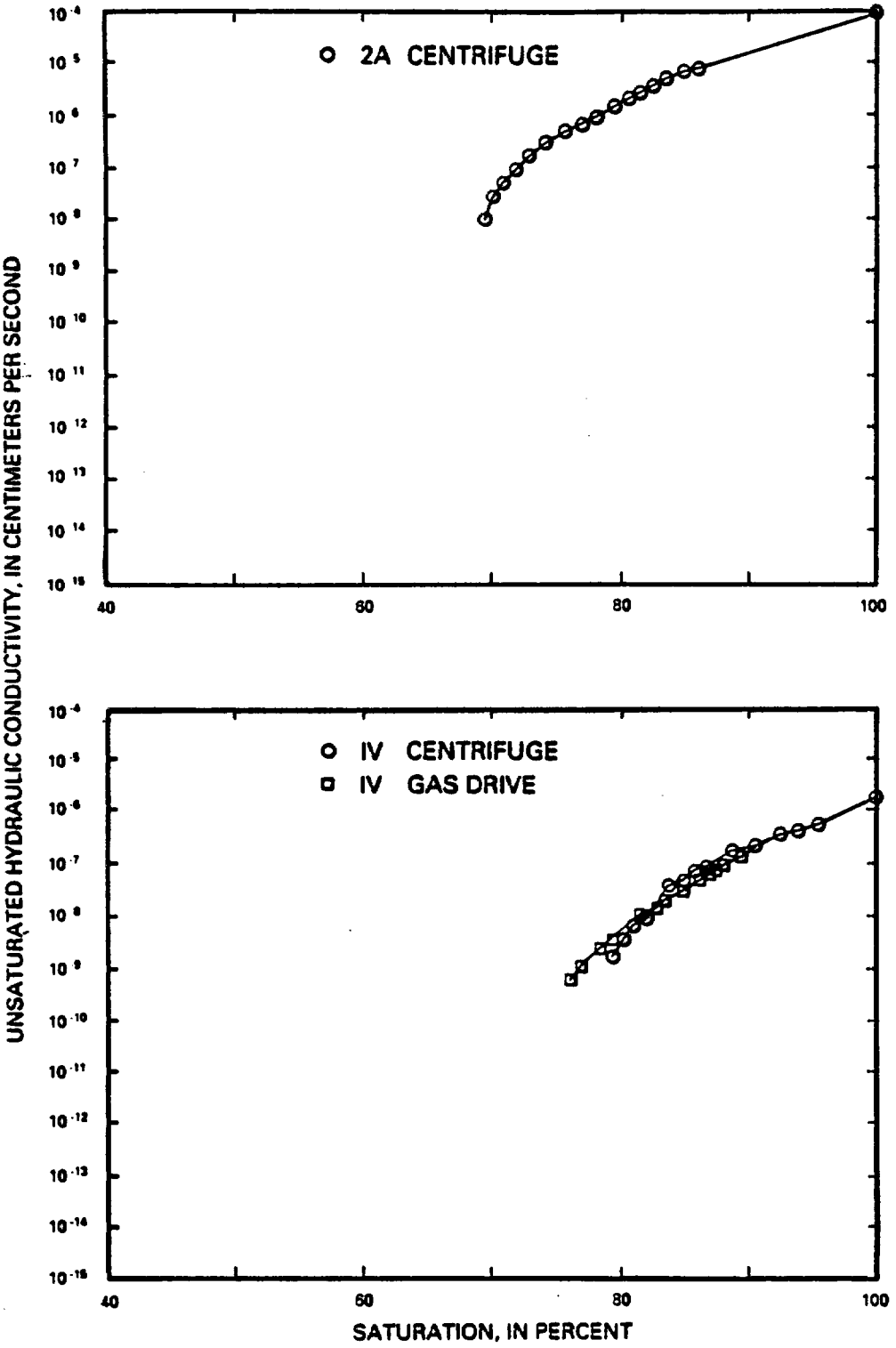

Figure I-5.--Relative permeability (unsaturated hydraulic conductivity) for sample 2A determined using centrifuge method and for sample IV using centrifuge and gas-drive methods.

APPENDIX II

Graphs of Water Retention:

II-1 through II-6. Centrifuge and Porous Plate Methods

II-7. Mercury Intrusion Porosimetry

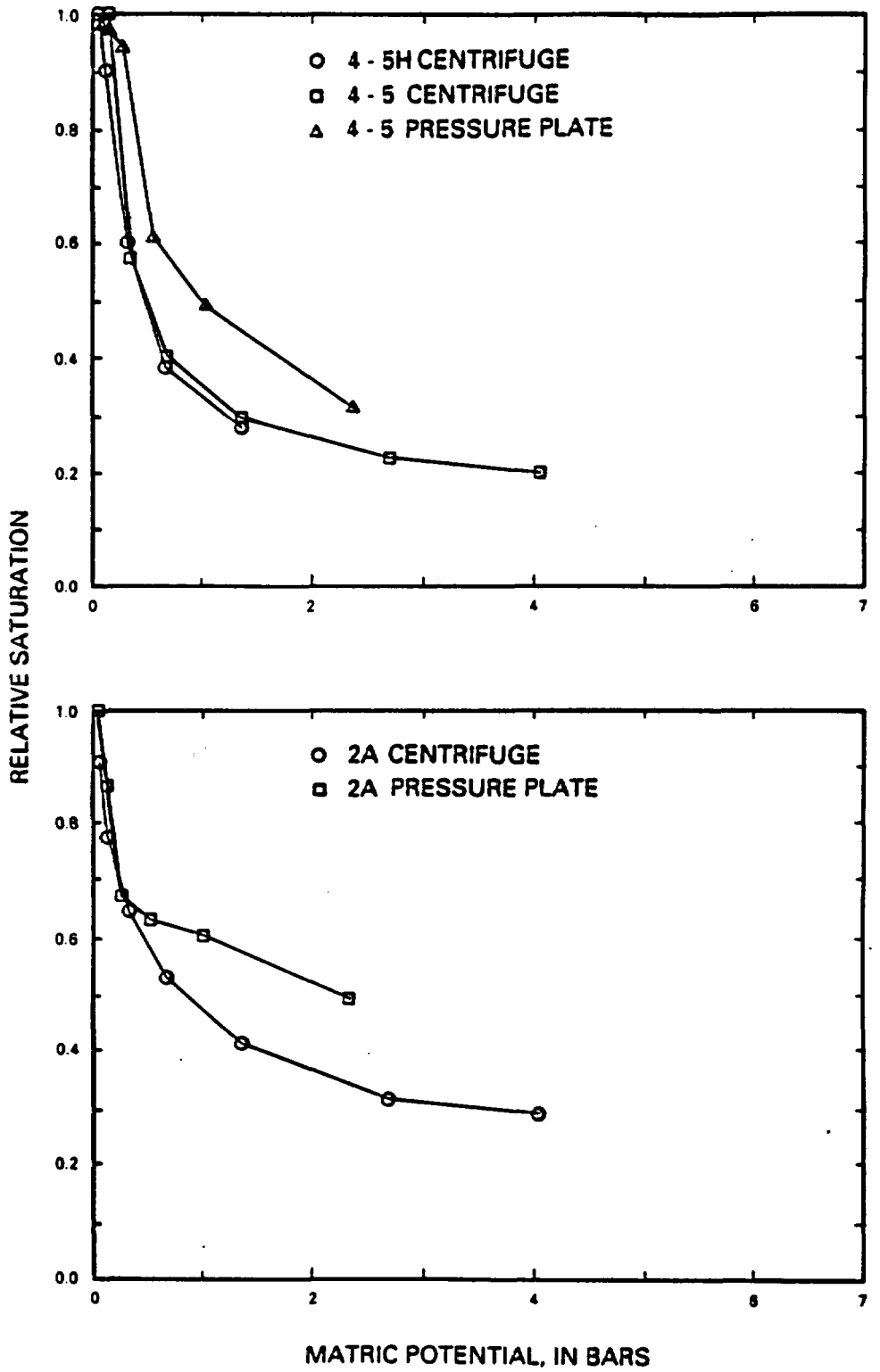

Figure II-1.--Water-retention curves for samples 4-5, 4-5H, and 2A determined using centrifuge and pressure plate methods.

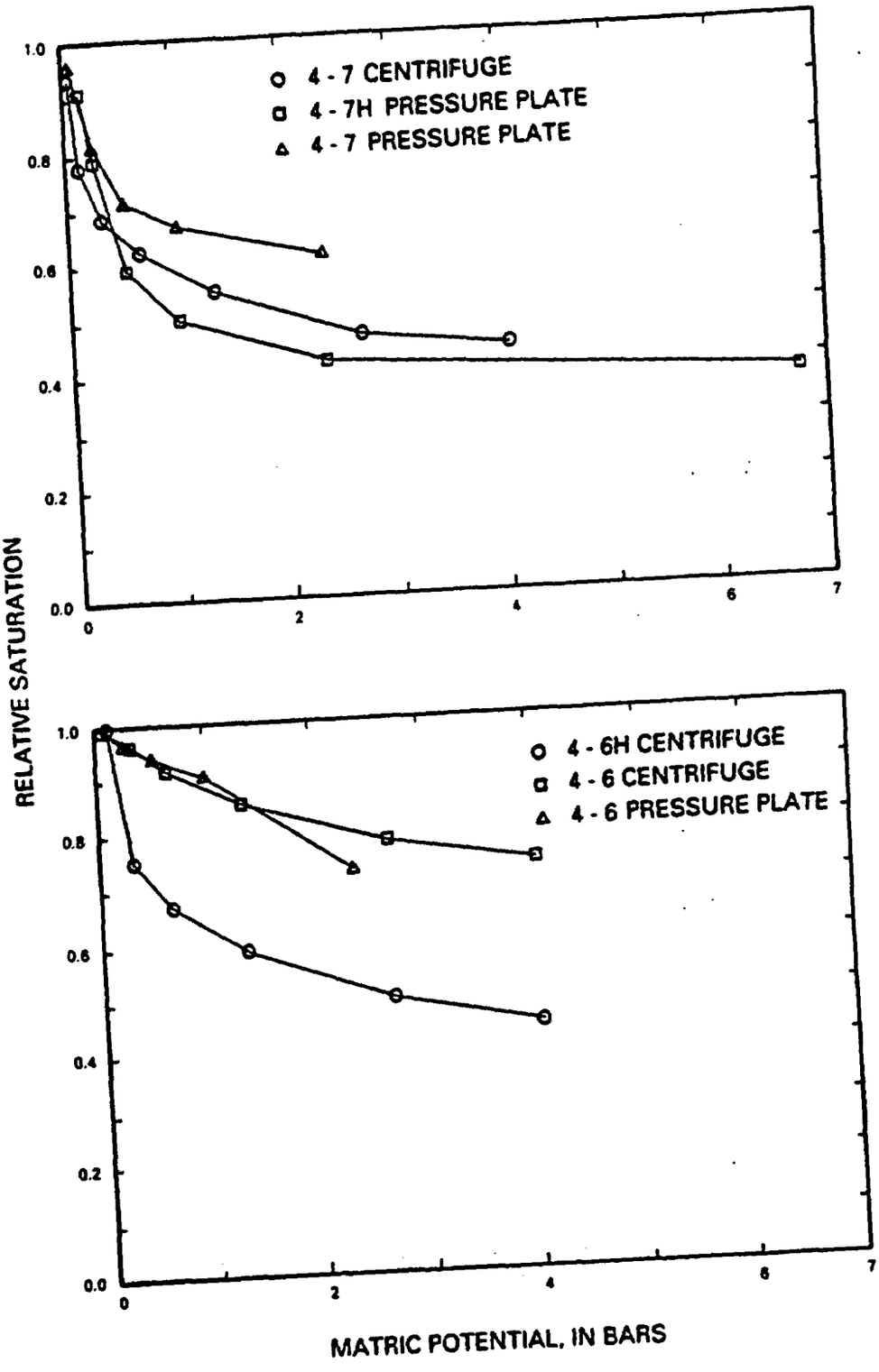

Figure II-2.--Water-retention curves for samples 4-7, 4-7H, 4-6, and 4-6H determined using centrifuge and pressure plate methods.

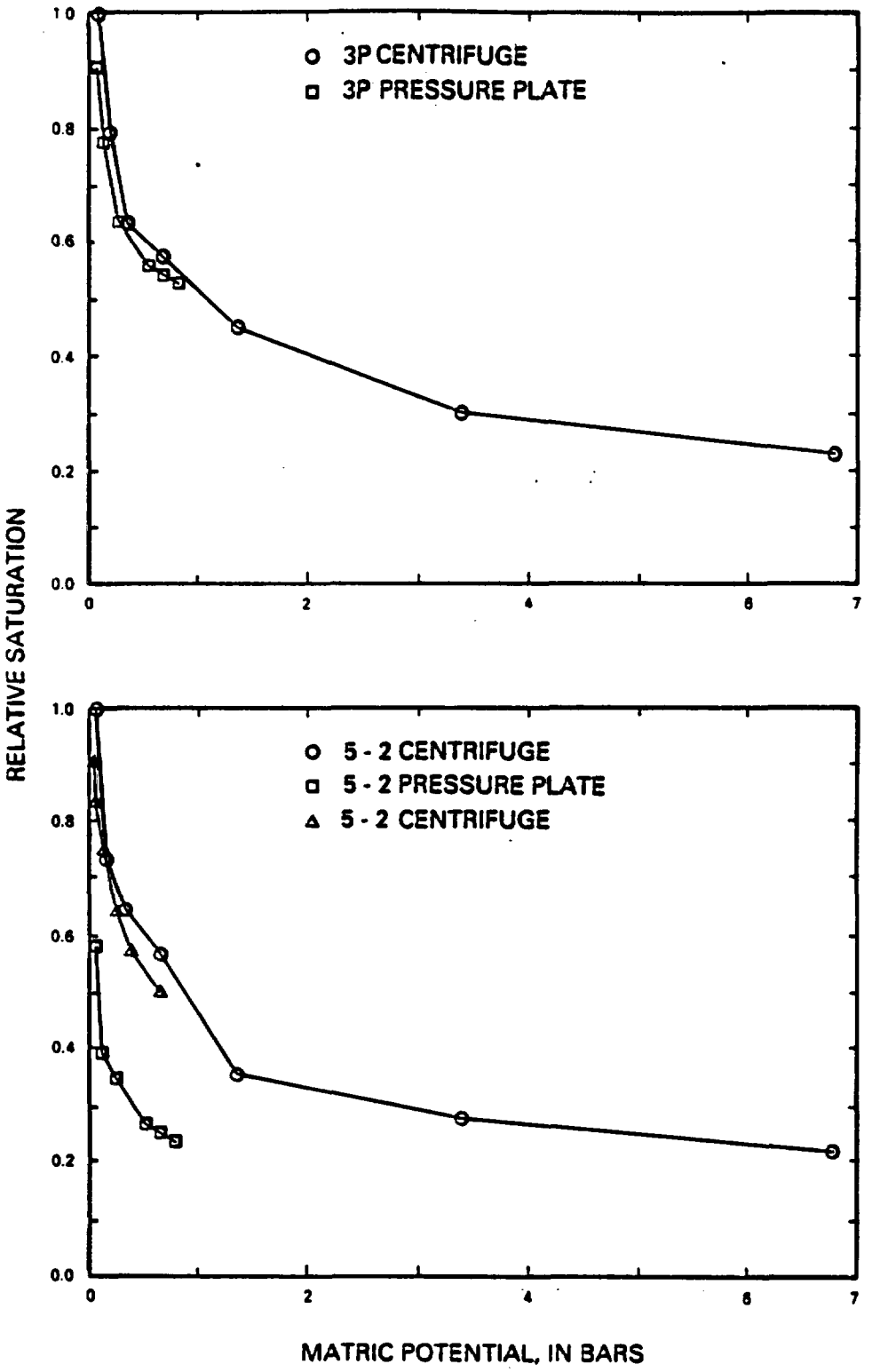

Figure II-3.--Water-retention curves for samples 3P and 5-2 determined using centrifuge and pressure plate methods.

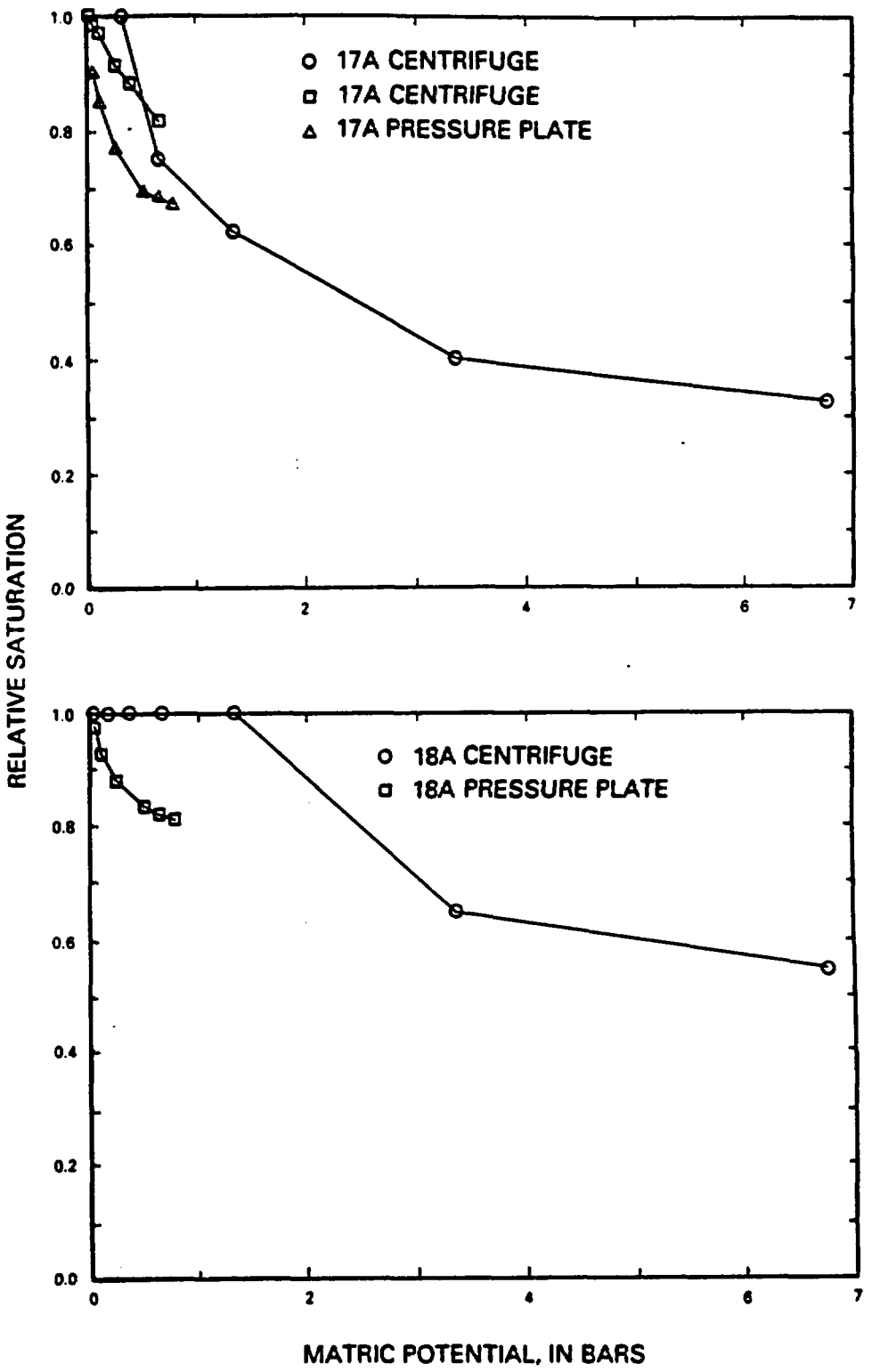

Figure II-4.--Water-retention curves for samples 17A and 18A determined using centrifuge and pressure plate methods.

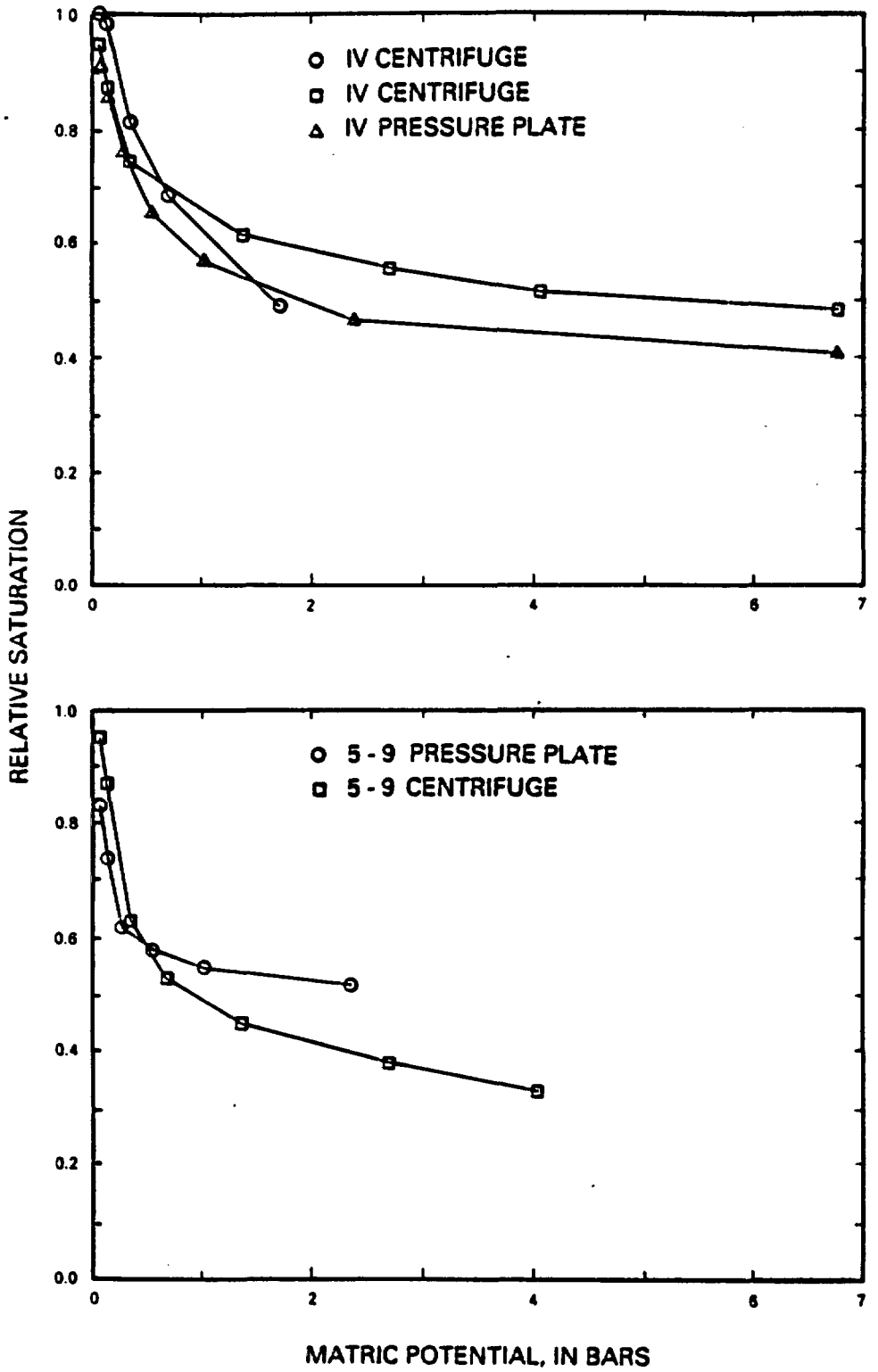

Figure II-5.--Water-retention curves for samples IV and 5-9 determined using centrifuge and pressure plate methods.

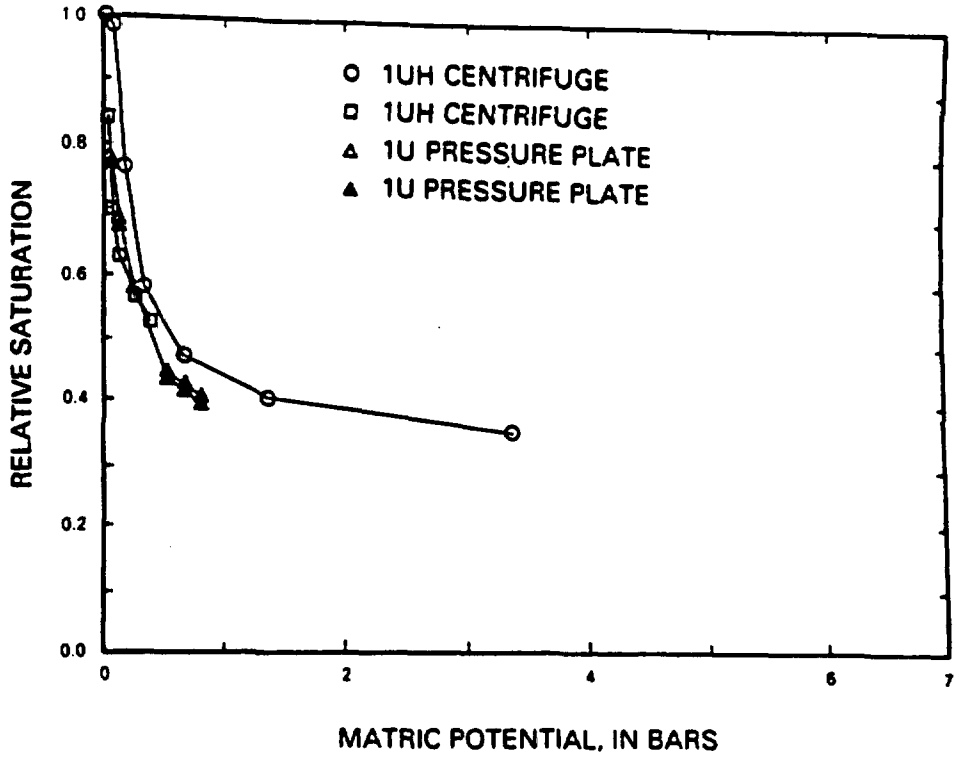

Figure II-6.--Water-retention curves for samples 1U and 1UH determined using centrifuge and pressure plate methods.

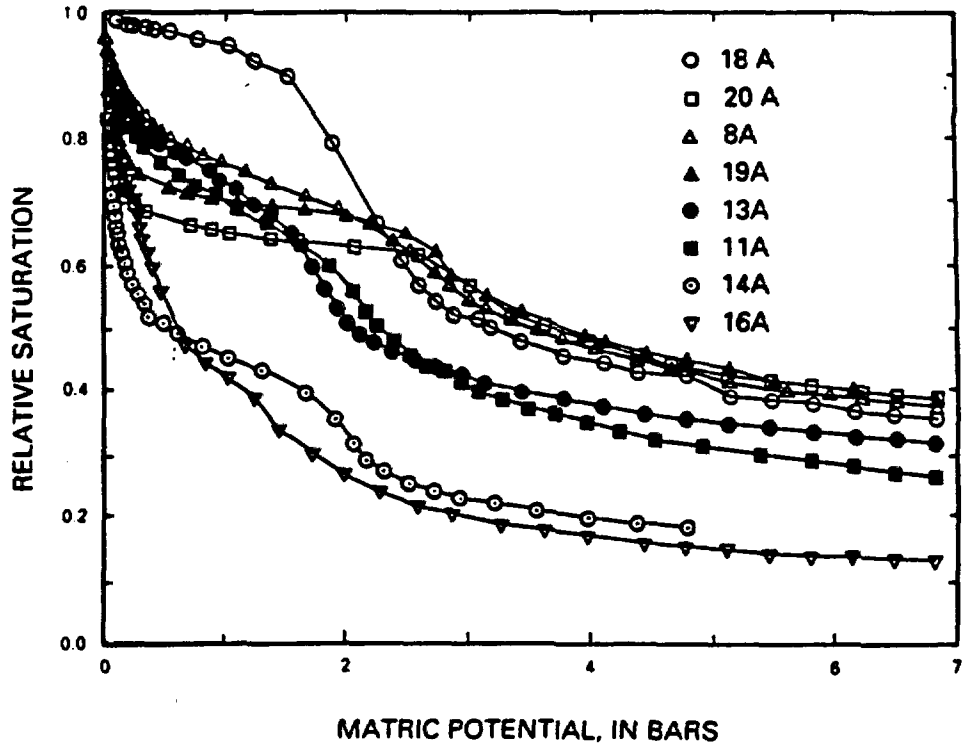

Figure II-7.--Water-retention curves calculated using mercury porosimetry for samples 18A, 20A, 8A, 19A, 13A, 11A, 14A, and 16A.

☆U.S. GOVERNMENT PRINTING OFFICE: 1991 - 576-003/45128

Eleipiess Informatsiya pp. 27 - 39

RESULTS OF THE USE OF THE POLARIZATION METHOD OF VERTICAL SEISMIC PROFILING (PM VSP) IN THE TERRITORY OF THE KRASNODAR REGION

Ye. I. Gal'perin, Yu. D. Mirzoyan, V. Ya. Oyfa.

The work was done for the purpose of analyzing the wave fields, bringing out the various types of waves, and studying the velocity section on the basis of P and S waves and determining the elastic properties.

PM VSP observations were made under conditions of mediums of complex constitution in the West Kuban depression (Kaluzh sector) and the mountainous part of the West Caucasus (Ubinka sector), under conditions of diapir tectonics on the Taman' (Fontalov sector), and also under platform conditions (Kushchevskaya sector), and others.

1. Study of wave fields. The southern edge of the West Kuban depression. Deposits from Mesozoic to Miocene, inclusive, enter into the make-up of the folds of the Kaluzh anticlinal zone on the southern edge of the West Kuban depression. Reflections from horizons in the Oligocene-Neogene complex are relatively stable and persistent over the sector. At large times (Eocene, Paleocene, Cretaceous) the record is complicated by wave interference caused by the inequalities curvature of the reflecting boundaries and by faults. Under these conditions the waves are not resolved by traditional methods.

PM VSP observations were carried out in the Kaluzh #60 hole to a depth of 2000 m, from two shotpoints 500 and 900 m from the hole. The vibrations were recorded by a three-point, three-component sonde with time-pulse modulation. Polar-positional correlation, using an array of 23 seismograms of fixed components, provided reliable distinction and tracing of

8.3.1.2.2.3
Encl. 2

direct (P and S) and reflected (PP and SS) waves.

In contrast to Z seismograms, the direct longitudinal wave P is traced on the records of the follow-up components (P) along the whole profile (Fig. 1). The direct S wave from both shotpoints was recorded at times of 1.2 and 1.5 sec, respectively. The S wave was most reliably distinguished on seismograms obtained from blasting material 5[00] [?].

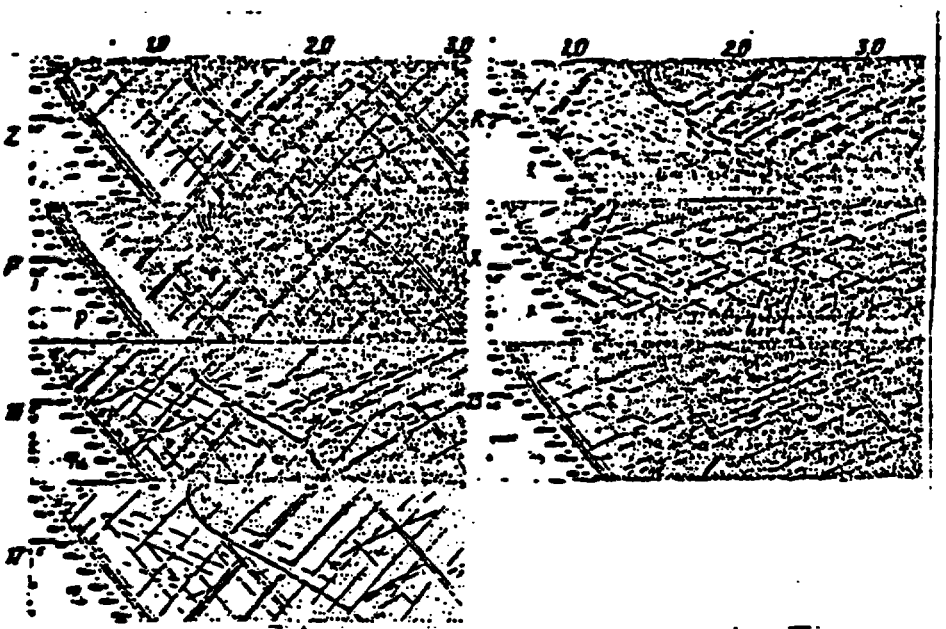

Fig. 1. Seismogram of recorded components (Kaluzh #60 hole, $\bar{l}$ = 500 m).

Longitudinal reflected waves PP are characterized by relatively high intensity. At times up to 3.8 sec, up to 10[12] reflections are observed, related to Neogene-Paleogene deposits. These waves, reflected from the base of the low-velocity zone (or from the surface), create an intensive field of incident waves and numerous interference zones. Converted waves (reflected and *transient), transverse reflections, and lateral PP waves also interfere with the distinction of PP waves. By using polar-positional correlation [PPC] it was possible to reduce the noise substantially and trace longitudinal reflections practically continuously.

* literally "trailing"

29

The regions of the follow-up components of PP waves are situated in the $\phi = 30°$, $\omega = 270-360°$ sector (Fig. 2). Apparent P-wave velocities vary within 1900-2400 m/s. With a record of stable shape, they are easily identified among themselves from the different shot points. Lateral waves with apparent velocities of 6700-7200 m/s are optimally recorded on the horizontal and inclined components in a substantial range of times.

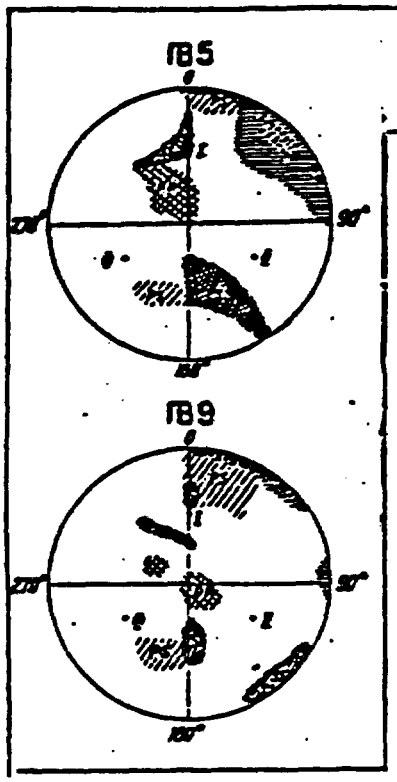

Fig. 2. Sectors of follow-up waves of different type (stereographic projection).

Converted reflected waves PS are extensively represented in the wave field. On seismograms of the Z component they are traced only in the beginning of the record to depths of 1300-1500 m. The follow-up components for PS waves are mainly the components close to the ray plane. In most of them the PS waves are polarized as SV vibrations. Their maximum recording time at the surface is 3.8 sec (the record is limited by the input into the computer), their apparent velocities increase rapidly with depth — from 500 m/s (at the surface) to 950 m/s (at the bottom of the whole). The field of incident converted waves is also intensive.

Reflected transverse waves SS are recorded at times of 1.6 to 3.8 sec. In this interval, up to 10 groups of vibrations are distinguished, related to the contacts of various lithostratigraphic complexes in the sequence of Cenozoic deposits, and deeper. Apparent SS-wave velocities vary within

900-1100 m/s, and the apparent frequencies are somewhat lower. Separation of PS and SS waves on the basis of V_H and frequencies is complicated, but it encounters no difficulties on the basis of the polarization criterion, as the regions where PS and SS waves are traced are different (Fig. 2). SS waves are polarized as SV vibrations.

The data obtained show that under the conditions of the highly deformed mediums of the West Kuban depression the use of PPC provides a reliable analysis of the wave field. The main types of waves are distinguished and traced on VSP profiles — longitudinal (P and PP), converted (PS), and transverse (S and SS), the joint interpretation of which can substantially enhance the precision and detail of investigations.

The data obtained on the Severskaya sector illustrate the possibilities of PM VSP in analyzing the wave field in the upper part of the section, where it is very complex as a rule. Let us examine the combination of recorded components of vibrations in the region of the follow-up components for various types of waves (Fig. 3). Despite the fact that the constitution of the region is not complicated and the medium is essentially axially symmetrical, the wave field consists of a fairly large number of waves of different type and nature. The follow-up component of the first longitudinal wave is the P component, the orientation of which coincides at every point with the direction of the vector of displacement in the P wave and varies along the profile. Longitudinal reflected waves are reliably traced on the Z and R components, and whereas longitudinal reflections of ascending waves are traced optimally on the inclined components at 0° azimuth, downward-reflected longitudinal waves are traced on components with 180° azimuth.

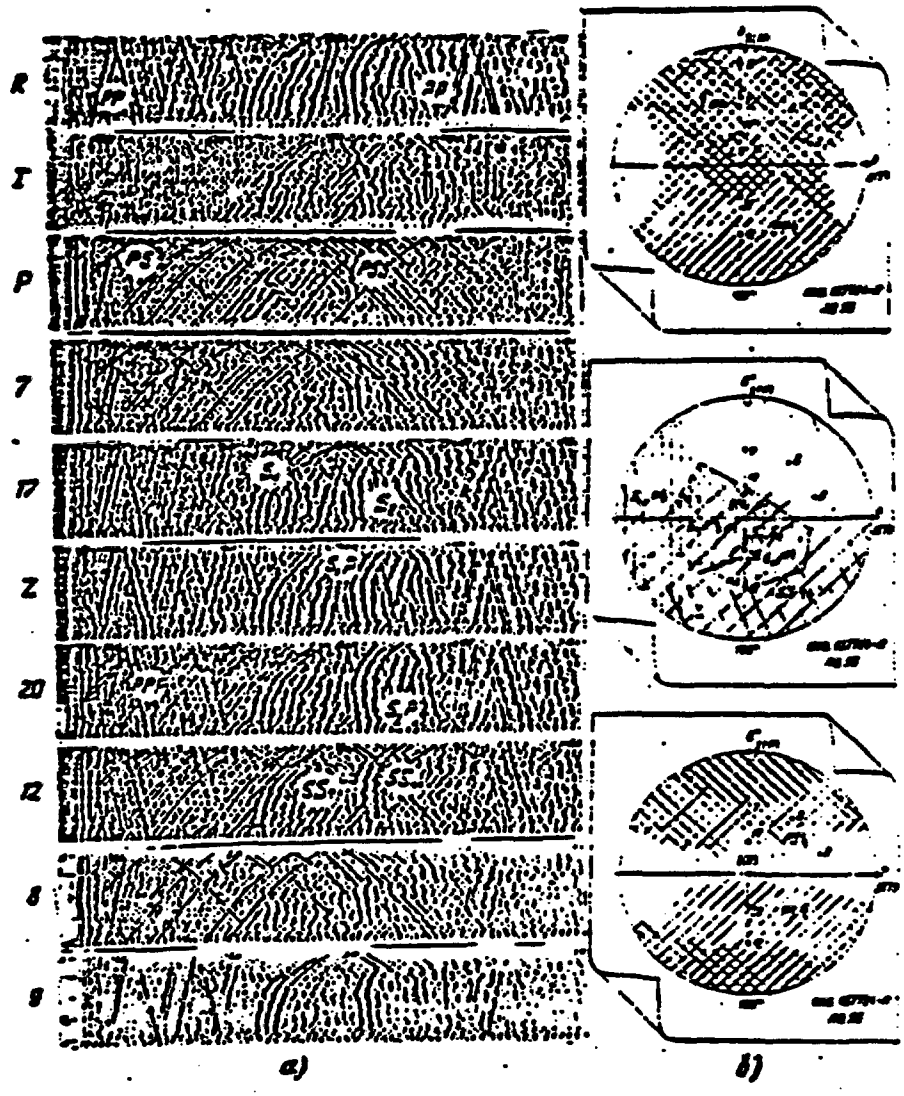

Fig. 3. Data of PM VSP observations (parametric hole in the Severskaya sector).

a - examples of seismograms of ~~fixed~~ مسجد components; b - fields of follow-up components of various types. [СНВ = hole, well]

The direct transverse waves S_1 and S_2 are optimally traced on component 17, and reflected ascending and incident transverse waves on the 20th component.

Converted ascending reflected waves of PS type are traced on components with 180° azimuth (20th, 12th), and incident multiples on components with 0° azimuth (P, Z).

SP converted waves are traced on components close to Z and the 20th. The examples given showed the complexity of the wave field in the upper part of the section and the possibilities of separating it into individual waves by studying the various components of the vibrations in space.

2. Study of velocities of longitudinal and transverse wave propagation. The possibility of simultaneous determination of P and S wave velocities is an important feature of the polarization method. The use of PPC in PM VSP made it possible to trace the direct longitudinal and transverse waves continuously along vertical profiles. From the P and S waves that are distinguished, traveltime curves of first arrivals are plotted, from which velocities and the V_p/V_s ratio are calculated.

The data obtained on various sectors indicate that the variation in longitudinal and transverse wave velocities are intimately related to the geology of the region and the lithology of the rocks.

Depth has a considerable effect on P and S wave velocities. Gravitational pressure of the overlying deposits leads to compaction of the rocks and to an increase in their elasticity and velocities. This is especially noticeable for the easily compacted Neogene deposits, the porosity of which is substantially reduced at low static pressures. As a result, an intensive increase in velocity with depth is observed: from 400-600 to 900-1100 m/s

in transverse and from 1500 to 2700 m/s in longitudinal waves, with vertical gradients of β_s = 0.66–0.5 sec^{-1} and β_p = 0.75–0.54 sec^{-1}.

An analogous regularity is observed in the Maykop deposits, where V_s and V_p velocity values increase to 1300 and 2700 m/s at a depth of 1800 m. The vertical gradient is about the same for longitudinal and transverse waves and decreases from 0.55 sec^{-1} to 0.35 sec^{-1}, which on the one hand is due to compaction and on the other to a general increase in sandiness in the Maykop beds.

The Paleogene deposits also react strongly to a change in depth. As a result, due to static loading of the overlying beds there occurs an increase in S-wave velocities from 800 m/s (H = 350 m) to 1300 m/s (H = 1850 m), and in P-wave velocities from 2100 to 3000 m/s. Transverse wave velocities in the Upper Cretaceous deposits were studied in only two holes: Cherkesskaya #3 and Mirnaya Balka #20. However, from the data of these holes also, an increase in V_s velocity with depth is observed, from 900–1100 to 1700–1900 m/s at depths of 200–1200 m. Longitudinal wave velocities at comparable depths ~~vary within~~ 2550–4200 m/s.

For the Lower Cretaceous deposits, the dependence of V_p and V_s on change in depth is more strongly manifested than in the Upper Cretaceous deposits. Here V_s velocities ~~range~~ from 1000 to 2000 m/s in the 100–2600 m depth interval, and longitudinal wave velocities from 2400–2600 to 4200 m/s.

There is little information on S-wave velocities in the Jurassic; they have been studied only in one hole, Cherkesskaya #3. These data show that the character of velocity variation with depth is much less clearly expressed in the Jurassic deposits and the fluctuations are fairly sub-

stantial in a relatively small depth range (1200 m), especially in longitudinal waves (V_p = 3500-4500 m/s, V_s = 1200-1500 m/s), and to a fairly large extent are caused by the lithologic composition of the rocks.

On the whole it can be observed that the particulars of the geology determine the values and range of variation of formation velocities. The highest V_p and V_s velocity values are obtained in holes in the mountainous part of the Caucasus, where the section consists of dense Cretaceous and Jurassic rocks.

Very low longitudinal and transverse wave velocity values are observed in the terrigenous deposits of the Taman' and in individual sectors under platform conditions (Il'inskaya, Kamenskaya, etc.). In sectors in the marginal zones of depressions, both longitudinal and transverse seismic wave velocities are somewhat higher than on the Taman' and on the platform, and are intermediate in value.

Differences in depth of rocks of the same age in different regions of western Ciscaucasia also cause considerable variations in average velocities of longitudinal and transverse waves.

The sandy-shaly Neogene-Paleogene deposits are characterized by low values of $V_{s_{av}}$. They increase slightly with depth — from 400-500 to 700-800 m/s (Fig. 4). The Mesozoic deposits have a higher level of average velocities — 750-1000 m/s in bedrock beneath the low-velocity layer and 1500-1600 m/s at depths to 2500 m. For longitudinal waves, larger gradients of $V_{av}(H)$ are noted for the first 600 m, due to the great variability of velocities in the upper part of the section. Deeper, the P and S wave velocity variations become similar, and the $V_{av}(H)$ curves stabilize at practically the same vertical gradients. The V_p/V_s velocity ratio in the

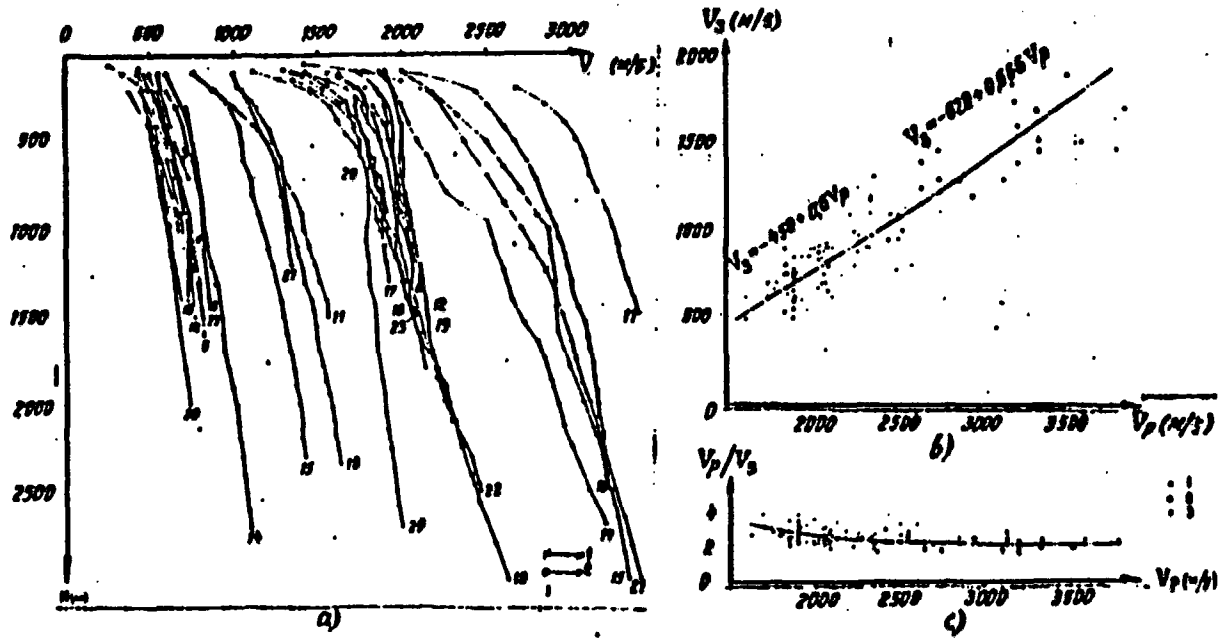

Fig. 4. Results of study of P and S wave velocities in 20 holes in western Ciscaucasia.

a - graph of average velocities of S (1) and P (2); b - dependence of V_s velocities on V_p; c - dependence of the V_p/V_s ratio on V_p (1 - Neogene-Oligocene deposits, 2 = Paleogene-Upper Cretaceous, 3 = Lower Cretaceous).

part of the section studied varies from 3.8 to 1.7 (Fig. 4c), which is typical of terrigenous deposits on the whole. And for the Neogene-Paleogene deposits the range of variation of V_p/V_s is rather substantial — 3.8-2.5, and for the Mesozoic formations it falls within 2.3-1.7 in the face of a considerable increase in longitudinal wave velocity values.

Analysis of the ratios of transverse and longitudinal wave velocities (Fig. 4b) showed that there is a relationship between them which may approximate a linear dependence:

for the Neogene-Paleogene $V_s^{N+Pg} = -0.45 + 0.6\ V_p$,

for the Mesozoic $V_s^{M} = -0.62 + 0.666\ V_p$.

35

The expressions obtained characterize the average values of V_p and V_s velocities. Analogous relationships were obtained in R. I. Yudina's work (1967).

The analysis that was made showed that the character of the variation of V_p and V_s velocities is not the same in different mediums. Sharper differentiation of the section is noted in the transverse wave velocities. On the whole the V_p/V_s ratio falls off monotonically with depth for the sandy-shaly Neogene-Paleogene deposits. For the dense Mesozoic rocks, places with anomalously high and low V_p/V_s are observed, related to the lithologic (limestones, dense sandstones, salt, etc.) and tectonic (geosynclinal regions, platform conditions, etc.) particulars of the regions investigated.

3. Study of elastic parameters. The elastic parameters depend on the structure and composition, depth and degree of deformation of the rocks. The set of elastic parameters and their correlational tracing can be a source of information on local variations in the geologic section in space. The elastic properties on the whole are determined by any one pair of con-

stants: Young's modulus E and Poisson's coefficient σ, Lamé's constants λ and μ, longitudinal and transverse wave velocities V_p and V_s, which are related by the following functions (A. K. Urupov, 1967):

$$V_p = \sqrt{\frac{\lambda + 2\mu}{\rho}} = \sqrt{\frac{E(1-\sigma)}{\rho(1+\sigma)(1-2\sigma)}},$$

$$V_s = \sqrt{\frac{\mu}{\rho}} = \sqrt{\frac{E}{\rho} \cdot \frac{1}{2(1+\sigma)}},$$

where ρ is the density of the rocks.

In PM VSP work, simultaneous study of V_p and V_s velocities is provided, i.e. information is obtained on all the elastic properties of the medium.

From the data on V_p and V_s velocities, Poisson's coefficient was calculated, and in sectors where the density of the rocks had been measured, Young's modulus and the shear modulus μ were also calculated; from these graphs the variations in elastic parameters with depth were plotted. From the σ(H) graph for the sandy-shaly Neogene-Paleogene deposits of western Ciscaucasia (Fig. 5), a systematic decrease in Poisson's coefficient with depth can be seen. And in the upper part of the section (100-800 m interval) the variation in Poisson's coefficient is very substantial (0.45-0.40). Below that, the σ(H) curve stabilizes and σ has values of 0.40-0.39. The values obtained for Poisson's coefficient agree on the whole with the theoretical values for plastic clays and fall within 0.45-0.38.

36

In the Kaluzh sector, where the section consists of interbedded clays, sands and sandstones, several layers from 200 to 800 m thick are distinguished on the basis of P-wave velocities, related to various lithostratigraphic complexes. On the basis of S waves the medium is more differentiated.

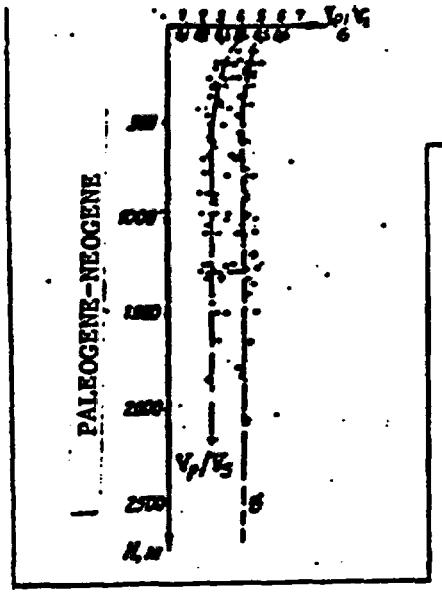

Fig. 5. Generalized results of PM VSP based on observations in 20 deep wells in western Ciscaucasia.

On the graphs (Fig. 6) there is noted an increase in V_s velocity and decrease in the V_p/V_s ratio and in σ on passing into the plastic clays of the Maykop. Comparison of the V_p/V_s and σ parameters with the E and μ elasticity moduli (depth 1200-1950 m) shows that higher values of Young's and the shear modulus correspond to low values of V_p/V_s and σ, this being more sharply expressed for Young's modulus. Obviously a decrease in porosity and density of the rocks occurs as overburden pressure increases. Therefore in the $\sigma(H)$ graphs there is observed a general lowering of Poisson's coefficient and increase in Young's modulus with depth. In many cases the lithology of the rocks definitely affects the elastic properties of the medium. It can be pointed out that this is the reason for the sharp increase in Young's modulus at the boundary of the Chokrak and Maykop deposits. No abrupt changes in density are observed in this part of the section. On the whole it should be stressed that the range of variation of the elastic parameters V_p/V_s, σ, E and μ is due to the particulars of the real medium.

By joint analysis of all the parameters, the section can be studied and subdivided in sufficient detail and fully, even under conditions of thin-bedded constitution. The data obtained on the elastic parameters of the medium in the Kaluzh sector (see Fig. 6a) are typical of sandy-shaly formations and close to the theoretical parameters.

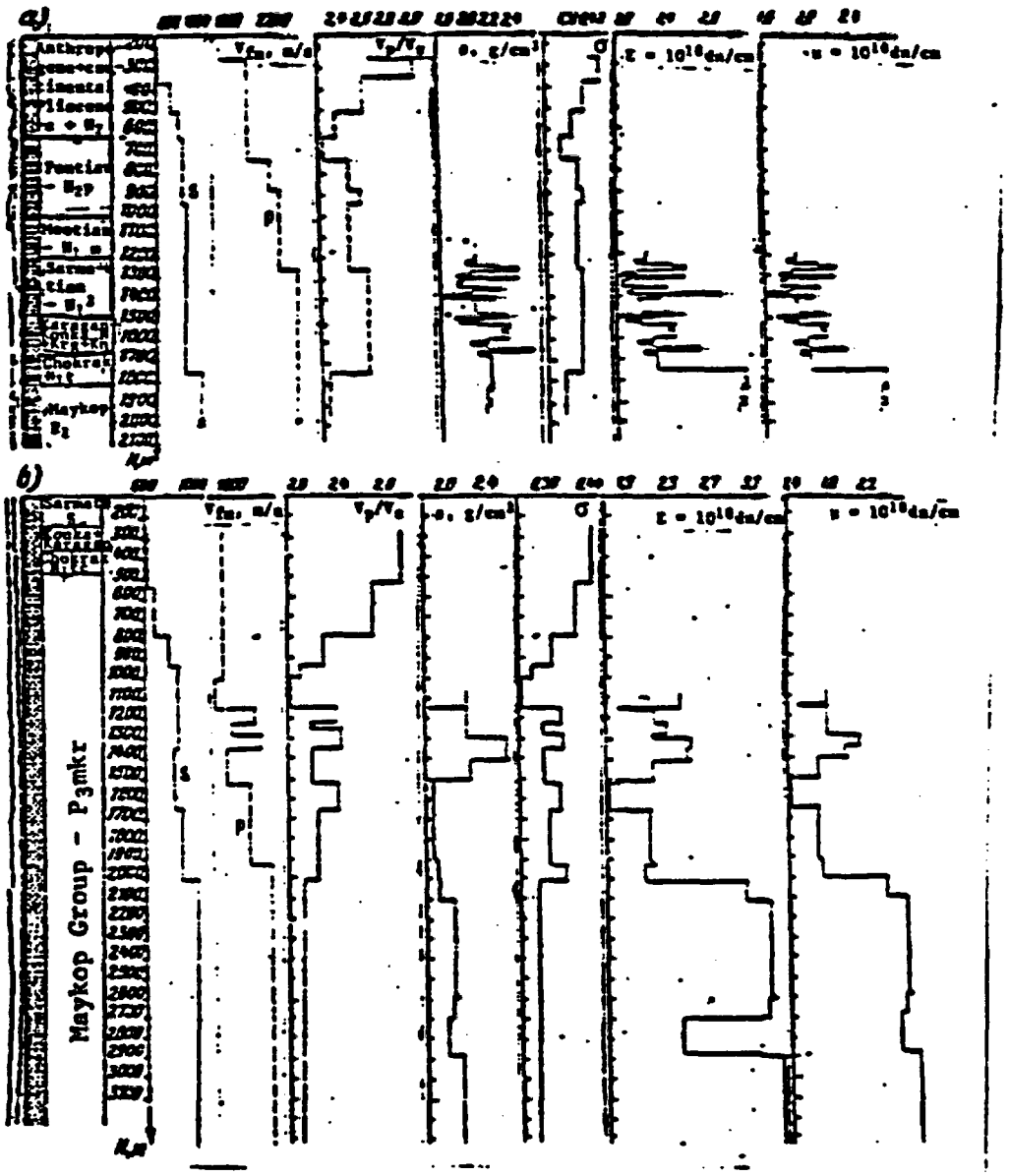

Fig. 6. Results of PM VSP in the Kaluzh #60 (a) and Taman' (b) holes.

On the Fontalov sector the section is less subdivided on the basis of density and seismic velocities (Fig. 6b), inasmuch as the greater part of it consists of a relatively homogeneous and thick sequence of Maykop sediments. In such places the variations in Young's and the shear moduli are more intensive (see Fig. 6b). Only V_s/V_p and Poisson's ratio were ascertained for the Paleogene-Mesozoic deposits (there are no data on the density of the rocks). The values of V_s/V_p for them vary within 3.0-1.7, and of σ, from 0.41 to 0.23, i.e. they decrease systematically with depth.

For the Cherkesskaya #3 hole the values of the elastic parameters are determined mainly by the lithologic particulars of the section and react well to variations in them. In particular, for the Paleogene deposits, which consist of interbedded clays and sandstones, the values of the Poisson's ratio σ are 0.41-0.43. In the Upper Cretaceous limestones they increase to 0.46, in the terrigenous clay packet of the Lower Cretaceous they decrease to 0.40, and then increase to 0.43-0.44 in the dense rocks (marls, sandstones, etc.) of the Lower Cretaceous and Jurassic.

Thus, the data obtained indicate that the use of the elastic parameters of the medium can be an effective means of predicting the geologic section, especially for studying the lithology of the rocks, their density, etc.

CONCLUSIONS

Testing and results of the use of PM VSP in mediums with different makeup in western Ciscaucasia make it possible to draw the following conclusions:

39

1. The observations made at internal points of the medium have confirmed that with the shots usually used in seismic surveying, transverse

waves are stably generated in addition to longitudinal, and converted reflected waves are produced on practically all sharp boundaries. Their joint study is of practical interest.

2. Use of PM VSP has made it possible to study the wave field under conditions of complexly constituted mediums, to distinguish longitudinal, transverse and converted waves related to boundaries situated at different depths which are of interest in exploration.

3. The use of PPC in PM VSP has provided reliable distinction of direct longitudinal and transverse waves and improved their tracing along the vertical profile, and also has offered the possibility of tracing reflected waves directly to the reflecting boundaries, thereby increasing the reliability and precision of the stratigraphic tie-in of the waves.

4. Joint study of the main types of waves distinguished (P, S, PP, PS, SS) has made it possible to study the velocity characteristics on the basis of longitudinal and transverse waves, and to obtain information on the elastic parameters of the medium, particularly their variation with depth and as a function of the lithofacies particulars of the section.

Ye. I. Gal'perin
(IFZ AN SSSR)

Yu. D. Mirzoyan, V. Ya. Oyfa
(Krasnodarneftegeofizika" Trust)

4055

CONF-8511172--6 MONTAZER wilson

HYDROGEOLOGY OF THE UNSATURATED ZONE, YUCCA MOUNTAIN, NEVADA

Parviz Montazer and William E. Wilson

U. S. Geological Survey
Denver, Colorado

Abstract

The unsaturated volcanic tuff beneath Yucca Mountain, Nevada, is being evaluated by the U.S. Department of Energy as a host rock for a potential mined geologic repository for high-level radioactive waste. Assessment of site suitability needs an efficient and focused investigative program. A conceptual hydrogeologic model that simulates the flow of fluids through the unsaturated zone at Yucca Mountain was developed to guide the program and to provide a basis for preliminary assessment of site suitability. The study was made as part of the Nevada Nuclear Waste Storage Investigations Project of the U.S. Department of Energy.

Yucca Mountain consists of a series of north-trending, fault-block ridges composed of volcanic rocks that have an eastward tilt of about 5° to 10°. The central block of Yucca Mountain, the primary area being evaluated for a potential repository, is bounded by major steeply dipping faults or fault zones. The central block is less faulted than the other blocks, but is transected by a few normal faults.

Thickness of the unsaturated zone is about 1,640 to 2,460 feet (500 to 750 meters). Based on physical properties, the rocks in the unsaturated zone are grouped for the purpose of this paper into five informal hydrogeologic units. From top to bottom these units are: Tiva Canyon welded unit, Paintbrush nonwelded unit, Topopah Spring welded unit, Calico Hills nonwelded unit, and Crater Flat unit. Welded units have a mean fracture density of 8 to 40 fractures per unit cubic meter, mean matrix porosities of 12 to 23 percent, matrix hydraulic conductivities with geometric means ranging from 6.5×10^{-6} to 9.8×10^{-6} foot per day (2×10^{-6} to 3×10^{-6} meter per day), and bulk hydraulic conductivities of 0.33 to 33 feet per day (0.1 to 10 meters per day). The nonwelded units have a mean fracture density of 1 to 3 fractures per unit cubic meter, mean matrix porosities of 31 to 46 percent, and saturated hydraulic conductivities with geometric means ranging from 2.6×10^{-5} to 2.9×10^{-2} foot per day (8×10^{-6} to 9×10^{-3} meter per day).

8.3.1.2.2.3 Encl. 2

Average annual precipitation at Yucca Mountain is estimated to be 5.9 inches (150 millimeters) per year; less than 0.002 inch (0.5 millimeter) per year becomes recharge to the saturated zone. Surface runoff is infrequent and of short duration, and no perennial streams exist in this area. Precipitation occurs during a few intense storms. Water infiltrates principally into the Tiva Canyon welded unit, but also into alluvial surficial deposits, the Paintbrush nonwelded unit, and the Topopah Spring welded unit, where these deposits or units are exposed at the land surface.

According to the conceptual model of flow in the unsaturated zone, percolation through the matrix principally occurs vertically in the welded units and both laterally and vertically in the nonwelded units. Fracture flow is predominant in the Tiva Canyon welded unit during intense pulses of infiltration and is insignificant in the Topopah Spring welded unit, except near the upper contact and near the structural features. Temporary development of perched water is possible near the structural features within and above the nonwelded units. This water drains into the structural features, and much of it travels directly to the water table.

Introduction

Yucca Mountain, Nevada, is one of several sites under consideration by the U.S. Department of Energy as the Nation's first mined geologic repository for storing high-level nuclear wastes. The U.S. Geological Survey has been conducting hydrologic, geologic, and geophysical investigations at Yucca Mountain and the surrounding region in order to help assess the suitability of the site for a repository. These investigations are part of the Nevada Nuclear Waste Storage Investigations (NNWSI) Project and are conducted in cooperation with the U.S. Department of Energy, Nevada Operations Office, under Interagency Agreement DE-AI08-78ET44802.

Under current conceptual designs, the waste would be placed within the thick section of unsaturated volcanic tuff that underlies Yucca Mountain. Investigations are underway to evaluate the hydrologic conditions, processes, and properties of the unsaturated zone at this site. This report proposes a conceptual flow model that has been developed from preliminary investigative results and from a general understanding of principles of unsaturated-zone flow.

Concept of a Repository in the Unsaturated Zone

The initial focus of the NNWSI Project in the late 1970's was to evaluate the suitability of placing a repository in the saturated zone beneath Yucca Mountain. However, the concept of storing waste in the unsaturated zone had been noted in the literature for nearly a decade (Winograd, 1972, 1974). Later, Winograd (1981) summarized the advantages associated with thick unsaturated zones, with special reference to the Nevada Test Site. Rosenbaum (1983) expanded on the concept and proposed design features that could enhance the isolation potential of this environment. At Yucca Mountain, as an understanding of the hydrologic system

began to develop, and as a result of the urging by various components of the scientific community, more careful consideration was given to the unsaturated zone. In 1982, investigative emphasis was shifted to the unsaturated zone.

One of the features of Yucca Mountain that permits consideration of a repository in the unsaturated zone is the very deep water table, generally about 1,640 to 2,460 ft (500 to 750 m) below land surface (Robison, 1984). As proposed, the repository would be constructed in the lower part of a densely welded fractured tuff, the Topopah Spring Member of the Miocene Paintbrush Tuff. These rocks appear to have geomechanical properties that permit the construction of stable openings and geochemical and thermal properties that are suitable for storage of waste (Johnstone et al., 1984). In addition, these rocks have a fracture density (Scott et al, 1983) that probably promotes rapid drainage of water. Moreover, a waste package and underground facility probably can be designed to enhance water drainage into the surrounding rocks with only minimal contact of the water with the waste package (Roseboom, 1983).

At the Yucca Mountain site, the unsaturated zone could be a natural barrier to radionuclide migration that would add to the barriers that exist in the saturated-zone system. The first component of the unsaturated-zone barrier is the very slow flux of water that occurs at Yucca Mountain. Next, a sequence of nonwelded porous tuff that overlies the potential host rock probably forms a natural capillary barrier to retard the entrance of water into the fractured tuff. A similar sequence of nonwelded tuff underlies the potential host rock. This underlying nonwelded tuff locally contains sorptive zeolites and clays that could be an additional barrier to the downward transport of radionuclides from a repository to the water table.

Although the general conditions described above probably exist, details of the hydrologic processes, conditions, and properties in the unsaturated zone are unknown. These details need to be known to characterize the site properly. The current lack of knowledge is the result of: (1) Lack of data, because of the newness of the focus on the unsaturated zone; (2) inadequacy of the general state of understanding of the physics of flow in thick, fractured-rock unsaturated zones in arid environments; and (3) lack of well-established techniques for testing and evaluating the hydrology of such unsaturated zones. To develop the information and understanding needed to assess the suitability of the unsaturated zone at Yucca Mountain within the time frame imposed by the national site-selection effort, an efficient and focussed investigative program needs to be conducted, and preliminary results need to be obtained quickly. A conceptual hydrologic model is needed to guide the program and to provide a basis for useful preliminary assessment of site integrity.

Purpose and Scope

The purpose of this paper is to describe the hydrogeologic setting of the unsaturated zone at Yucca Mountain and to examine some conceptual hypotheses of flow of fluids through this hydrogeologic system. Scott et al. (1983) presented an initial conceptual hydrogeologic model for the unsaturated zone at Yucca Mountain, based on detailed geologic, but very limited hydrologic, information. In this report, some of their concepts are examined and either supported or modified, and new concepts are developed. Much of this report is from a more detailed description given by Montazer and Wilson (1984).

Extensive geologic information but relatively few hydrologic data currently exist from the unsaturated zone in the Yucca Mountain area. Many uncertainties remain to be resolved concerning hydrologic conditions and processes. As a result, most of the concepts presented in this report are intentionally descriptive and conjectural, with little quantitative basis provided. However, for the sake of directness and simplicity of expression, the model is presented as if it were a true expression of the facts. The authors recognize, and the reader should be aware, that the proposed model probably is not the only reasonable description that could be made at this point, and it certainly is subject to revision and quantification as more data become available. However, the framework presented in this paper provides sufficient flexibility for future adjustments of the boundary conditions and, thereby, modification of the model.

General Setting

Yucca Mountain lies in and west of the southwestern part of the Nevada Test Site (NTS) (fig. 1). The NTS, used principally by the U.S. Department of Energy for underground testing of nuclear devices, is in Nye County, Nevada, about 65 mi (105 km) northwest of Las Vegas. The part of the mountain of principal interest is informally termed the central block, as outlined in figure 2. The central block approximately corresponds to the area under consideration by the U.S. Department of Energy for a repository, or the primary repository area.

Yucca Mountain is in the Great Basin physiographic province. The maximum altitude of the central block is 4,950 ft (1,509 m). Along the highest ridge within the central block (Yucca Crest, fig. 2), altitudes generally are between 4,806 and 4,840 ft (1,465 and 1,475 m). The crest is about 1,510 ft (460 m) above Jackass Flats (fig. 1) to the east, and about 590 ft (180 m) above Solitario Canyon to the west. Topography of the mountain is rugged. The mountain consists of a series of north-trending fault-block ridges underlain by volcanic rocks (fig. 2) that generally have an eastward tilt of 5° to 10° (Scott and Bonk, 1984). Washes, generally underlain by alluvium, dissect the mountain. The major washes in the northeastern part of the mountain are approximately parallel to a northwest-trending strike-slip fault system and drain southeastward to Fortymile Wash (figs. 1 and 2). The upstream reaches of most of the washes are parallel to the dips of the uppermost strata of the mountain.

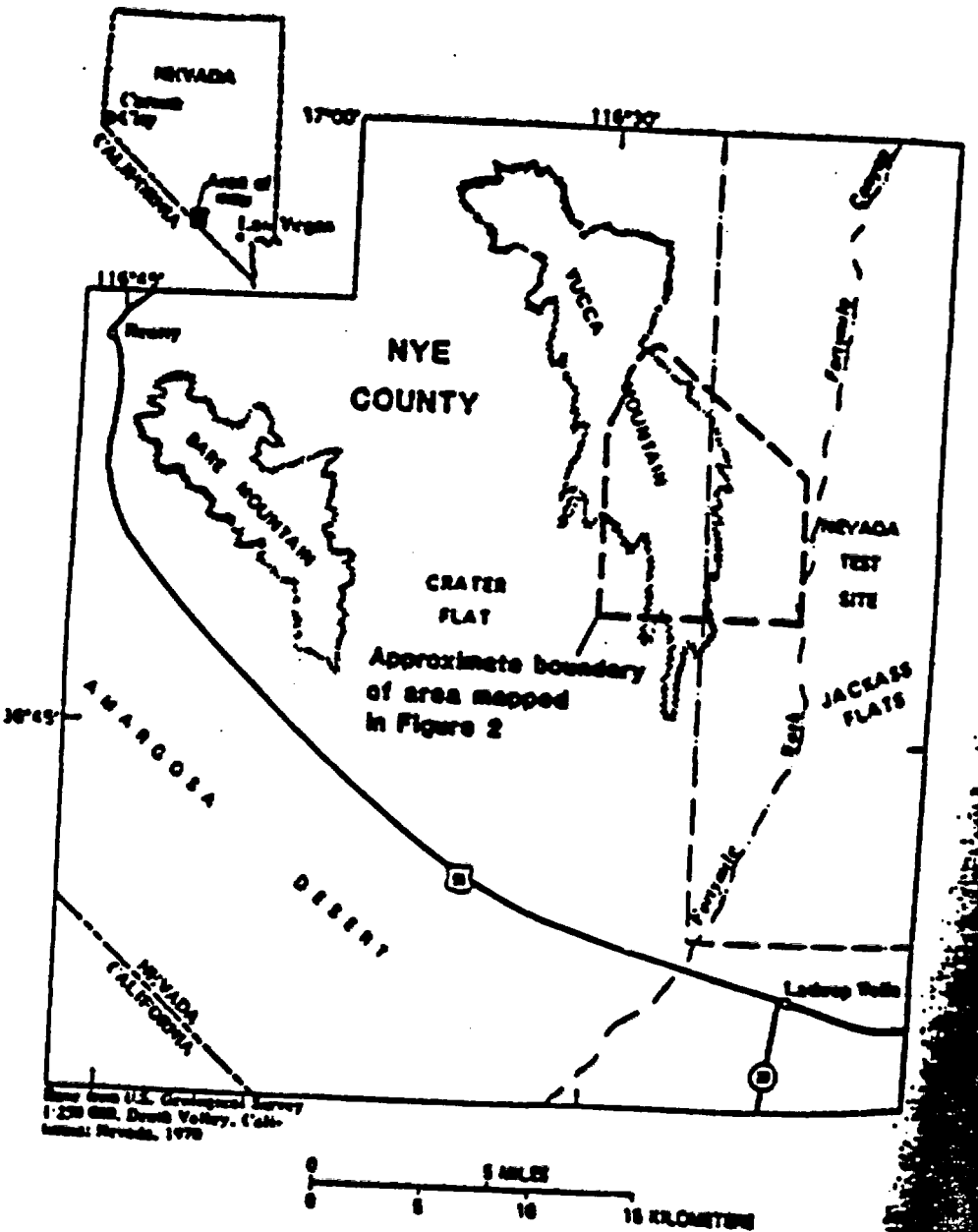

Figure 1.--Location of Yucca Mountain

Figure 2.—Generalized geologic map of the Yucca Mountain central block and vicinity (modified from Hoover and Wilson 1964; Scott and Castellanos, 1984).

The climate of the Yucca Mountain area is arid. Only recently have measurements of precipitation been made at Yucca Mountain itself. Average annual precipitation is estimated to be about 5.9 in/yr (150 mm/yr), based on information presented by Quiring (1983). Nearly three-fourths of the annual precipitation occurs during the cool season (October-April), generally as rainfall resulting from frontal systems moving through the region, and occasionally as snowfall. The altitude of Yucca Mountain is too low for snow to persist for more than a few days. Warm-season precipitation generally occurs as thunderstorms. No perennial streams exist in the Yucca Mountain area. Surface runoff is infrequent and of short duration, occurring only as a direct result of intense precipitation or rapid snowmelt.

Geologically, Yucca Mountain is within the Basin and Range province. The mountain is underlain for the most part by a thick sequence of silicic volcanic tuff of Miocene age (fig. 2). In the unsaturated zone of the central block, three formations occur beneath the alluvium. In descending stratigraphic order, these are: Paintbrush Tuff (including the Tiva Canyon, Yucca Mountain, Pah Canyon, and Topopah Spring Members), tuffaceous beds of Calico Hills, and Crater Flat Tuff (including the Prow Pass and Bullfrog Members). The Rainier Mesa Member of the Timber Mountain Tuff, which overlies the Paintbrush Tuff, also occurs locally in topographic lows near the central block (fig. 2). The Paintbrush Tuff is the only unit exposed in the central block (fig. 2). These formations and their component members are distinguished stratigraphically by their petrographic characteristics.

The physical properties within each formation vary considerably, which is largely due to variations in the degree of welding of the tuff. The physical-property boundaries do not correspond to rock-stratigraphic boundaries in most cases. Because the physical properties largely control the characteristics of water occurrence and flow in the unsaturated zone, the rocks have been grouped into hydrogeologic units, based principally on the degree of welding. Beneath the alluvium, five hydrogeologic units have been identified: Tiva Canyon welded unit, Paintbrush nonwelded unit, Topopah Spring welded unit, Calico Hills nonwelded unit, and Crater Flat unit.

In detail, the structural geology of the Yucca Mountain area is very complex, as reflected in the geologic map (fig. 2) and the hydrogeologic sections (fig. 3). The volcanic plateau of Yucca Mountain is broken into structural blocks bounded by major north-striking and west-dipping normal faults with as much as 330 ft (100 m) of vertical separation (Scott et al., 1983). Northwest-striking strike-slip faults with minor horizontal separation form a second type of faulting. Two dominant sets of fractures occur on Yucca Mountain; one set strikes north-northwest, and the other strikes north-northeast. Both fracture sets have steep to vertical dips. Fracture densities are substantially greater in welded tuff than in nonwelded tuff (Scott et al., 1983).

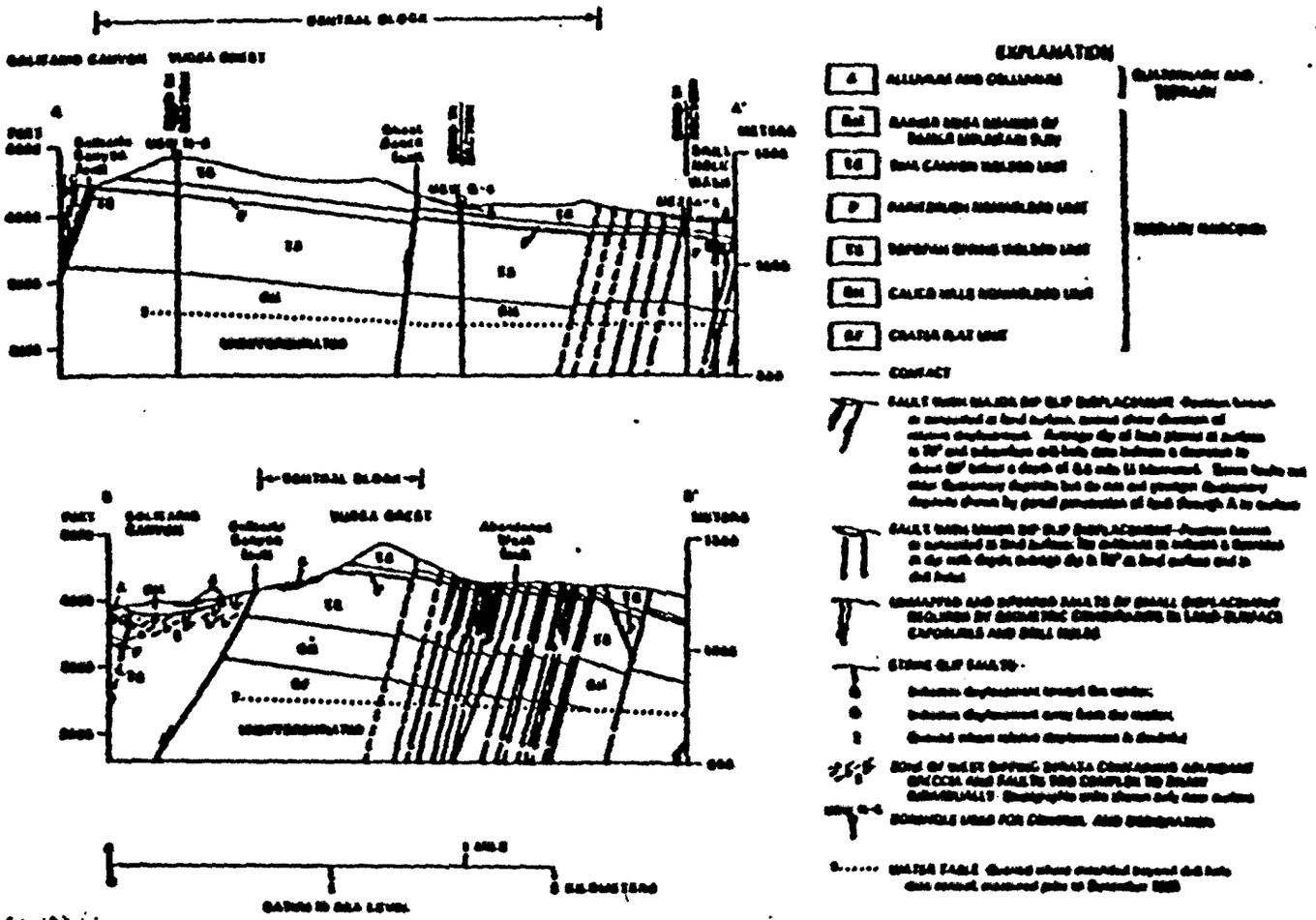

Figure 3.—Hydrogeologic sections across Yucca Mountain (from Montazer and Wilson, 1984; Spengler and Rosholt, 1984)

Table 1.--Summary of hydrologic properties of hydrogeologic units (modified from Montazer and Wilson, 1984)

[SD, unfavorable to density setting; SP, unrelated to porosity setting; VV, varies; UN, undetermined; 0, during; fractures/ft², fractures per cubic yard; fractures per cubic yard; Std. dev., standard deviation; cy/d, gallons per day]

Stratigraphic unit	Unit symbol	Hydrogeologic unit	Approximate range of thickness, in feet (meters)	Fracture density, in fractures per ft² (fractures per m²)	Assumed permeability		Fracture density (percent)			Matrix porosity (percent)			Value assigned to matrix porosity (percent)		Hydraulic conductivity in direction of ground-water flow	
					Matrix	Fracture	Number of samples	Mean	Std. dev.	Number of samples	Mean	Std. dev.	Number of samples	Mean	Std. dev.	No. of observations	Range
Alluvium	----	Alluvium	0-200 (0-100)	----	Generally substantial	----	--	--	----	--	--	--	--	----	----	----	----------
Upper Tuff Aquifer	UA	Upper Tuff aquifer unit	0-500 (0-150)	0-10 (0-30)	Negligible	Substantial	10	10	0.0	0	10	15	0	0.0	0.0	10	0.0 x 10⁻⁰ (0.0x10⁻⁰)
Upper Tuff Aquifer	UA, B	Intermediate confining unit	50-200 (15-100)	0 (0)	Moderate	Moderate	10	10	10	0	10	10	0	10	10	0	[illegible] ([illegible])
Upper Tuff Aquifer	UA	Upper Tuff aquifer unit	250-1000 (100-300)	0-20 (0-60)	Negligible	Substantial	10	10	0.0	10	10	10	10	0.0	0.0	10	[illegible] ([illegible])
Bedrock beneath Tuff aquifer	UA, B	Bedrock confining unit	2000-3000 (600-900)	0-2 (0-5)	(VV) Substantial (SD) Small to negligible	Moderate	0 (VV) (SD) 10	10	0.0	0 (VV) (SD) 10	10	0.0	-- (VV) (SD) --	----	----	0 (VV) (SD) 10	[illegible] ([illegible])
Lower Tuff Aquifer	LA	Lower Tuff aquifer unit	250-1000 (100-300)	0-2 (0-5)	(VV) Substantial (SD) Small to negligible	Moderate	0 (VV) (SD) 10	10	0.0	0 (VV) (SD) 10	10	0.0	-- (VV) (SD) --	----	----	0 (VV) (SD) 10	[illegible] ([illegible])
Bedrock beneath Tuff aquifer	UA, LP, B	Bedrock confining unit	400 (120)	0-10 (0-30)	Variable	Variable	10	10	0.0	10	10	0.0	--	----	----	10	[illegible]

[1] Thickness from geologic sections of Bentz and Smith (1984).
[2] Bentz et al. (1983).
[3] Estimated from physical properties.
[4] Montazer, Andersen (1984); U.S. Bureau of Land Management, written commun., (1983); Bentz et al.(1983); Thordarson (1983); Bentz and Wilson (1984).
[5] Sample values of effective permeability from Bentz and Wilson (1984) (1) and from U.S. Bureau of Land Management, written commun., 1983) (2) were applied to the geometric means of saturated hydraulic conductivity.

Hydrogeologic features that probably affect flow significantly in the unsaturated zone at Yucca Mountain include the presence of fractured porous media, layered units with contrasting properties, dipping units, bounding major faults, and a deep water table. These features probably result in the occurrence of phenomena such as fracture and matrix flow, retardation of flow by capillary barriers, infiltration into fractured rocks, lateral flow, perched ground water zones, and vapor movement. All these phenomena are incorporated into the conceptual model.

Conceptual Model of Flow

The manner in which flow probably occurs in the unsaturated zone at Yucca Mountain is described hereafter, based on: (1) Knowledge of the hydrogeologic framework; (2) application of the principles of unsaturated flow, including those described above; and (3) interpretation of some preliminary data from ongoing field and laboratory investigations. A detailed description of the conceptual model of flow is given in Montazer and Wilson (1984).

Average annual precipitation at Yucca Mountain is estimated to be about 5.9 in/yr (150 mm/yr). From analyses of the relationships among precipitation, recharge, and altitude, recharge to the saturated zone is conservatively estimated to be about 0.02 in/yr (0.5 mm/yr). This value probably approximates net infiltration, but this assumption may not be valid if the travel time through the recharging paths (structural features, for example) is longer than the duration of major phases of climatic cycles. Estimates of flux distributions are summarized as follows (Montazer and Wilson, 1984): (1) From 0.004 to about 4 in/yr (0.1 to about 100 mm/yr) of vertical flux may be occurring in the Paintbrush nonwelded unit, but the magnitude of vertical flux depends on the effectiveness of the capillary barrier at the lower contact of this unit; (2) the capacity to transmit lateral flux in the Paintbrush nonwelded unit is more than 4 in/yr (100 mm/yr), and the potential lateral volumetric flow rate is about twice the maximum estimated volumetric infiltration rate; (3) from 4×10^{-3} to 2×10^{-2} in/yr (0.1 to 0.5 mm/yr) of flux could be occurring in the matrix of the Topopah Spring welded unit, but flux in the fractures is unknown; (4) flux in the Calico Hills nonwelded unit is variable, but probably is limited to 2.4×10^{-4} in/yr (0.006 mm/yr) in the downward direction; and (5) results of analyses of the geothermal heat-flux data show that about 1×10^{-3} to 2×10^{-3} in/yr (0.025 to 0.05 mm/yr) of upward flux occurs in the Topopah Spring welded unit, possibly as a result of upward-moving vapor-saturated air, but the results are uncertain because of possible alternative interpretations of the data. These analyses indicate that the distribution of the vertical percolation is nonuniform in the unsaturated zone at Yucca Mountain. In the Paintbrush nonwelded unit, percolation rates probably are rapid and occur both vertically and laterally; but in the Topopah Spring welded unit, rates probably are extremely slow or even negative.

The general concept of flow at Yucca Mountain is illustrated in the section shown in figure 4. Flow through the unsaturated system is initiated by infiltration of precipitation at the land surface. Water infiltrates principally into the Tiva Canyon welded unit, but also into the alluvium, Paintbrush nonwelded unit, and Topopah Spring welded unit where they are exposed at the land surface. Water that is not lost by evapotranspiration and interflow becomes net infiltration and moves rapidly downward through fractures of the Tiva Canyon welded unit. The combination of dipping beds, permeability layering, and capillary-barrier effects results in significant lateral flow within the Paintbrush nonwelded unit toward the bounding structural features. Most of the infiltrated water is transmitted downward to the water table along structural features. Some flow occurs through the matrices from the Paintbrush nonwelded unit into the underlying Topopah Spring welded unit, but a capillary barrier retards flow into the fractures of the Topopah Spring welded unit.

At Yucca Mountain, nonuniform infiltration periodically produces moderately intense fluxes. Under such fluctuations of infiltration intensity, a zone of transient flux develops near the upper part of the unsaturated-zone profile. At depths greater than a few tens to hundreds of feet this transient flux dampens out, and flow reaches a more or less (quasi) steady-state condition. In the shallow transient zone, the phenomena of hysteresis and air entrapment are active. One of the effects of these phenomena is to start fracture flow in the Tiva Canyon welded unit much earlier in the wetting cycle than would be predicted by the drainage curves. Therefore, pulses of infiltration may cause rapid percolation down through the Tiva Canyon welded unit and into the Paintbrush nonwelded unit. Hysteresis effects may occur in the upper part of the Paintbrush nonwelded unit and result in rejection of downward percolating water much sooner than would be predicted by drainage curves. These effects result in the start of unsaturated lateral flow along the contact between the Tiva Canyon welded and the Paintbrush nonwelded units. Depending on the areal extent of the infiltration pulse, this lateral flow may reach structural features, where development of perched ground water is possible. This temporarily perched ground water drains into the structural flowpaths and much of it travels directly to the water table; some of this water moves into the matrix of the Paintbrush nonwelded unit and other units along the path.

Several factors indicate that the net flux in the Topopah Spring welded unit is very small. Fracture flow into the Topopah Spring welded unit is retarded by the capillary barrier that exists between the Paintbrush nonwelded unit and this welded unit. Limited fracture flow may occur near the upper contact of the Topopah Spring welded unit; however, movement into the matrix diminishes the extent of fracture flow in the deeper parts of this unit. Considering the potential for vapor transport under geothermal gradients, the net flux in parts of the Topopah Spring welded unit may be smaller than the downward liquid flux. Probably only a small part of the net infiltration is transmitted through the Topopah Spring welded unit. The excess net infiltration probably flows laterally into the structural features, which, therefore, transmit the major part of the infiltrated water.

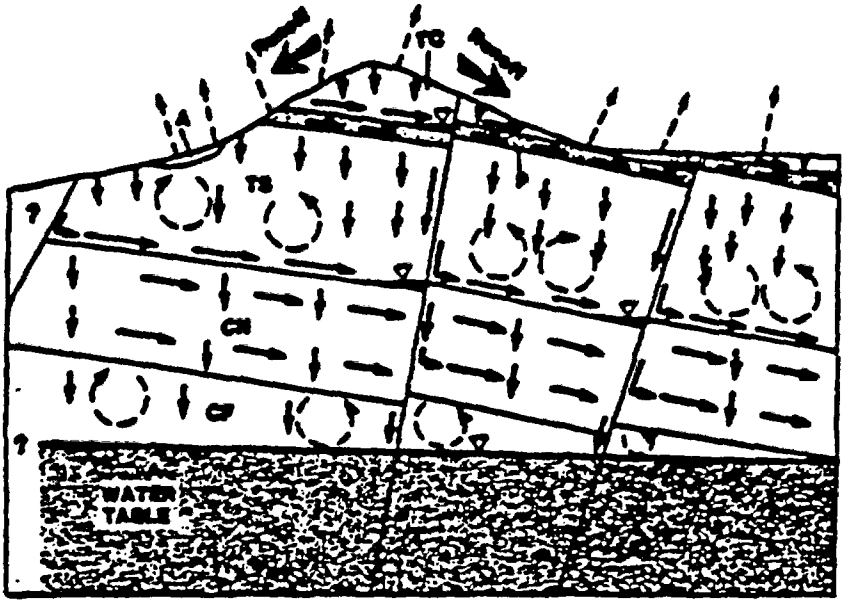

NOT TO SCALE

EXPLANATION

A ALLUVIUM	QUATERNARY AND TERTIARY	CONTACT
TC TIVA CANYON WELDED UNIT	TERTIARY (MIOCENE)	DIRECTION OF LIQUID FLOW
P PAINTBRUSH NONWELDED UNIT		DIRECTION OF VAPOR MOVEMENT
TS TOPOPAH SPRING WELDED UNIT		PERCHED WATER
CH CALICO HILLS NONWELDED UNIT		
CP CRATER FLAT UNIT		

Figure 4.--Generalized section across Yucca Mountain showing conceptualized flow regime. Lengths of solid arrows show relative magnitudes of fluxes (modified from Montazer and Wilson, 1984).

Flow enters the Calico Hills nonwelded unit either from the matrix of the Topopah Spring welded unit or through structural flowpaths. Most structural features probably become hydraulically discontinuous as they cross the Calico Hills nonwelded unit. Some water reaches the water table through these features, but perched water and down-dip flow may occur along the upper contact of the Calico Hills nonwelded unit. This laterally moving water percolates downward into the matrix of the Calico Hills unit. Vertical flux through this unit probably is limited to 2.4×10^{-4} in/yr (0.006 mm/yr). Lateral flow probably occurs within this unit, but may not be as significant as the lateral flow within the Paintbrush nonwelded unit.

Structural features transect a variety of welded and nonwelded tuff units. Variations in properties of these tuff units could result in local perching above or within the nonwelded units in the vicinity of these structural features. This perched water may take a variety of pathways: (1) it may move laterally along the upper contact or within the nonwelded unit; (2) it may move downward through the nonwelded unit; or (3) it may move downward along the structural pathway. The result is an uneven distribution of moisture content within the unit in the vicinity of the structural feature. Ultimately, the water flows through the Calico Hills nonwelded unit and reaches the water table, either beneath the central block, or at the structural features immediately east of the block, or further east, where the water table is within the Topopah Spring welded unit.

Conclusions

The authors believe that the conceptual model described in this report is based on an appropriate hydrogeologic framework. Therefore, the degree to which the model accurately describes flow conditions at Yucca Mountain depends in large measure on the appropriateness of the assumptions used and on the boundary flux assigned to the model. Many of the processes incorporated in the model are based on the presumed substantial difference between the relatively slow percolation rate in the Topopah Spring welded unit beneath the block and the relatively large net infiltration entering the system. Several types of evidence support the slow percolation rate. However, the net infiltration at Yucca Mountain principally is based on an application of regional analyses; thus, the rate is very uncertain. Further definition of this rate is required to assess the accuracy of the flow conditions described by the model.

The model can provide a basis for making preliminary assessments of the hydrologic integrity of a potential repository in the unsaturated zone at Yucca Mountain. Such assessment modeling needs to incorporate the phenomena of fracture flow, lateral flow, capillary barriers, flow through structural features, and hysteretic effects.

The model also can be a guide for further investigations of the hydrology of the unsaturated zone at Yucca Mountain. Such investigations could include evaluations of: (1) flux in the shallow hydrogeologic unit to identify more directly the net infiltration rate; (2) flux in the major structural features bounding the central block, to assess the significance

of such features and similar ones that might exist or develop in the central block; (3) the presence or absence of perched water bodies, to assess their impact on repository construction and integrity; (4) two-phase flux in the Topopah Spring welded unit, to evaluate the potential for upward-moving water; and (5) the assumptions made in developing the conceptual model, to assess the appropriateness of the model and to provide a basis for its revision.

References

Anderson, L.A. 1981. Rock property analysis of core samples from the Yucca Mountain UE25a-1 borehole, Nevada Test Site, Nevada. U.S. Geological Survey Open-File Report 81-1338. 15 pp.

Johnstone, J.K., R.R. Peters and P.F. Gnirk. 1984. Unit evaluation at Yucca Mountain, Nevada Test Site--Summary report and recommendation. Sandia National Laboratories Report SAND83. 85 pp.

Montazer, Parviz, and W.E. Wilson. 1984. Conceptual hydrologic model of flow in the unsaturated zone, Yucca Mountain, Nevada. U.S. Geological Survey Water-Resources Investigations Report 84-4345. 55 pp.

Quiring, R.F. 1983. Precipitation climatology of the Nevada Test Site. National Oceanic and Atmospheric Administration, National Weather Service Report WSNSO 351-88. 34 pp.

Robison, J.H. 1984. Ground-water level data and preliminary potentiometric-surface maps of Yucca Mountain and vicinity, Nye County, Nevada. U.S. Geological Survey Water-Resources Investigations Report 84-4197. 8 pp.

Roseboom, E.H. 1983. Disposal of high-level nuclear waste above the water table in arid regions. U.S. Geological Survey Circular 903. 21 pp.

Rush, F.E., William Thordarson and Laura Bruckheimer. 1983. Geohydrologic and drill-hole data for test well USW H-1, adjacent to Nevada Test Site, Nye County, Nevada. U.S. Geological Survey Open-File Report 83-141. 38 pp.

Scott, R.B. and Jerry Bonk. 1984. Preliminary geologic map of Yucca Mountain with geologic sections, Nye County, Nevada. U.S. Geological Survey Open-File Report 84-494, scale 1:12,000.

Scott, R.B. and Mayra Castellanos. 1984. Stratigraphic and structural relations of volcanic rocks in drill hole USW GU-3 and USW G-3, Yucca Mountain, Nye County, Nevada. U.S. Geological Survey Open-File Report 84-491. 121 pp.

Scott, R.B., R.W. Spengler, Sharon Diehl, A.R. Lappin and M.P. Chornack. 1983. Geologic character of tuff in the unsaturated zone at Yucca Mountain, southern Nevada, in Mercer, J.W., Rao, P.S.C., and Marine, I.W., eds., Role of the unsaturated zone in radioactive and hazardous waste disposal. Ann Arbor Science, Ann Arbor, Mich. pp. 289-335.

Thordarson, William. 1983. Geohydrologic data and test results from well J-13, Nevada Test Site, Nye County, Nevada. U.S. Geological Survey Water-Resources Investigations Report 83-4171. 57 pp.

Weeks, E.P. and W.E. Wilson. 1984. Preliminary evaluation of hydrologic properties of cores of unsaturated tuff, test well USW H-1, Yucca Mountain, Nevada. U.S. Geological Survey Water-Resources Investigations Report 84-4193. 30 pp.
Winograd, I.J. 1972. Near surface storage of solidified high-level radioactive waste in thick (400-2,000 feet) unsaturated zones in the Southwest. Geological Society of America Abstracts with Programs, v. 4, no. 7, pp. 708-709.
Winograd, I.J. 1974. Radioactive waste storage in the arid zone. Transactions of the American Geophysical Union (EOS), v. 55, no. 10, pp. 884-894.
Winograd I.J. 1981. Radioactive waste disposal in thick unsaturated zones. Science, v. 212, no. 4502, pp. 1457-1464.

Biographical Sketch

Parviz Montazer received his bachelor of science degree from Pahlavi University, Shiraz, Iran, in 1972, and his master of science degree and his doctor of philosophy degree from Colorado School of Mines, Golden, Colorado, in geological engineering in 1978 and 1982, respectively. He has been employed by the Water Resources Division of the U.S. Geological Survey in Denver, Colorado, since 1983. His research interests include flow through fractured rocks and hydrology of deep unsaturated zones. He is currently the project chief for unsaturated-zone hydrologic studies of Yucca Mountain, Nevada Test Site. His address is: U.S. Geological Survey, Box 25046, MS 416, Denver Federal Center, Denver, Colorado 80225.

William E. Wilson received his bachelor of arts degree in geology from Harvard College in 1956 and his doctor of philosophy degree in geology from the University of Illinois in 1963. Since 1963, he has been employed as a hydrologist by the U.S. Geological Survey. He has conducted water-resources investigations in Connecticut and Florida and is currently Chief of the Nuclear Hydrology Program in Denver, Colorado. In this position he is managing a program of hydrologic investigations at Yucca Mountain, Nevada, to help evaluate the suitability of this site as a potential repository for high-level nuclear waste. His address is: U.S. Geological Survey, Box 25046, MS 416, Denver Federal Center, Denver, Colorado 80225.

Applications Data

BECKMAN INSTRUMENTS INC., SPINCO DIVISION, P.O. BOX 10200, PALO ALTO, CA ■ 94304 ■ (415) 857-1150

Capillary Pressure Measurements in Reservoir Rock Cores Using the Centrifuge

By Brian Skuse

Introduction

Capillary pressure measurements are essential for the complete characterization of an oil reservoir. A plot of capillary pressure vs. saturation for a rock core, called the capillary pressure curve, can be used either to calculate reserves or in reservoir-simulation computer routines. These curves also provide data on the irreducible water saturation of a reservoir rock and the entry pressure of oil into a water-saturated reservoir or cap rock.

Three static (non-flow) methods of obtaining capillary pressure curves are the porous plate, mercury injection, and centrifuge methods. The centrifuge method compares favorably with the other methods of preparing capillary pressure curves. The porous plate method may require weeks whereas the centrifuge can take only days. Any fluid combination (gas-oil, gas-water, water-oil, gas-water-oil) can be used in the centrifuge. The centrifuge method is nondestructive and the results are reproducible. Both drainage and imbibition curves can be produced. Interphase pressure differences up to 1000 psi can be developed in an air-liquid system, extending the range of permeability down to one millidarcy (md) or less. Unconsolidated samples can be evaluated on a centrifuge.

The seminal work on the centrifuge method is the 1945 paper of Hassler and Brunner.[1] Slobod *et al.*[2] demonstrated in 1951 the virtues of simplicity, reproducibility, and speed in the centrifuge method, and its good correlation with the porous plate method. They also indicated the very high pressure differences attainable between the phases. Marx[3] discussed the use of the centrifuge in a gravity drainage investigation. Hoffman[4,5] performed dynamic (time-dependent) measurements of saturation in core samples using a constantly accelerated centrifuge, with considerable time savings. Donaldson[6] used the centrifuge for capillary pressure measurements in a study of wettability. Szabo[7] extended the method to include imbibition capillary pressure curves. He also used the centrifuge to measure electrical resistivity as a function of saturation. Samaroo and Guerrero[8] used a centrifuge to measure the effects of temperature on drainage capillary curves.

Hagoort[9] and Van Spronsen[10] have used the centrifuge to make two- and three-phase relative permeability measurements. In this application the centrifuge method mitigates both the capillary end effect and the viscous instability of gas displacing liquid.

Principles of the Method

We discuss here the principles of obtaining and interpreting centrifuge data for the case of a drainage capillary pressure curve and illustrate for the air-water case. A fully water-(brine)-saturated core sample is placed on a water-wet semipermeable membrane located in a holder in a centrifuge rotor (see Figure 1). This arrangement permits one to measure the volumes of water expelled from the core and replaced by air in the pore space. The first data point is obtained at a low centrifugal field by selecting a low rate of rotation. The expelled water volume is measured until it no longer changes. The volume of water remaining in the core is divided by the core's total pore volume to give an average water saturation value, $\bar{S}_w$. Subsequent points are obtained by a series of increasing rates of rotation.

At hydrostatic equilibrium the capillary pressure at every position is equivalent to the difference in hydrostatic pressure between the phases, i.e.,

$$P_c(r) = \frac{\Delta\rho\omega^2}{2}(r_c^2 - r^2) \qquad (1)$$

where r represents distance from center of rotation, r_c the radius of the core bottom, $\Delta\rho$ the difference between the density of the phases, and ω the rate of rotation in radians/second.

For each value of $P_c(r)$ there is a corresponding value of water saturation $S_w(r)$ at each radial position r, and both may vary substantially from one end of the core to the other. The essential

BECKMAN

8.3.1.2.2.3
Encl. 2

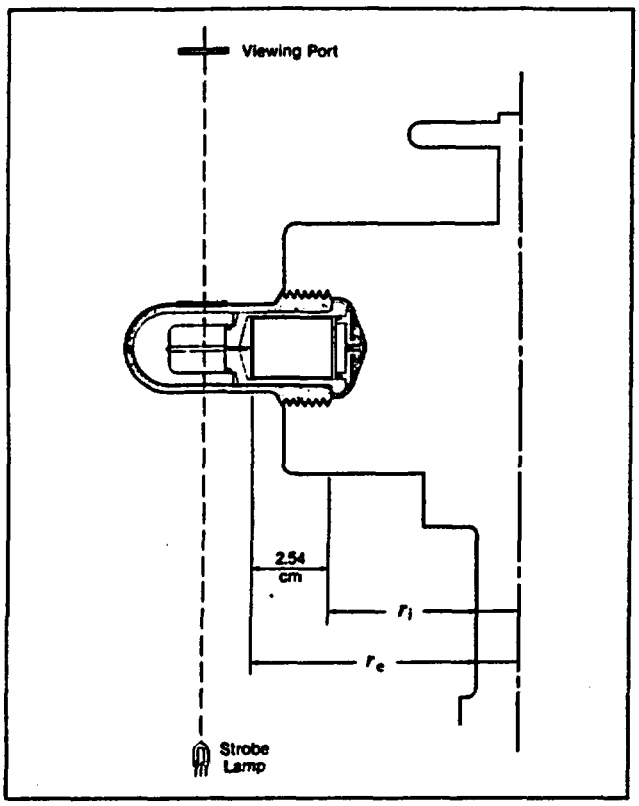

Figure 1. *Cross-Section of Type PIR-20 Rotor.*

problem one must solve to get a capillary pressure curve is to relate P_c to its appropriate S_w.

Hassler and Brunner proposed a method for doing this in 1945,[1] and we will illustrate their method here. They compute the capillary pressure and saturation at the top face of the core ($r = r_i$). Using their nomenclature,

$$P_c(r_i) = z = \frac{\Delta\rho\omega^2}{2}(r_e^2 - r_i^2) \tag{2}$$

and

$$S_w(r_i) = S_w(z).$$

The water saturation at the top face of the core is obtained from the relation

$$S_w(z) = \frac{d}{dz}[z\bar{S}_w(z)] \tag{3}$$

Hassler and Brunner indicated that this is actually an approximation to the correct value for $S_w(z)$, accurate enough for $r_i/r_e \geq 0.70$, and proposed an iterative technique to improve the approximation, not discussed further here.

The Hassler-Brunner theory rests on several assumptions that should be kept in mind whenever interpreting data. The model is one-dimensional. Centrifugal acceleration and fluid flow are assumed to be parallel to the axis of the core. The assumption that $S_w = 100\%$ at $r = r_e$ is necessary, and the theory is based on the "bundle of capillary tubes" model of the porous medium.

Experimental Results

Measurement of Water-Air Capillary Pressure

The cores used in this study were 1 in. in length, 1 in. in diameter and of 1000 md permeability. They were cut from a single block of Berea sandstone obtained courtesy of Stanford University, Petroleum Research Institute. To determine porosity, the cores were dried 12 hours at 85 °C, weighed, vacuumed at 10 microns of mercury for 5 hours, flooded with deaerated brine, and weighed again. The weight difference between saturated and dry cores determines porosity.

A Beckman Model L5-50P Rock Core Ultracentrifuge was used for the measurements. This instrument is equipped with a strobe light assembly in the rotor chamber and a viewing port in the chamber door. The strobe flashes once during each revolution of the rotor, so measurement of extracted volume can be made without stopping the centrifuge. The strobe can be adjusted to shine through a slit in any one of the rotor buckets. The extracted water collects in a tube or reservoir (see Figure 1).

The 100% water-saturated cores were loaded into a Type PIR-20 rotor. Approximately 1 mL of dense fluorocarbon oil (specific gravity 1.7 g/mL) had been placed in each collection tube to form a false bottom which facilitated readings. The run began at the lowest speed used, around 500 rpm. (The speed selected was very low because of the high permeability of these cores.) The rotation rate was held constant until the extracted volume stabilized. The speed was then changed to the next higher rotation rate. (It is essential to change each time to a higher rotation rate without ever lowering the rate. Redistribution of the fluids [hysteresis] would occur if the centrifuge were slowed or stopped. Thus, the subsequent values calculated for water saturation would be too low.)

Calculation of Capillary Pressure Curves

The raw data (see Table 1) were in the form of extracted volume readings, V, *vs.* rotation rates in rpm (see Figure 2). Each volume reading was converted to an average saturation $\bar{S}_w$, using the total pore volume of the core, V_{tot}:

$$\bar{S}_w = 1 - \frac{V}{V_{tot}} \tag{4}$$

The total pore volume for the Berea core No. 12 was 2.7 mL. Each rotation rate, rpm, was converted to a pressure, z, using

$$z = \frac{\Delta\rho\omega^2}{2}(r_e^2 - r_i^2) \tag{5}$$

For the case of air-water, $\Delta\rho = 1.0$ g/mL; thus, for a 1-in. long core run in the Type PIR-20 rotor (where $r_e = 8.6$ cm), $z = (2.96 \text{ psi})(\text{RPM}/1000)^2$.

The next step was to plot $z\bar{S}_w$ *vs.* z (see Figure 3). Using Equation 3, where $P_c = z$, the capillary pressure curve (Figure 4) is generated from the data of Figure 3. The slope of the $z\bar{S}_w$ *vs.* z curve (Figure 3) was taken graphically.

Table 1. Experimental Data for Berea Sandstone Core No. 12. The estimated accuracy of the volume readings is ± 0.02 mL. The extracted water volumes were obtained from the volume readings by subtracting the 0.92 mL of fluorocarbon oil used to form the lower meniscus.

Centrifuge Speed (rpm)	Volume Readings (mL)	Extracted Water Volumes (mL)	$\bar{S}_w$	z (psi)
437	1.10	0.18	0.93	0.565
537	1.08	0.16	0.94	0.854
653	1.23	0.31	0.88	1.262
765	1.52	0.60	0.78	1.732
860	1.74	0.82	0.70	2.189
970	1.91	0.99	0.63	2.785
1075	2.08	1.16	0.57	3.421
1175	2.20	1.28	0.53	4.087
1275	2.28	1.36	0.50	4.812
1380	2.34	1.42	0.47	5.637
1477	2.41	1.49	0.45	6.457
1575	2.48	1.56	0.42	7.343
1680	2.52	1.60	0.41	8.354
1865	2.60	1.68	0.38	10.296
2000	2.65	1.73	0.36	11.840

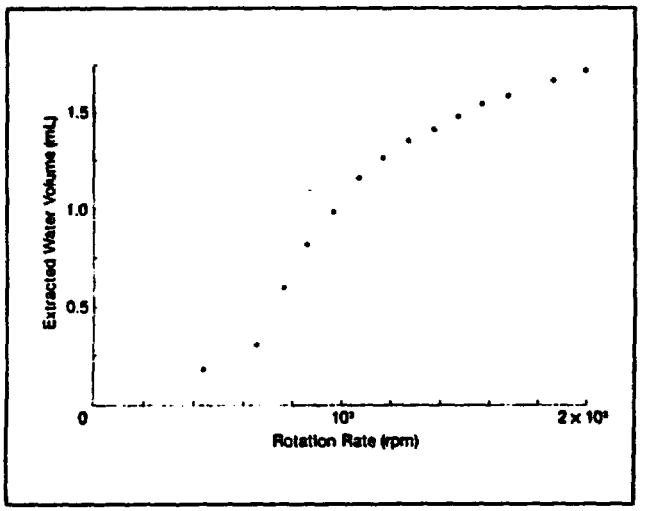

Figure 2. *Extracted Water Volume vs. Rotation Rate for Berea Core No. 12. The estimated accuracy of the volume readings is 0.02 mL.*

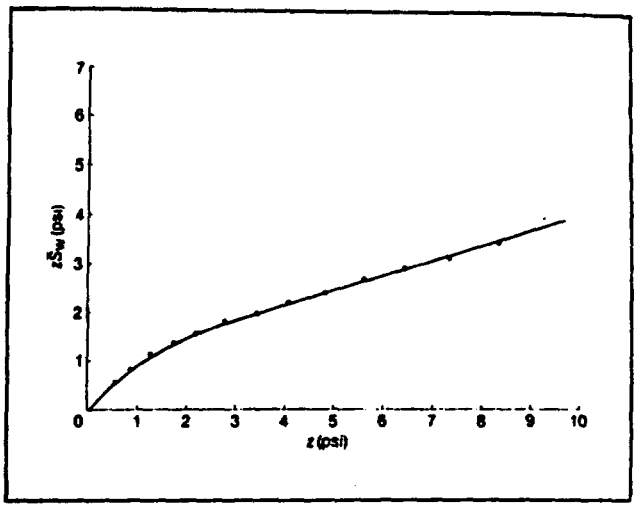

Figure 3. $z\,\bar{S}_w$ *vs.* z. *The data of Figure 2 was reduced through the procedure described under* Calculation of Capillary Pressure Curves.

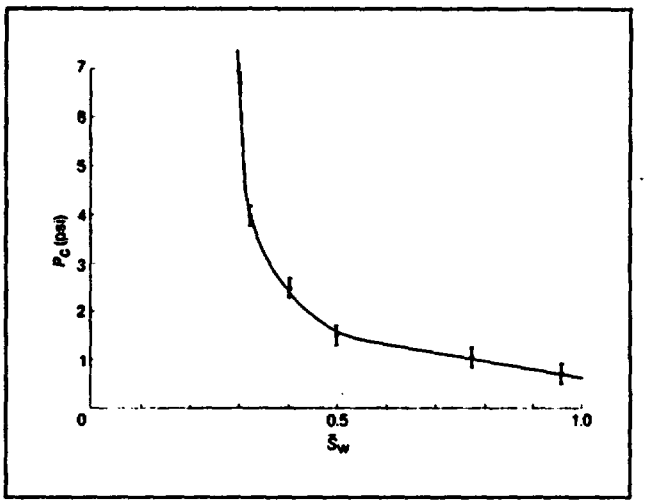

Figure 4. *Capillary Pressure Curve. This is the derivative of the line plotted in Figure 3. Note that the irreducible water saturation of 30% is attained at a very low capillary pressure. This correlates with the high permeability of the core.*

References

1. Hassler, G. L., Brunner, E. Measurement of capillary pressures in small core samples. *Trans. Am. Inst. Min. Metall. Eng. 160*, 114-123 (1945)
2. Slobod, R. L., Chambers, A., Prehn, W. L., Jr. Use of centrifuge for determining connate water, residual oil, and capillary pressure curves of small core samples. *Trans. Am. Inst. Min. Metall. Eng. 192*, 127-134 (1951)
3. Marx, J. W. Determining gravity drainage characteristics on the centrifuge. *Trans. Am. Inst. Min., Metall. Pet. Eng. 207*, 88-91 (1956)
4. Hoffman, R. N. A technique for the determination of capillary pressure curves using a constantly accelerated centrifuge. *Soc. Pet. Eng. J. 3*, 227-235 (1963)
5. Luffel, D. L. Further discussion of "A technique for the determination of capillary pressure curves using a constantly accelerated centrifuge," by R. N. Hoffman published in *Soc. Pet. Eng. J. 3*, 227-235 (1963). *Soc. Pet. Eng. J. 4*, 191-194 (1964)
6. Donaldson, E. C. Wettability determination and its effect on recovery efficiency. *Soc. Pet. Eng. J. 9*, 13-20 (1969)
7. Szabo, M. T. New methods for measuring the imbibition capillary pressure and electrical resistivity curves by centrifuge. *SPE Pap. 3038, Ann. Fall Tech. Conf. Soc. Pet. Eng. AIME, 45th, 1970.*
8. Samaroo, B. H., Guerrero, E. T. The effect of temperature on drainage capillary pressure in rocks using a modified centrifuge. *SPE Pap. 10153, Ann. Fall Tech. Conf. Soc. Pet. Eng. AIME, 56th*, 1981.
9. Hagoort, J. Oil recovery by gravity damage. *SPEJ, Soc. Pet. Eng. J. 20*, 139-150 (1980)
10. Van Spronsen, E. Three-phase relative permeability measurements using the centrifuge method. *SPE/DOE Pap. 10688, Jt. Symp. Enhanced Oil Recovery, 3rd*, 1982.
11. Dullien, F. A. L. *Porous Media; Fluid Transport and Pore Structure*. New York, Academic Press, 1979.

BECKMAN

Beckman Instruments, Inc.
Spinco Division
P.O. Box 10200
Palo Alto, California 94304
(415) 857-1150

4SP64780-283-5J

Printed in U.S.A.

Prof. A. Bolch
V-1-4 with compliments
26/V/1976

DETAILED INVESTIGATIONS OF GEOLOGICAL STRUCTURES BY SEISMIC WELL SURVEYS

Abstract

Seismic reflection observations in wells improve the results of detailed study of complicated geological structures. These are carried out to provide three-dimensional interpretation.

Observations below the weathering zone increase resolution and signal-to-noise ratio. The multi-component registration with special regard to wave polarisation allows one to realise the optimum space–time systems for processing.

As a result of observations in wells, signal spectrum is substantially broadened thus providing sure detection of the frequency change absorption caused by the presence of oil and gas deposits.

Examples of a study of complicated geological structures are presented: the cross-sections and the contour maps, anomalies of absorption over deposits.

Résumé

L'étude des réflexions sismiques dans les puits améliore sensiblement les résultats des études des structures géologiques compliquées. Les enregistrements sont réalisés de façon à permettre l'interprétation en trois dimensions.

Les mesures faites en-dessous de la zone altérée, augmentent le pouvoir de résolution et le rapport signal bruit. L'enregistrement à plusieurs composantes compte tenu de la polarisation des ondes, a permis de réaliser des systèmes spatio-temporels optimals pour le traitement.

Les mesures dans les puits ont permis d'étendre sensiblement le spectre de signaux, ce qui a garanti la détection sûre des changements de la composition de fréquences et de l'absorption provoqués par la présence de pétrole et de gaz.

A titre d'exemples d'études de structures géologiques compliquées, on présente des coupes sismiques, des cartes de structure, des anomalies d'absorption au-dessus des gisements.

by E. V. KARUS,
All-Union Research Institute of Nuclear Geophysics and Geochemistry, Moscow, U.S.S.R.
L. A. RYABINKIN,
Gubkin Moscow Institute of Petrochemical and Gas Industry, U.S.S.R.
E. I. GALPERIN,
Institute of Physics of the Earth, U.S.S.R. Academy of Science, U.S.S.R.,
V. A. TEPLITSKIY,
All-Union Research Institute of Petroleum Geology, U.S.S.R.,
Yu. B. DEMIDENKO,
Ukrneftegeofizika, Ministry of Geology of the Ukrainian S.S.R., U.S.S.R.,
K. A. MUSTAFAYEV,
Azerbaijan Branch of All-Union Research Institute of Geophysical Exploration, U.S.S.R.,
and M. B. RAPOPORT,
Gubkin Moscow Institute of Petrochemical and Gas Industry, U.S.S.R.

1. INTRODUCTION

The earliest surveys were made for the determination of average velocities and subsequent analysis in major exploration areas. Later, suggestions were made to use borehole surveys to locate geometrical positions of geological boundaries.[1-7] The industry began to use a seismic method of exploring configurations of concealed geological bodies of a complex shape by recording first arrivals of waves travelling between boreholes.[6] Further research resulted in development of a method of vertical seismic profiling (VSP).[2-4] The evolution of the method and the related references have been reported in a paper submitted to the 8th World Petroleum Congress.[1]

In the first place, the VSP method has made a great contribution to the studies of acoustic properties of geological media by seismoacoustic methods, which have long since been made in the USSR and which recently have become particularly successful.[8] The development of the acoustic log[7] has made it possible

8.3.1.2.2.3
Encl. 2

to survey uncased and cased boreholes with simultaneous recording of wave patterns, phase-correlation diagrams and interval time curves. This has greatly increased reliability of velocity determination under such complicated conditions as intensive absorption and high interference of the casing, and has allowed determination of shear velocities and effective attenuation.

Special research has been made, which proved the absence of geometrical and three-dimensional dispersion of velocities in a broad range of frequencies. This means that velocity data obtained from acoustic logs may be used in the work with seismic frequencies.

Thus, favourable conditions have been created for combined application of acoustic log and vertical seismic profiling providing a more accurate velocity section which is a very important requirement for detailed investigations of crustal geological structure by seismic methods.

The successful application of the VSP method has also initiated the appearance and development of several prospecting modifications designed for detailed exploration of complicated geological structures rather than for studies of acoustic characteristics of geological media. Recording of seismic waves in boreholes at a remote distance from the low-velocity zone and the ground surface has many significant advantages which will be discussed in detail in the sections that follow. These advantages served as the basis for a rapid development of several prospecting techniques which allow exploration of deep-seated complicated geological structures with high accuracy.

The most developed and most widely used in the USSR is a method of reverse reflection observations (RRO),[21] in which multichannel detector sondes are lowered into the available or specially drilled boreholes and seismic energy is generated near the ground surface with a preselected spacing along a line. The resulting time (or depth) sections are corrected in accordance with a modified shot-geophone arrangement as compared with a conventional one. All the known techniques of wave selection can be applied in processing.

Another modification is a method of offset vertical profiling (OVP),[19] in which a detector sonde is moved along the bore of a deep well and seismic energy is generated at different points offset from the well mouth. Large shot-to-detector distances permit CDP stacking using an algorithm different from the conventional one.[18] On field records obtained in boreholes by the RRO and OVP methods, waves of different types and classes vary in apparent velocities. Figure 1 shows an OVP record in which one can easily distinguish waves of different nature each having its own apparent velocity. This facilitates selection of the reflections characterising the structure of subsurface formations.

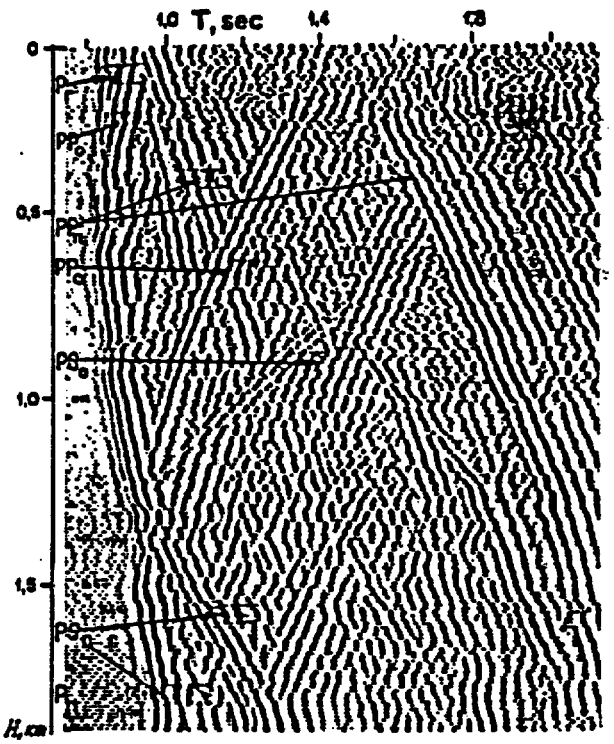

Fig. 1—A seismic record of offset vertical profiling (OVP). Seismic waves: P_r, head wave; PP_n, reflection; P_n, direct transmitted wave; PP_n, multiple reflection, transmitted; PS_o, exchange wave; PS_m, exchange transmitted wave (from the results of G. E. Rudenko).

In RRO and OVP data processing, seismic records are transformed into vertical time sections of the same type as those obtained from conventional reflection or CDP surveys. Processing of OVP records is accomplished using two types of waves: those reflected upwards, and those reflected and travelling downwards from a single boundary.[2] The resulting time section shows the positions of reflecting boundaries in the space near the borehole and facilitates identification and analysis of primary and multiple reflections. An example of such a section is shown in Fig. 2. The portion to the left of the vertical line $x = 0$ was plotted using the fronts of primary upward

reflections and that to the right using the extensions of the fronts of the same waves travelling downwards.

Transformation of OVP records into time sections helps to eliminate the effect of noise on correlation of line-ups when they are traced to form seismic horizons. It also substantially increases the area of the boundaries surveyed.

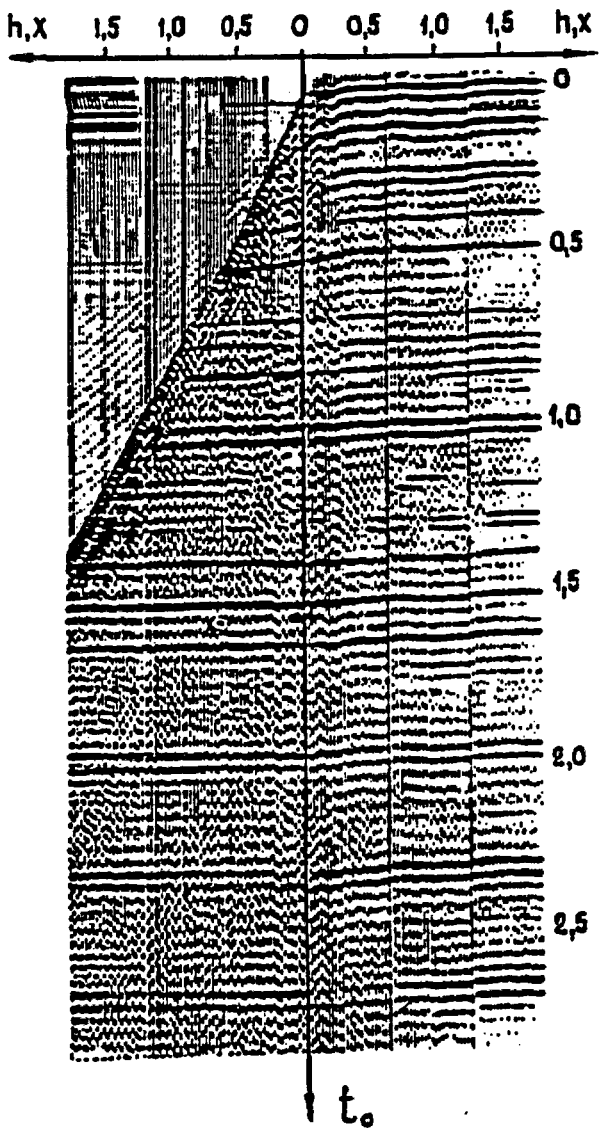

Fig. 2—Seismic section of offset vertical profiling (OVP) plotted from upward reflections (left) and multiple transmitted reflections (right).

2. BOREHOLE INVESTIGATIONS

If with a borehole depth of 3 km the area investigated by upward reflections is 3–4 km, the usage of extensions of the fronts of these waves reflected downwards enlarges it to 4·5–6 km^2.

Successful application of borehole modifications of a reflection method is greatly favoured by appropriate features found in the spectra of the recorded waves owing to the location of seismic detectors below the low-velocity zone which filters low frequencies.[22] One of the typical examples of numerous frequency analyses of the waves recorded in reverse reflection observations (RRO) is shown in Fig. 3.

Figure 3(a) shows a P-wave velocity curve alongside the geological column of the well in which the measurements were made. The data recorded in the well were used for calculating the spectra of one wave. The base of the low-velocity zone is at a depth of 20 m. Figure 3(b) shows the spectra calculated at depths of 6 and 42 m. Characteristic values of cut-off and maximum frequencies at a 0·7 level are marked by dots. One can easily see the difference of frequencies of the spectra maxima from 20 to 70 cm/sec. Figure 3(c) shows a relationship of the above-mentioned characteristic frequency values versus the depth of the well. Figure 3(d) shows a frequency response characteristic of a space between the points at which the frequency spectra were measured. One can see a substantial slope of high frequencies suppression.

Thus, seismic detectors lowered into a well and pressed to the walls of a hole record signals which have not yet lost the most informative high constituents of their spectra.

Another advantage of recording seismic waves in boreholes is the fact that the detectors appear to be completely protected against surface waves which are most intensive in conventional seismic prospecting.

However, borehole surveys possess some specific features, one of which is recording many waves of equivalent intensity which arrive at the detectors from various directions (Fig. 1). Differentiation and identification of these waves requires application of all available procedures of digital processing. Of great help here is multicomponent recording which can be easily performed in borehole surveys. It allows examination of wave polarisation which is carried out under more favourable conditions than at the surfaces.[5]

The greatest success in the analysis of polarisation of the waves recorded in the subsurface has been achieved in scanning complex combinations of various waves, in picking and following reflected

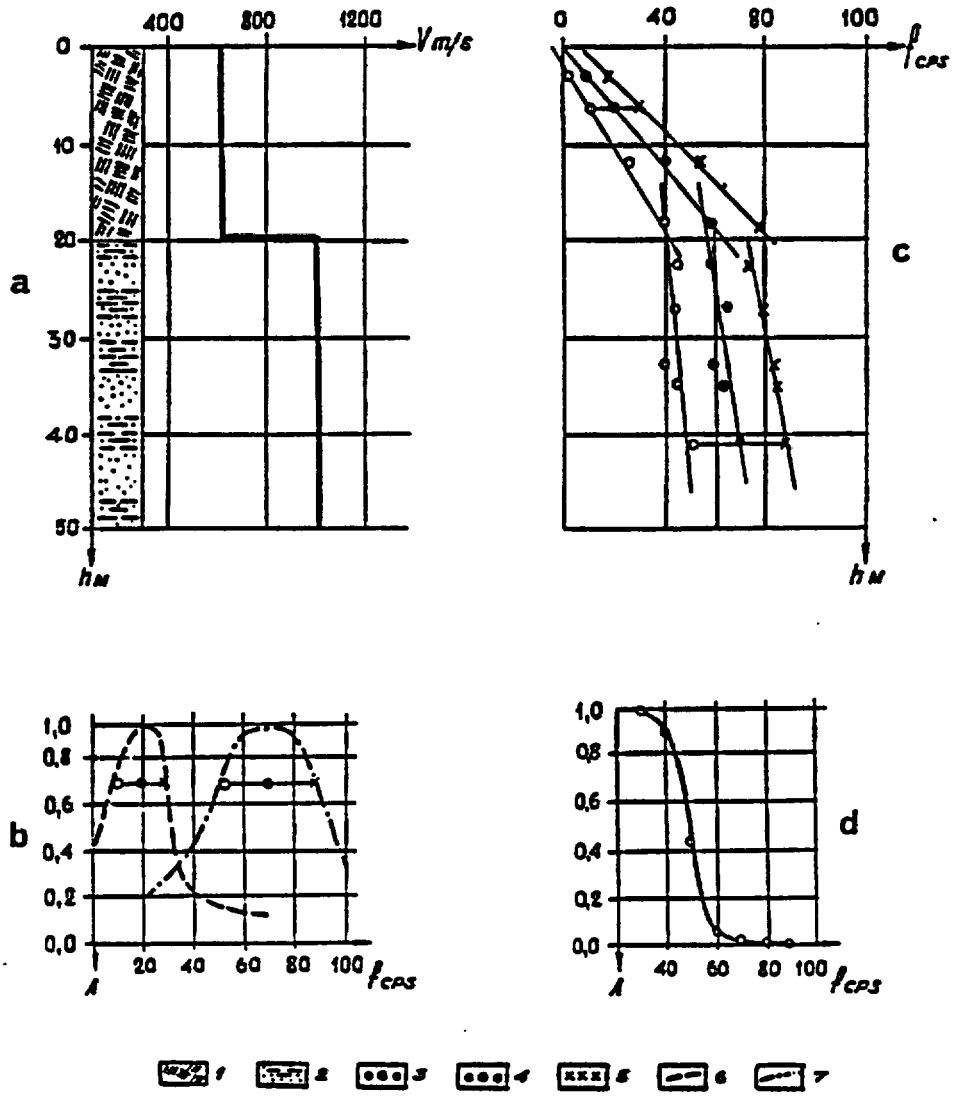

Fig. 3—Amplitude–frequency spectra of a direct wave recorded in a borehole: (a) lithological cross-section and layer velocities; (b) direct wave spectra at depths of 6 and 42 m; (c) curves of cut-off and maximum frequencies; (d) frequency response characteristic of the low-velocity layer: 1, loess; 2, loam; 3, low cut-off frequencies; 4, maximum frequencies; 5, high cut-off frequencies; 6, spectrum at a depth of 6 m; 7, spectrum at a depth of 42 m.

events and in mapping such subsurface structural features which cannot be detailed by conventional shooting from the surface (slopes of salt domes, diapirs, reefs, intrusions, fault zones and others).

In the case of a complex structure of subsurface formations the directions of wave incidence do not only deviate from the vertical but also greatly vary along the line of shooting. In this case, the commonly recorded vertical component which is not related to the direction of wave propagation loses its specific sense which it has in surface observations.

Accuracy of identification and resolution of compressional and exchange waves arriving from different directions are increased by using a polarisation positional correlation the main essence of which is as follows.[13]

At each recording point, three components of waves are repeatedly projected on to a series of directions with different azimuths and dips. Then for every point and every wave we select those projections which provide the best correlation. Figure 4 illustrates the possibilities of this approach. For comparison the figure shows two records, one obtained from vertical projections and the other from the projections selected with the above-mentioned optimum technique.

Along with a three-component set-up, use is also made of a uniform symmetrical array of inclined geophones, which has substantial advantages as compared with the conventional X, Y, Z set-ups.[4-13]

In multicomponent borehole surveys it is required to know the actual orientation of the set-up which is measured with the help of magnetic or gyroscopic sensors.

In the case of highly intensive noise, the latter is

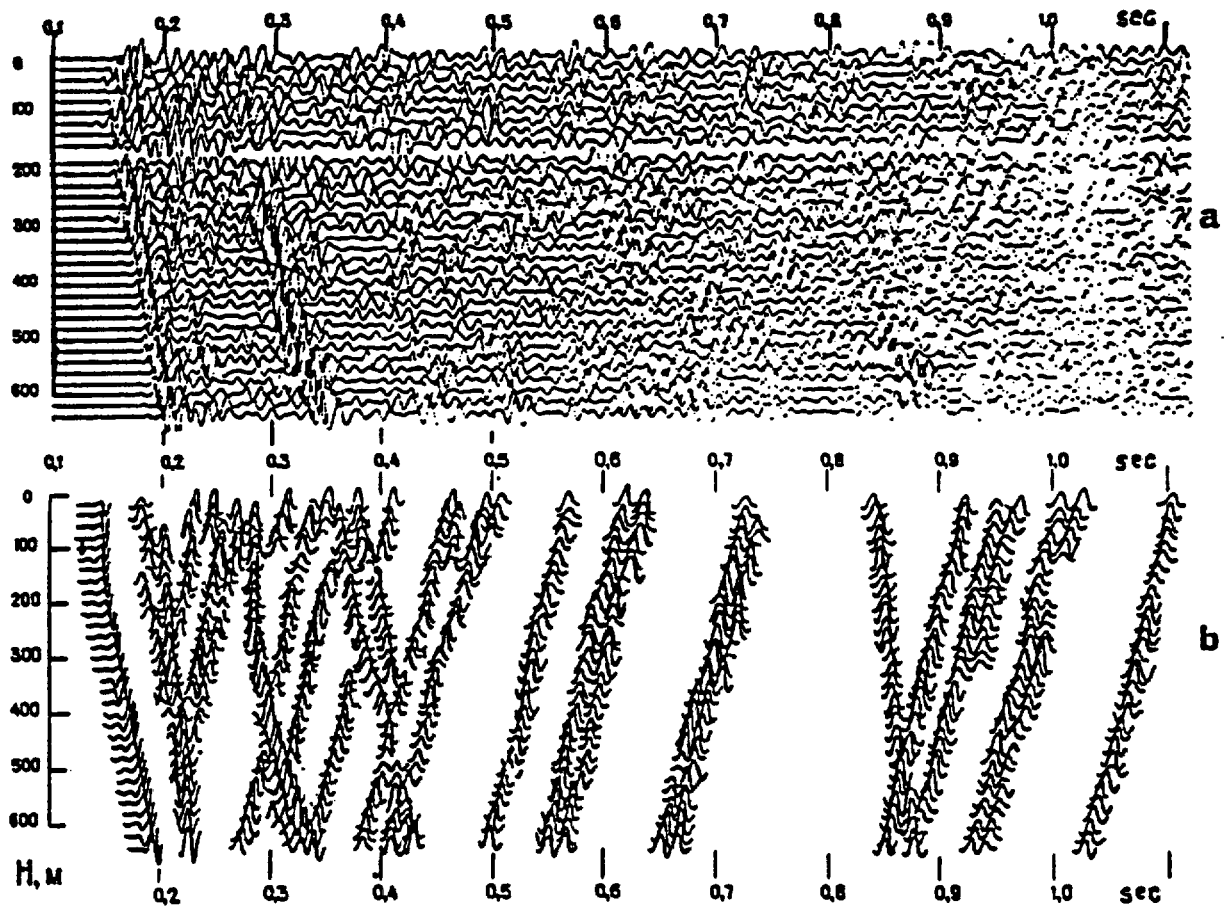

Fig. 4—An example of polarisation positional correlation of three-component borehole recording: (a) records from vertical projections; (b) records from optimally selected projections.

subtracted using a technique of energy analysis of the waves. A multi-step processing procedure of detecting seismic events recorded in the subsurface has recently been worked out.[9, 10]

The principal methodological characteristic of the procedure is a possibility of quantitative control of the effectiveness of every processing step and an ability to perform feedback operations.

3. ENERGY ANALYSIS

The basis of the multi-step procedure is an energy analysis of waves which is performed both at the initial and subsequent steps of processing.

The energy analysis consists of interpretation of estimates of a signal-to-noise ratio $\rho(t, V_i)$ which are obtained in a time window $(t - T, t + T)$, where t is a current time and $2T$ is an averaging interval for a preselected set of apparent or effective velocities (V_i). Regular waves are identified from the maximum values of $\rho(t, V_i)$.

The estimate of a signal-to-noise ratio is obtained as a ratio of estimates of a signal energy and a noise energy:

$$\rho(t, V_i) = \frac{\hat{E}_s(t, V_i)}{\hat{E}_n(t, V_i)} \tag{1}$$

where estimates of signal and noise energies are

$$\hat{E}_s(t, V_i) = \frac{1}{N(N-1)} \int_{t-T}^{t+T} \left\{ \left[\sum_{k=1}^{N} y_k(t + \tau_k(V_i)) \right]^2 - \sum_{k=1}^{N} y_k^2(t + \tau_k(V_i)) \right\} dt \tag{2}$$

$$\hat{E}_n(t, V_i) = \frac{1}{N(N-1)} \int_{t-T}^{t+T} \left\{ N \sum_{k=1}^{N} y_k^2(t + \tau_k(V_i)) - \left[\sum_{k=1}^{N} y_k(t + \tau_k(V_i)) \right]^2 \right\} dt \tag{3}$$

Here, $y_k(t)$ is a kth trace of a VSP record, whose model is

$$y_k(t) = \sum_{i=1}^{r} f_i(t - \tau_k(V_i)) + \xi_k(t) \tag{4}$$

where $f_i(t - \tau_k(V_i))$ is an ith regular wave with a velocity V_i, $\tau_k(V_i)$ is a delay of the ith regular wave at the kth trace, and $\xi_k(t)$ is a random noise.

It is shown that if a random noise wave $\xi_k(t)$ is normally distributed with zero mathematical expectation with a space–time correlation function of noise

$$R_{k,l}(t_1, t_2) = M\xi_k(t_1) \cdot \xi_l(t_2) \tag{5}$$

decreasing not slower than exponentially with increased $|k - l|$ or $|t_1 - t_2|$, then estimates $E_s(t, V_i)$ and $E_n(t, V_i)$ are consistent estimates of actual energies of a signal with a velocity V_i and of all the other signals.

In order to determine the signal-to-noise ratio of each wave, the estimate (4) is calculated for different values of velocity V_i. A set of functions obtained for a given set of velocities V_i or for a given set of traces $y_k(t)$ is here referred to as an energogram.

Regular noise is suppressed using a technique of multiple subtraction. Having subtracted the noise from a set of traces $y_k(t)$ we obtain a new set of traces $y_k^P(t)$ using a recurrent procedure:

$$y_k^{P+1}(t) = y_k^P(t) - \frac{1}{N} \sum_{k=1}^{N} y_k^P(t + \tau_k(V^P)), \qquad 1 \le P \le P - 1$$

Here, $\tau_k(V^P)$ is a delay of the arrival time of a Pth noise wave identified from the results of the energy analysis.

The effectiveness of suppressing the noise waves with velocities V_P is controlled by calculation of the estimate of a signal-to-noise ratio for traces $y_k^{P+1}(t)$ and comparison of the ratios obtained with those resulting from using initial traces $y_k(t)$.

Arrival times and move-outs of the waves recorded in boreholes allow effective application of two versions of the energy analysis.

In the first version, estimates of a signal-to-noise ratio are sequentially calculated for overlapping groups of traces and one velocity. In this case, having a set of functions $\rho_i(t, V)$, one can follow regular waves with a velocity V on a length of a vertical profile.

In the second version, the estimates of a signal-to-noise ratio, grouped into one energogram, are calculated for one group of waves and several different velocities V_i. Having such an energogram, one can separate several regular waves with different velocities V_i and evaluate for every wave a signal-to-noise ratio, a ratio of the energy of this particular wave to the total energy, and a share of the noise in the total energy.

An example of an energogram of the second type is shown in Fig. 5, which shows the result of processing of an OVP record obtained from a remote shot point. Such energograms resemble sum records of the CDR

subtracted using a technique of energy analysis of the waves. A multi-step processing procedure of detecting seismic events recorded in the subsurface has recently been worked out.[9, 10]

The principal methodological characteristic of the procedure is a possibility of quantitative control of the effectiveness of every processing step and an ability to perform feedback operations.

3. ENERGY ANALYSIS

The basis of the multi-step procedure is an energy analysis of waves which is performed both at the initial and subsequent steps of processing.

The energy analysis consists of interpretation of estimates of a signal-to-noise ratio $\rho(t, V_i)$ which are obtained in a time window $(t - T, t + T)$, where t is a current time and $2T$ is an averaging interval for a preselected set of apparent or effective velocities (V_i). Regular waves are identified from the maximum values of $\rho(t, V_i)$.

The estimate of a signal-to-noise ratio is obtained as a ratio of estimates of a signal energy and a noise energy:

$$\rho(t, V_i) = \frac{\hat{E}_s(t, V_i)}{\hat{E}_n(t, V_i)} \tag{1}$$

where estimates of signal and noise energies are

$$\hat{E}_s(t, V_i) = \frac{1}{N(N-1)} \int_{t-T}^{t+T} \left\{ \left[\sum_{k=1}^{N} y_k(t + \tau_k(V_i)) \right]^2 - \sum_{k=1}^{N} y_k^2(t + \tau_k(V_i)) \right\} dt \tag{2}$$

$$\hat{E}_n(t, V_i) = \frac{1}{N(N-1)} \int_{t-T}^{t+T} \left\{ N \sum_{k=1}^{N} y_k^2(t + \tau_k(V_i)) - \left[\sum_{k=1}^{N} y_k(t + \tau_k(V_i)) \right]^2 \right\} dt \tag{3}$$

Here, $y_k(t)$ is a kth trace of a VSP record, whose model is

$$y_k(t) = \sum_{i=1}^{r} f_i(t - \tau_k(V_i)) + \xi_k(t) \tag{4}$$

where $f_i(t - \tau_k(V_i))$ is an ith regular wave with a velocity V_i, $\tau_k(V_i)$ is a delay of the ith regular wave at the kth trace, and $\xi_k(t)$ is a random noise.

It is shown that if a random noise wave $\xi_k(t)$ is normally distributed with zero mathematical expectation with a space–time correlation function of noise

$$R_{k,l}(t_1, t_2) = M\xi_k(t_1) \cdot \xi_l(t_2) \tag{5}$$

decreasing not slower than exponentially with increased $|k - l|$ or $|t_1 - t_2|$, then estimates $E_s(t, V_i)$ and $E_n(t, V_i)$ are consistent estimates of actual energies of a signal with a velocity V_i and of all the other signals.

In order to determine the signal-to-noise ratio of each wave, the estimate (4) is calculated for different values of velocity V_i. A set of functions obtained for a given set of velocities V_i or for a given set of traces $y_k(t)$ is here referred to as an energogram.

Regular noise is suppressed using a technique of multiple subtraction. Having subtracted the noise from a set of traces $y_k(t)$ we obtain a new set of traces $y_k^P(t)$ using a recurrent procedure:

$$y_k^{P+1}(t) = y_k^P(t) - \frac{1}{N} \sum_{k=1}^{N} y_k^P(t + \tau_k(V^P)), \qquad 1 \le P \le P - 1$$

Here, $\tau_k(V^P)$ is a delay of the arrival time of a Pth noise wave identified from the results of the energy analysis.

The effectiveness of suppressing the noise waves with velocities V_P is controlled by calculation of the estimate of a signal-to-noise ratio for traces $y_k^{P+1}(t)$ and comparison of the ratios obtained with those resulting from using initial traces $y_k(t)$.

Arrival times and move-outs of the waves recorded in boreholes allow effective application of two versions of the energy analysis.

In the first version, estimates of a signal-to-noise ratio are sequentially calculated for overlapping groups of traces and one velocity. In this case, having a set of functions $\rho_i(t, V)$, one can follow regular waves with a velocity V on a length of a vertical profile.

In the second version, the estimates of a signal-to-noise ratio, grouped into one energogram, are calculated for one group of waves and several different velocities V_i. Having such an energogram, one can separate several regular waves with different velocities V_i and evaluate for every wave a signal-to-noise ratio, a ratio of the energy of this particular wave to the total energy, and a share of the noise in the total energy.

An example of an energogram of the second type is shown in Fig. 5, which shows the result of processing of an OVP record obtained from a remote shot point. Such energograms resemble sum records of the CDR

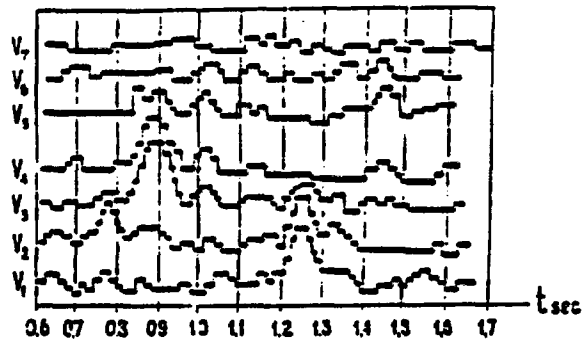

Fig. 5—A set of energograms calculated for different apparent velocities (the second version of the energy analysis of seismic waves recorded in a borehole).

technique (controlled directional reception). They help to separate overlapping waves with a high level of random noise. One can easily recognise the most intensive events at times of 0·88 and 1·25 sec (velocities V_4 and V_2) and less intensive at times of 0·77 and 1·44 sec (velocities V_2 and V_5). The events at 0·77 and 0·88 sec were resolved only because the procedure was repeated for different velocities V_i.

4. DIRECT INDICATIONS OF OIL AND GAS

The advantages of borehole surveys (primarily noise suppression and broader frequency spectrum) are also very contributory in solving lithological problems. One of them is a problem of direct oil and gas finding. Among the direct indications of oil and gas pools reported in a paper to the 7th World Petroleum Congress,[20] numerous observations have proved a relationship existing between oil and gas pools and zones of abnormally high absorption of seismic waves. It has also been discovered that at least in some cases not only pay formations produce this effect but also their aureoles detected by mud logging.

Figure 6 shows curves of amplitudes corrected for divergence of a direct wave recorded in a well (No. 982) drilled near the margins of a pool at different depths from two shot points, SP-1 and SP-2. The seismic rays from the second shot pass through the pool and non-productive hydrocarbon accumulation (aureole) above it. One can see a rapid decrease of amplitudes in the pool where their attenuation marked by a rate of the curve rise is one order higher. The rays from the first shot (at the left) do not penetrate through the pool, and direct waves slowly attenuate with depth.

Zones of high absorption can be distinguished by two independently determined effects, spectral and energetic. The former implies lowering of frequencies owing to the increase of attenuation with frequency, and the latter general attenuation of energy with time. The former, most widely used, allows arbitrary amplitude control during recording permitting the use of old records, and the latter requires specially controlled amplitude regulation.

In order to determine absorption parameters, a seismic record is divided into time intervals of a sufficiently large duration T (as compared with a duration of a pulse). With some assumptions and a linear absorption versus frequency relationship an absorption decrement g can be estimated from averaged power spectra for pairs of adjacent intervals i, $i+1$.[14, 15]

Power spectra are calculated with the help of either rapid Fourier transformation or autocorrelation functions $B_i(\tau)$ depending upon the technical means available. To avoid errors, it is essential that the spectra should be averaged for a large number of traces (a seismic record or several common depth points).

In correlation analysis the amount of calculation is much smaller if a bell-shaped cosine function with a visible frequency ω_0 is adopted as a model:

$$B_i(\tau) = \exp(-a^2 \cdot \tau^2) \cdot \cos(\omega_{0,i} \cdot \tau) \qquad (6)$$

For the next interval $(i+1)$, having considered the absorption, we obtain

$$B_{i+1}(\tau) = \exp(-a^2 \cdot \tau^2) \cdot \cos(\omega_{0,i+1}\tau)$$

The shape of an envelope as a low-frequency function did not change, and the visible frequency is

$$\omega_{0,i+1} = \omega_{0,i} - \frac{a^2(t_{i+1} - t_i) \cdot 2g}{\pi} \qquad (7)$$

where t_i are times of the centres of the intervals.

We see that the absorption decrement g is proportional to variation of visible frequencies (or visible periods) of an autocorrelation function. Therefore, the simplest parameter qualitatively characterising the absorption is a relative variation of visible periods

$$\beta = \frac{T_{0,i+1} - T_{0i}}{T_{0i}} \qquad (8)$$

where $T_{0i} = 2\pi/\omega_{0i}$ is a visible period of autocorrelation function of an interval i, which characterises the average period of seismic waves in this interval.

Owing to its simplicity, parameter β is widely used

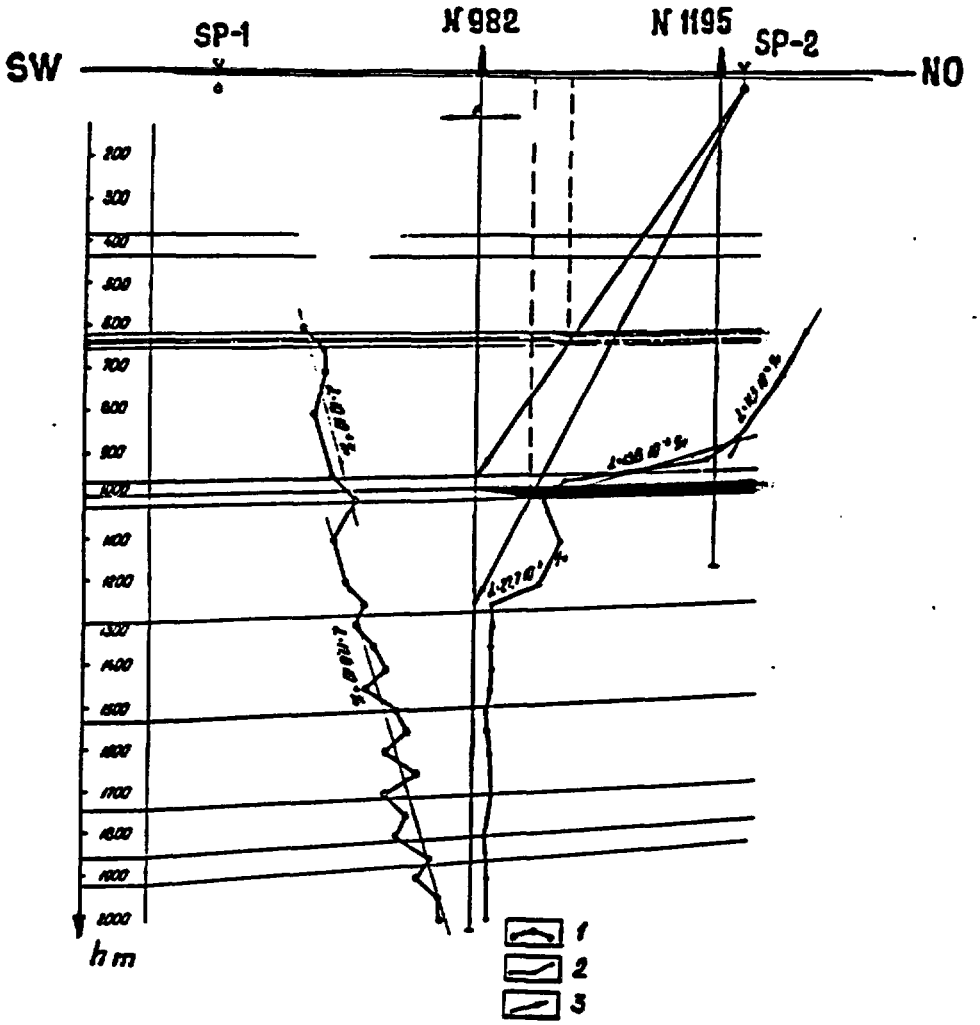

Fig. 6—Attenuation of a direct wave amplitude in a hydrocarbon pool: 1, amplitudes measured from SP-1; 2, same from SP-2; 3, averaged amplitude curves used for calculating attenuation.

in practice. Using a computer, a decrement estimate can be obtained without any significant additional effort using characteristic points of an autocorrelation function, for instance its first maximum. A magnitude of the maximum $B_i(T_{0i})$ is measured at this point ($\tau = T_{0i}$), and according to eqn. (6):

$$a^2 = \frac{1}{T_{0i}^2} \ln \frac{B_i(0)}{B_i(T_{0i})} \tag{9}$$

Using eqn. (7), we obtain an absorption decrement g:

$$g = \frac{\pi^2}{2} \cdot \frac{T_{0,i+1} - T_{0i}}{t_{i+1} - t_i} \cdot \frac{T_{0i}}{T_{0,i+1}} \cdot \ln \frac{B_i(T_{0i})}{B_i(0)} \tag{10}$$

Having obtained the first maxima of autocorrelation functions $B_i(T_{0i})$ for intervals with the centres t_i and t_{i+1}, we can estimate a decrement value from the measurements for each pair of intervals.

The same data are used to determine attenuation:

$$\xi = \frac{T_{0i}}{t_{i+1} - t_i} \ln \frac{B_i(0)}{B_{i+1}(0)} \tag{11}$$

Attenuation can be determined without correlation analysis, from time variation of amplitudes.

The above-mentioned assumptions of the subsurface layering and stationarity of waves within every interval become unnecessary if acoustic logs are

available for the considered depth intervals.[16] In that case the effect of noise in the layered earth can be taken into account using synthetic records. This increases the accuracy of absorption estimation and makes it possible to analyse small time intervals, which increases the resolution.

5. CONCLUSIONS

Borehole seismic surveys are capable of delineating the outlines of hydrocarbon pools by placing geophones at the surface and making explosions beneath the pools or the other way round.[11, 12] Zones of high absorption produced by the pools are recognised from decreased amplitudes and frequencies of direct waves. The displacement of a seismic shadow by changing depths of shot points (or reception points) allows estimation of the depths of pools.

If applied in producing wells, a seismic survey can locate internal and external boundaries of every productive formation in a multizone reservoir. In non-productive (dry) wells a survey can detect a pool near the well and outline its boundaries.

Borehole modifications of a seismic reflection method are widely used for detailing structures in wildcat and exploratory drilling.[22] An important application of OVP and RRO surveys is mapping reflection interfaces in the vicinity of wildcat and exploratory wells, particularly in deep horizons not yet explored by drilling.

The RRO surveys are generally made along a line of wells. They are designed to explore the boundaries in the lower sedimentary layers hidden beneath thick salt-bearing or carbonate formations. Applications of an RRO method were highly successful in mapping reefs situated beneath salt formations in the south of the USSR. Reflections were recorded at relatively small depths (400–500 m) below the upper marker. The surveys were made both in the available wildcat

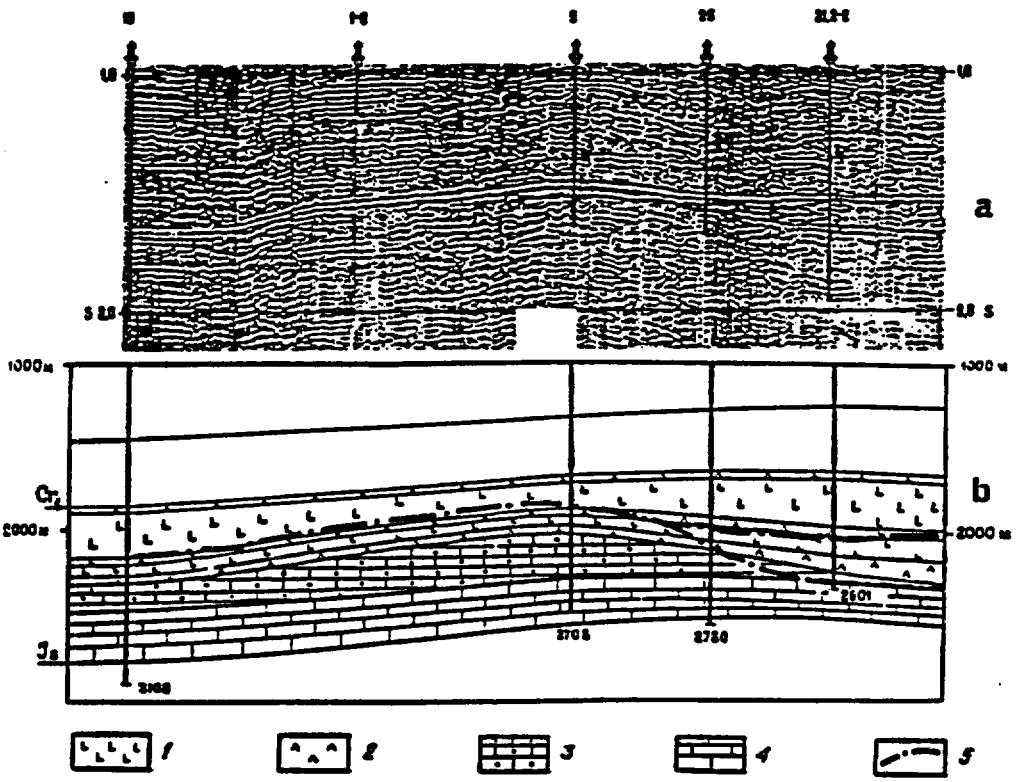

Fig. 7—Mapping of a reef beneath salt formations by reverse reflection observations (RRO): (a) RRO seismic section; (b) geological section; 1, salt; 2, anhydrite; 3, porous reef limestone; 4, impermeable limestone; 5, seismic boundaries from RRO recording.

wells and in specially drilled ones along extensive lines. A high resolution of the method resulted in reliable identification of reflections from the boundary between porous reef limestone and compact enclosing rocks. Figure 7 shows an example of locating a reef by seismic data and a comparison with an actual geological section from drilling data. The comparison shows a high accuracy of the RRO method.

The RRO surveys were made in wells along a line of 7·5 km running across the strike of a structure. Two deep wells were available and three structural wells were purposely drilled. The distance between the wells was 1200–1500 m. The shot points were spaced 100 m apart. A multi-geophone sonde was lowered to a depth of 350–400 m below the base of the upper strong limestone marker. The RRO cross-section clearly shows a boundary of a salt formation wedged into a space between the reefs.

Figure 8(b) shows another example of locating a reef beneath a salt formation in which a gas deposit is found at a wing of a larger anticline. In this case the measurements were made in specially drilled shallow wells (not deeper than 300 m). The detectors were lowered below the first marker boundary. The reef was found to be situated between two closely spaced reflection interfaces. The slopes of the reef body are well defined due to a contact of the enclosing salt-anhydrite formations and porous limestone.

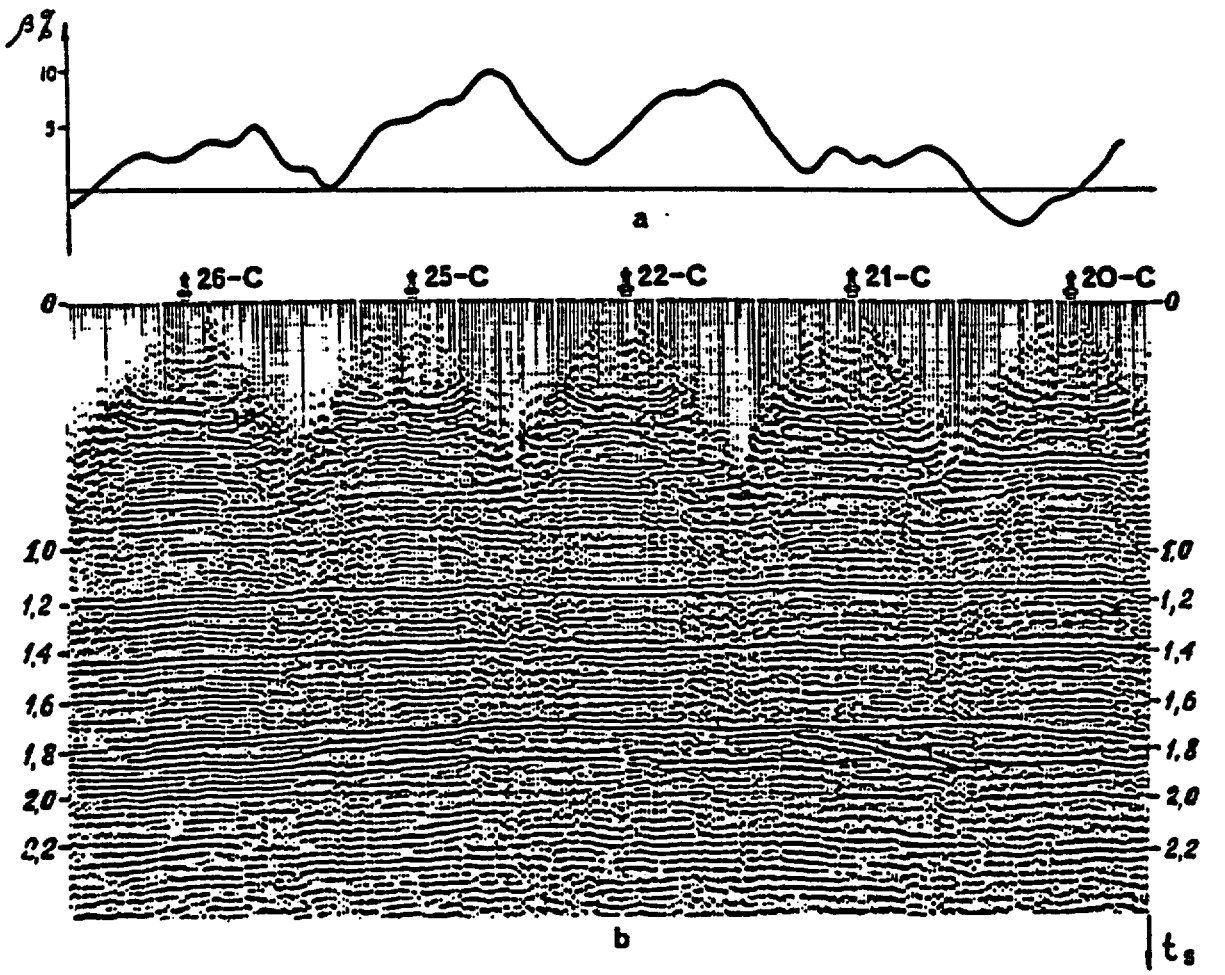

Fig. 8—Mapping of a reef beneath salt formations and evaluation of its oil and gas content: (a) absorption anomaly along a profile; (b) RRO seismic section.

Figure 8(a) shows an example of the application of the above-mentioned correlation technique of direct oil finding. The figure shows a curve resulting from processing the RRO data (Fig. 8(b)) obtained along a profile crossing a known gas deposit as was mentioned above. Two intervals of the analysis 0·5 sec each were chosen so that one of them (1·2 + 1·7 sec) was directly above the reef and the other (1·7 + 2·2 sec) included the top of the reef. A distinct absorption anomaly has been obtained consisting of two maxima reaching $\beta \approx 10\%$. The anomaly agrees with the position of the reef. The maximum values correspond to the ends of the reef. This effect is also often encountered in hydrocarbon deposits situated in terrigenous rocks. The absorption anomaly is not very large and therefore could not be detected from surface shooting. It was located only by processing the data recorded in a borehole.

The examples reported here, though small in number, clearly demonstrate the effect of seismic information recorded in boreholes for mapping reefs beneath salt formations. They reduce the amount of drilling and save time required for estimation of deposits. As to the application and improvement of seismic well surveys, their future success and perspectives can be predicted with certainty bearing in mind the above-mentioned advantages of seismic recording in the subsurface.

References

1. A. C. BORISEVICH, L. A. RIABINKIN and N. T. TURCHANENKO, Investigation of deep complicated structures by seismic methods, Paper to 8th Wld. Petrol. Congr., 1971.
2. Yu. B. DEMIDENKO, Geofizicheskii sbornik IGANUSSR, 1964, 7(9), Kiev, Naukova Dumka.
3. Yu. B. DEMIDENKO, in: Metodika seismicheskikh issledovanii, Kiev, 1967, Tekhnika.
4. E. I. GALPERIN, Vertical seismic profiling, Moscow, 1971, Nedra.
5. E. I. GALPERIN, G. I. AKSENOVICH and A. V. FROLOVA, in: VSP—uvelichenie effektivnosti seismicheskikh issledovanii, Moscow, 1971, VIEMS.
6. S. I. IVANOV, Trudy NIIGA, 1953, 39, Gosgeotekhizdat.
7. E. V. KARUS, O. L. KUZNETSOV and B. N. IVAKIN, Trudy VII Vsesoyuznoi i-t geofiz. konferentsii, Moscow, 1974, Nedra.
8. E. V. KARUS and O. L. KUZNETSOV, Izvestiya AN SSSR, ser. Fizika Zemli, 1974, no. 11.
9. S. A. KATS, T. N. ERSHOVA and B. M. SHUBIK, ONTI VIEMS, ser. Regionalnaya, razvedochnaya i promyslovaya geofizika, Moscow, 1973.
10. S. A. KATS, T. N. ERSHOVA and B. M. SHUBIK, Prikladnaya geofizika, 1973 (72), Moscow, Nedra.
11. K. A. MUSTAFAYEV, in: Neftegazovaya geologiya i geofizika, 1973, no. 12, Moscow, VNIIOENG.
12. K. A. MUSTAFAYEV, Avt. Svidet. SSSR No. 338474, 1972.
13. E. I. GALPERIN (ed.), Polarization of seismic waves applied to increase the effectiveness of seismic prospecting (Polarizatsiya seismicheskikh voln i vozmozhnosti uvelicheniya effektivnosti seismicheskikh issledovanii), Trudy KazVIRG, 1974, No. 7.
14. M. B. RAPOPORT and A. E. SAKHAROV, in: Tsifrovaya obrabotka dannykh seismorazvedki, ONTI VIEMS, Moscow, 1970.
15. M. B. RAPOPORT, Automatic data processing in seismic prospecting (Avtomaticheskaya obrabotka zapisei kolebanii v seismorazvedke), Moscow, 1973, Nedra.
16. L. I. RAPOPORT, in: Voprosy geologii, geokhimii i geofiziki pri poiskakh poleznykh iskopaemykh i ingenerno-geologicheskikh izyskaniyakh, 1974, Izd. MGU.
17. Yu. V. RIZNICHENKO, Trudy in-ta teoret. geofiz., 1946, 2, Izd. AN SSSR.
18. G. E. RUDENKO, in: Razvitie metodiki skvazhinnykh seismoakusticheskikh nabliudenii, ONTI VIEMS, Moscow, 1971.
19. G. E. RUDENKO and L. L. KHUDZINSKIY, Razvedochnaya geofizika, 1972, No. 50, Moscow, Nedra.
20. L. A. SERGEYEV, H. A. ALIZADE, A. A. GEODEKIAN *et al.*, On possibility of direct oil finding, Paper to 7th Wld. Petrol. Congr., Mexico, 1967.
21. V. A. TEPLITSKIY, in: Novye tekhnicheskiei metodicheskie razrabotkiv seismorazvedke, ONTI VIEMS, Moscow, 1963.
22. V. A. TEPLITSKIY, Trudy VNIGNI, 1973, 132, Moscow, Nedra.
23. V. S. VOYUTSKIY, Bul. neft. geofiz., 1937, 4, ONTI.

Figure 8(a) shows an example of the application of the above-mentioned correlation technique of direct oil finding. The figure shows a curve resulting from processing the RRO data (Fig. 8(b)) obtained along a profile crossing a known gas deposit as was mentioned above. Two intervals of the analysis 0·5 sec each were chosen so that one of them (1·2 + 1·7 sec) was directly above the reef and the other (1·7 + 2·2 sec) included the top of the reef. A distinct absorption anomaly has been obtained consisting of two maxima reaching $\beta \approx 10\%$. The anomaly agrees with the position of the reef. The maximum values correspond to the ends of the reef. This effect is also often encountered in hydrocarbon deposits situated in terrigenous rocks. The absorption anomaly is not very large and therefore could not be detected from surface shooting. It was located only by processing the data recorded in a borehole.

The examples reported here, though small in number, clearly demonstrate the effect of seismic information recorded in boreholes for mapping reefs beneath salt formations. They reduce the amount of drilling and save time required for estimation of deposits. As to the application and improvement of seismic well surveys, their future success and perspectives can be predicted with certainty bearing in mind the above-mentioned advantages of seismic recording in the subsurface.

References

1. A. C. BORISEVICH, L. A. RIABINKIN and N. T. TURCHANENKO, Investigation of deep complicated structures by seismic methods, Paper to 8th Wld. Petrol. Congr., 1971.
2. Yu. B. DEMIDENKO, Geofizicheskii sbornik IGANUSSR, 1964, 7(9), Kiev, Naukova Dumka.
3. Yu. B. DEMIDENKO, in: Metodika seismicheskikh issledovanii, Kiev, 1967, Tekhnika.
4. E. I. GALPERIN, Vertical seismic profiling, Moscow, 1971, Nedra.
5. E. I. GALPERIN, G. I. AKSENOVICH and A. V. FROLOVA, in: VSP—uvelichenie effektivnosti seismicheskikh issledovanii, Moscow, 1971, VIEMS.
6. S. I. IVANOV, Trudy NIIGA, 1953, 39, Gosgeotekhizdat.
7. E. V. KARUS, O. L. KUZNETSOV and B. N. IVAKIN, Trudy VII Vsesoyuznoi i-t geofiz. konferentsii, Moscow, 1974, Nedra.
8. E. V. KARUS and O. L. KUZNETSOV, Izvestiya AN SSSR, ser. Fizika Zemli, 1974, no. 11.
9. S. A. KATS, T. N. ERSHOVA and B. M. SHUBIK, ONTI VIEMS, ser. Regionalnaya, razvedochnaya i promyslovaya geofizika, Moscow, 1973.
10. S. A. KATS, T. N. ERSHOVA and B. M. SHUBIK, Prikladnaya geofizika, 1973 (72), Moscow, Nedra.
11. K. A. MUSTAFAYEV, in: Neftegazovaya geologiya i geofizika, 1973, no. 12, Moscow, VNIIOENG.
12. K. A. MUSTAFAYEV, Avt. Svidet. SSSR No. 338474, 1972.
13. E. I. GALPERIN (ed.), Polarization of seismic waves applied to increase the effectiveness of seismic prospecting (Polarizatsiya seismicheskikh voln i vozmozhnosti uvelicheniya effektivnosti seismicheskikh issledovanii), Trudy KazVIRG, 1974, No. 7.
14. M. B. RAPOPORT and A. E. SAKHAROV, in: Tsifrovaya obrabotka dannykh seismorazvedki, ONTI VIEMS, Moscow, 1970.
15. M. B. RAPOPORT, Automatic data processing in seismic prospecting (Avtomaticheskaya obrabotka zapisei kolebanii v seismorazvedke), Moscow, 1973, Nedra.
16. L. I. RAPOPORT, in: Voprosy geologii, geokhimii i geofiziki pri poiskakh poleznykh iskopaemykh i inzhenerno-geologicheskikh izyskaniyakh, 1974, Izd. MGU.
17. Yu. V. RIZNICHENKO, Trudy in-ta teoret. geofiz., 1946, 2, Izd. AN SSSR.
18. G. E. RUDENKO, in: Razvitie metodiki skvazhinnykh seismoakusticheskikh nabliudenii, ONTI VIEMS, Moscow, 1971.
19. G. E. RUDENKO and L. L. KHUDZINSKIY, Razvedochnaya geofizika, 1972, No. 50, Moscow, Nedra.
20. L. A. SERGEYEV, H. A. ALIZADE, A. A. GEODEKIAN *et al.*, On possibility of direct oil finding, Paper to 7th Wld. Petrol. Congr., Mexico, 1967.
21. V. A. TEPLITSKIY, in: Novye tekhnicheskiei metodicheskie razrabotkiv seismorazvedke, ONTI VIEMS, Moscow, 1963.
22. V. A. TEPLITSKIY, Trudy VNIGNI, 1973, 132, Moscow, Nedra.
23. V. S. VOYUTSKIY, Bul. neft. geofiz., 1937, 4, ONTI.

3995

SNOW
Not In Trade

Reprint from Vol. IV/4, 1988
FELSMECHANIK UND INGENIEURGEOLOGIE
ROCK MECHANICS AND ENGINEERING GEOLOGY
Springer-Verlag/Wien · New York

David T. Snow:

Three-Hole Pressure Test for Anisotropic Foundation Permeability

8.3.1.2.2.3
Encl. 2

Three-Hole Pressure Test for Anisotropic Foundation Permeability

By

David T. Snow*

With 4 Figures

Summary — Zusammenfassung — Résumé

Three-Hole Pressure Test for Anisotropic Foundation Permeability. Solutions to fluid-discharge or pore-pressure distribution problems in pervious foundations need not assume isotropic permeability if anisotropy is measured in the field. To devise a pumping test arrangement that will measure anisotropy, a procedure for computing the steady discharge from, or seepage to cylindrical cavities is derived. The cylinder analyzed may be arbitrarily oriented with respect to the principal permeability directions of an infinite, saturated, anisotropic rock mass. Independent water-pressure tests in three orthogonal drill holes, oriented along predetermined principal axes, will theoretically measure the three principal permeabilities, since discharge depends nearly upon the geometric mean of permeabilities normal to each test hole. An equation for the errors permits closure on the correct values.

Conventional exploration-hole lay-outs can often be modified to give pressure test data that can be analyzed for anisotropy, applicable especially where seepage, uplift or remedial drains or curtains are to be designed.

Abpreßversuche in drei Bohrlöchern zur Bestimmung der Durchlässigkeitsanisotropie im Baugrund. Bei der Beantwortung von Fragen über Strömungsvorgänge und Porenwasserdrücke in einem wasserdurchlässigen Baugrund darf dieser hinsichtlich seiner Wasserdurchlässigkeit keineswegs als isotrop angenommen werden, falls schon bei der Geländeaufnahme eine Anisotropie festgestellt wurde. Um die Anisotropie mittels eines Pumpversuches ermitteln zu können, wird ein Verfahren zur Berechnung eines gleichmäßigen Durchströmens oder eines Durchsickerns zu zylindrischen Hohlräumen hin entwickelt. Ein Zylinderhohlraum kann bezüglich der Hauptdurchlässigkeitsrichtungen in einer unbegrenzten, wassergesättigten und anisotropen Gesteinsmasse beliebig orientiert werden. Theoretisch kann aus unabhängig voneinander vorgenommenen Wasserdruckuntersuchungen in drei normal zueinander stehenden Bohrlöchern, die nach den zuvor bestimmten Hauptachsen ausgerichtet sind, die Größe der drei Hauptdurchlässigkeiten bestimmt werden, da das Ausfließen in etwa vom geometrischen Mittel der Wasserdurchlässigkeiten normal zur jeweiligen Bohrlochachse abhängig ist. Eine Korrekturgleichung erlaubt die Annäherung an die richtigen Werte.

Die herkömmlichen Anordnungen von Aufschlußbohrungen sollten öfters abgeändert werden, um Daten über die Durchlässigkeitswerte zu erhalten und damit eine Bestimmung der Anisotropie zu ermöglichen; besonders geeignet ist diese Methode, wenn Sickerungen und Auftrieb bestimmt und behelfsmäßige Drainagen und Injektionsschirme entworfen werden sollen.

Essai de compression à la presse dans trois trous de forage pour déterminer l'anisotropie de perméabilité au sous-sol. Pour résoudre les problèmes d'écoulement ou de distribution de pression dans les fondations perméables il n'est pas nécessaire de supposer que l'on a une perméabilité isotrope si l'anisotropie est mesurée sur place. Le système de

* David T. Snow, Assistant Professor of Geology, Colorado School of Mines, Golden, Colorado, USA.

pompage à utiliser pour mesurer l'anisotropie est déterminé à l'aide d'un procédure de calcul basé sur un écoulement uniforme dans des cavités cylindriques. Le cylindre analysé peut être orienté arbitrairement par rapport aux directions principales de perméabilité d'une masse rocheuse illimitée, saturée et anisotrope. Des mesures indépendantes de la pression d'eau dans trois trous de forage à angle droit, orientés suivant des axes principaux choisis d'avance, déterminent théoriquement les trois perméabilités principales, car l'écoulement est presque fonction de la moyenne géométrique des perméabilités normales à chacun des trous de mesure. Les écarts des valeurs vraies dûes aux erreurs sont corrigées à l'aide d'une équation.

Des forages conventionnels d'exploration peuvent être modifiés de façon à fournir des données de pression, lesquelles peuvent être analysées en fonction de l'anisotropie; ceci s'applique spécialement dans le cas de fuites, de soulèvements, ou dans le cas de construction de drains ou d'écrans d'étanchéité.

Introduction

A method of pressure-testing jointed rock to determine its anisotropic permeability is the object of this paper. Current practices of analyzing tests neglect nisotropy and heterogeneity. Solutions to boundary-value problems, to determine flow or pressure distribution in jointed rock, have thus-far been attempted by methods designed for isotropic, intergranular-conducting media. Notable examples include Stuart's (1955) drawdown tests for predicting shaft drainage, Thayer's (1962) analysis of Oroville pump-test data and Yokota's (1963) study of potential in the Kurobe IV dam-site. No rational basis of justifying the assumed isotropy has been advanced, though adequate correspondence between measured and theoretical potential values is sometimes found.

More commonly we observe anomalous uplift pressures beneath masonry dams (Richardson's 1948 report on Hoover Dam, for instance, p. 16), wildly erratic pressure-test discharges (Lyon's 1962 report of Oroville tests) or sporadic tunnel infiltration (Wahlstrom and Hornback's 1962 report on the Harold D. Roberts Tunnel, Colorado). These are expressions of the heterogeneity characteristic of jointed rock. As opposed to the systematic depth-varying inhomogeneity demonstrated by Turk (1963) and applied to water-well design by Davis and Turk (1964), heterogeneous permeability encountered in jointed rock is believed due to the process of sampling a few elements out of a large population having great dispersion of conductivity. It is better to attempt statistical interpretation of jointed-rock permeability values than it is to accept the pessimism of Terzaghi (1962), who said:

"Water levels in observation wells located in jointed rock can vary over short distances by important amounts and the effect that filling the reservoir will have on the pore water pressures in the gouge seams cannot even be estimated in advance ... the pattern of seepage is likely to be erratic ... one cannot tell which ones (joints) are continuous over a large area."

This paper is part of a broader work (Snow, 1965) modeling arbitrary joint sets with their orientations, apertures and spacings as statistical parameters, and leading to statistical evaluations of permeability. The mathematical model succeeds in reproducing the distribution of discharge obtained by field tests in crystalline rock.

With a theory to back it, refinement in methods of interpreting pump-tests is possible, but the data must be collected to reflect interpretable parameters of the medium. The model study predicts three different principal permeabilities and the orientations of principal axes, depending on the geometry of the system. For present purposes, it suffices to note the finding that an orthogonal joint system should have principal axes parallel to directions of joint intersections, with permeability magnitudes related to the spacial frequency of intersections.

Few field studies have demonstrated anisotropy for jointed rock, due to lack of methods to measure it. Interactions between wells indicated a preferred direction (in plan only) of permeability of the Spraberry oilfield (Elkins and Skov, 1960). Sweep efficiency has been proposed as a means of determining anisotropy (Landrum and Crawford, 1960). Contours on a piezometric surface for water conducted in fractures of the crystalline basement at the Nevada Test Site indicate high permeability in the direction of streamline convergence (Davis, 1963).

Improved resolution of anisotropy should prove it a general attribute of fractured rocks, by reason of their oriented planar conductors. Diamond-drill explorations can be designed to give measures of principal permeabilities that can then be treated statistically to establish medians, means and dispersions of the three heterogeneous measures required. Orientation of the drill-holes must nearly coincide with principal permeability axes, predetermined from study of joint orientation. Another publication treats directional effects more fully than is possible here (Snow, 1967).

To describe the orientation of three mutually orthogonal axes requires three independent parameters, and to describe the corresponding permeabilities, three additional. Since as many measures as unknowns are required for a unique solution, observable orientation data is relied upon for axial predictions, while three orthogonal drill-holes are employed to measure the principal permeabilities. Three suborthogonal pressure test holes can define the principal permeabilities because a discharge from each long cylindrical cavity depends largely upon the permeabilities in directions normal to the axis of the cavity, and but weakly upon the permeability parallel to the axis.

Theoretical Development

Theory developed by Maasland (1957, pp. 218–284) for piezometer tests in anisotropic soil is amplified and generalized for arbitrary orientations of packer test-holes in anisotropic media. Introductory theory is summarized from his work.

The three components of macroscopic velocity in an anisotropic medium may be expressed by Darcy's law:

$$v_i = -k_{ij} \frac{\partial \varphi}{\partial x_j},$$

where the repeated index signifies summation. If the tensor is oriented along principal axes, then k_{ii} are the principal hydraulic conductivities, cm/sec,

φ is the head, cm, and
x_j are the coordinates.

When substituted into the continuity equation,

$$\frac{\partial v_i}{\partial x_i} = 0,$$

there results

$$k_{ii} \frac{\partial^2 \varphi}{\partial x_i^2} = 0.$$

Maasland introduces an arbitrary constant, k_0, into the equations transforming the Cartesian coordinates to a system identified by primes:

$$x_i' = (k_0/k_{ii})^{1/2} x_i \text{ (after Samsioe, 1931).} \qquad (1)$$

This substitution results in the Laplace equation

$$\nabla^2 \varphi = 0.$$

When boundaries are expanded or contracted by equation (1), then potential theory for isotropic media applies. (Reviews of boundary problem methods are found in such texts as Collins, 1961, or Scheidegger, 1960.) The hydraulic conductivity of this equivalent but fictitious transformed medium,

$$k = (k_{11}\, k_{22}\, k_{33}/k_0)^{1/3}, \tag{2}$$

was derived by Vreedenburg (1936) and modified to the above form by Maasland.

Kirkham (1945) gives a general equation for flow from cavities below the water table:

$$Q = k S y, \tag{3}$$

where Q is the flow rate, say in gallons per day,

k is the hydraulic conductivity, feet per day,

y is the net hydraulic head, feet, and

S is a coefficient dependent upon the geometry of the cavity, the boundaries and unit conversions. Fig. 1 (b) identifies the assumed boundaries.

Maasland gives derivations and electric analogue results leading to S values for various shapes. Dachler (1936) called this coefficient the "Formfaktor"; Hvorslev (1951), the "shape factor"; and Zangar (1953) calls $S/2$ the "effective hemispherical radius". S is a constant for piezometers having unchanging boundaries, and a variable for auger-holes because the boundaries change with the water-level. In a piezometer, the hole is cased to a certain level, leaving

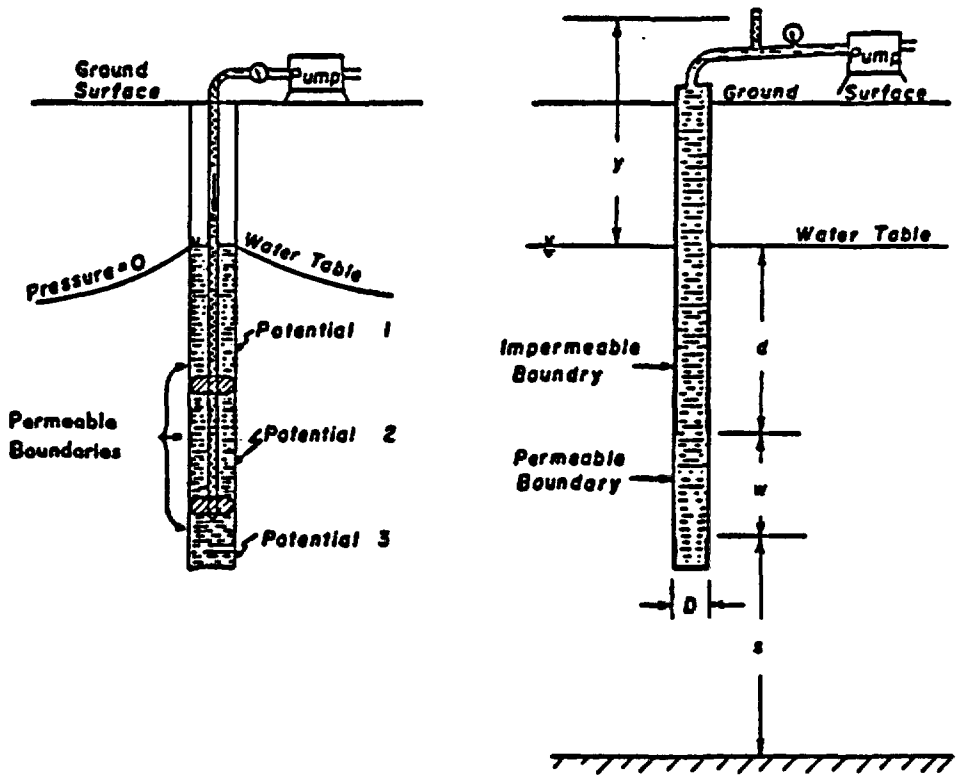

Fig. 1. (a) Common conditions of packer pump tests in rock. (b) Conditions of piezometer assumed in analysis of packer tests conducted in drill holes

a) Allgemeine Bedingungen beim Abpreßversuch in Bohrlochabschnitten. b) Schema eines Piezometers zur Analyse von abschnittweise vorgenommenen Abpreßversuchen in Bohrlöchern

a) Conditions générales à un essai de compression dans la roche. b) Schéma d'un piézomètre

open a cylindrical cavity of length w below. In rock pumping tests, water is conducted through drill rods to an open length of hole isolated by packers. Thus, the customary use of S-factors derived for cased holes, whose walls above and below the pumping cavity are streamlines (e.g., Thayer, 1962, p. 6), is at best an approximation of the actual conditions. The piezometer test could be more faithfully duplicated if tests were confined to the bottom of the hole, as is done in the Snowy Mts. Hydroelectric Authority, one packer only applied at various stages of completion of the hole. Better still, the unneeded upper part of the hole might be grouted or mud-filled above a drillable obstructor.

No rigorous solution is known or expected for packer tests, as they are currently practiced, for the hole above the cavity is either an equal-pressure surface if air-filled, equipotential if water-filled, or part one and part the other. Water levels within the hole are not customarily measured during tests. In Fig. 1 (a), schematically illustrating these tests, potentials 1 and 3 differ from the chamber potential 2, according to the length and conductivity of fracture paths short-circuiting the packers through the rock. The performance of tests sometimes discloses leaking packers.

Fig. 1 (b) portrays the assumed geometry that is used to analyze packer tests. It corresponds to piezometer tests described in the literature. The walls of the hole are no-flow boundaries except at the cavity. It is further assumed that the quantities of water injected are so small that the water-table remains unchanged.

If the test is applied above the water-table, there is displacement of air and water in a partially-saturated medium. Resistance and saturation increase with time.

The packer test currently gives empirical measures of discharge, believed useful as criteria for grouting needs and grout-take estimation (Talobre, 1957, p. 153; Grant, 1964: de Mello, 1960, p. 703), but the test gives a low-confidence measure of permeability. This is due, in part, to the assumptions discussed above, and in part, to the great variability of results common to most sites on rock. Improvement of methods and confidence is one object of this work.

The dimensionless variables describing the cavity geometry and determining the shape factor are expressed by:

$$S/D = f(d/D, w/D, S/D). \tag{4}$$

Frevert and Kirkham (1948) have established by electrical analogy that there is very little effect of lowered water table until d is less than one diameter, D, from the top of the cavity. The depth to an impermeable barrier, s, is seldom known in exploration, but can usually be assumed large in comparison to D. S/D is as insensitive to s/D as it is to d/D (Childs, 1952, p. 533). Thus, piezometer or packer tests are best analyzed as though in an infinite medium, provided that they are located below the water table. In such cases,

$$S/D = f(w/D). \tag{5}$$

In particular, if the cavity is long ($w/D > 8$)

$$S/D = \frac{2\pi w/D}{\ln(2w/D)} \text{ (Glover, reported by Zangar, 1946)*.} \tag{6}$$

Since the derivations of Dachler, Samsioe and Glover assume a line source, they fail to satisfy the condition of uniform potential over the surface of a cylinder. Maasland has provided, as alternative, the shape factors for ellipsoids.

* Zangar (1953) reports the derivation by Cornwell, but attributes the equation

Evans and Kirkham (1950) pointed out the analogy of the shape factor the electrostatic capacity about an ellipsoid in an infinite medium.

$$S = 4\pi C.$$

Smythe (1939) shows that

$$2/C = \int_0^\infty d\theta/[(\alpha^2 + \theta)(\beta^2 + \theta)(\gamma^2 + \theta)]^{1/2},$$

where θ is a variable of integration and α, β and γ are the semi-axes of an ellipsoid. For the ellipsoid inscribed in a packer cavity, $\alpha = \gamma$ and $\beta > \alpha$, giving:

$$S = 8\pi(\beta^2 - \alpha^2)^{1/2}/ln\left(\frac{\beta + (\beta^2 - \alpha^2)^{1/2}}{\beta - (\beta^2 - \alpha^2)^{1/2}}\right),$$

which becomes

$$S = 4\pi[(w/D^2 - 1]^{1/2}/ln\left(\frac{w/D + [(w/D)^2 - 1]^{1/2}}{w/D - [(w/D)^2 - 1]^{1/2}}\right), \tag{7}$$

upon substitution of

$$\alpha = D/2, \beta = w/2.$$

Shape factors computed by equation (7) differ by less than 3 percent from those computed by equation (6) if $w/D > 3.0$. As Maasland has noted (p. 273), neither of these equations are correct for a circular cylinder, though they are assymptotic to these values for large cavity lengths.

When a vertical piezometer coincides with the extraordinary axis of a two-dimensional anisotropic medium (Maasland, pp. 275–280), then the hydraulic conductivity

$$k_h = k_1 = k_2 \text{ and } k_v = k_3.$$

The transformation equations are

$$x_1' = x_1,\ x_2' = x_2,\ x_3' = m x_3,$$

m being $(k_h/k_r)^{1/2}$. Circular sections remain circular in the fictitious transformed medium, and the isotropic hydraulic conductivity is

$$k = (k_h k_v)^{1/2}.$$

Thus, the discharge is:

$$Q = (k_h k_v)^{1/2} S_a y, \tag{8}$$

where y is the head difference

and S_a is the anisotropic shape factor,

$$S_a/D = f(mw/D),$$

found by equations (6) or (7).

Maasland reports equations for shapes other than the long cylindrical cavities considered here. It is noteworthy that the principal conductivities of a two-dimensional anisotropic soil can be found if the principal directions are known to coincide with the axes of two differently-shaped piezometers. The combination of a long cylindrical cavity for one, and an open-ended disk source (no cavity) for [illegible] soil (Maasland, p. 279) but is inadequate for rock

because too few joint conductors (too small a sample) would communicate with the end of a drill-hole. Childs' two-well system does not readily lend itself to rock testing because large potential differences cannot be introduced by gravity.

Maasland also developed a means of analyzing three-dimensional anisotropy. His work served as a guide to the following but is not repeated here because it is not assumed that the axis of the piezometer coincides with a (vertical) principal axis of conductivity.

A rotation of the coordinate system is first necessary when the piezometer has an arbitrary orientation with respect to the principal axes of conductivity. Assume a drill-hole with orientation specified as B_i, the direction cosines of its

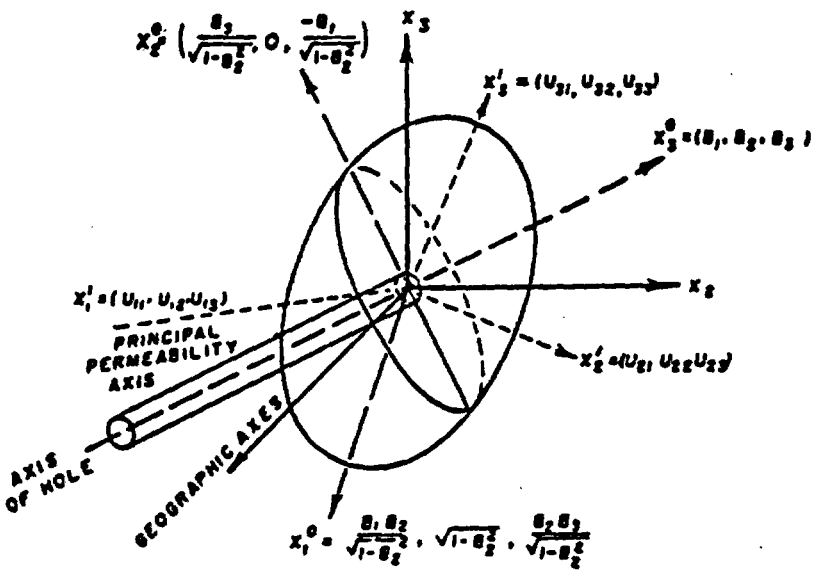

Fig. 2. Coordinate systems for packer tests in anisotropic media
Koordinatensystem beim Abpreßversuch im anisotropen Medium
Système de coordonnées à un essai de compression dans un milieu anisotrope

axis with respect to a right-handed geographic system (south $= x_1$, east $= x_2$, $up = x_3$), and three principal axes of conductivity with general orientation U_{ij}, similarly referenced.

Fig. 2 is a diagram of the unit vectors of three coordinate systems, two of them labeled with their direction cosines relative to the geographic axes x_i. In representing these, the superscript ^{0} signifies one of many possible coordinate systems having an axis along the cylinder; it has B_i as x_3^0 and x_2^0 is in the x_2-plane. The x_i' system coincides with the principal conductivity axes, U_{ij}, themselves being direction cosines in the x_i system. The origin is centered on the upper packer.

The equation of a right-circular cylinder with axis along the x_3^0 coordinate axis is:

$$x_1^{0^2} + x_2^{0^2} = r^2,\ r = D/2 \tag{9}$$

and the test section is limited to

$$0 \geq x_3^0 \geq -w.$$

The equation for the cylinder must be rotated from the x_i^0 system to the x_i' system. Each position vector is related, one system to the other, by a transformation

$$x_i^0 = = a_{ij} x_j', \tag{10}$$

whose matrix is defined by

$$a_{ij} = \begin{vmatrix} \cos(1'', 1') & \cos(1'', 2') & \cos(1'', 3') \\ \cos(2'', 1') & \cos(2'', 2') & \cos(2'', 3') \\ \cos(3'', 1') & \cos(3'', 2') & \cos(3'', 3') \end{vmatrix}.$$

Inspection of Fig. 2 will verify that the elements of the transformation are:

$$a_{ij} = \begin{vmatrix} \left[\frac{U_{11} B_1 B_2}{\sqrt{1-B_2^2}} - U_{12}\sqrt{1-B_2^2} + \frac{U_{13} B_2 B_3}{\sqrt{1-B_2^2}}\right] \\ \left[\frac{U_{11} B_3}{\sqrt{1-B_2^2}} - \frac{U_{13} B_1}{\sqrt{1-B_2^2}}\right] \\ [U_{11} B_1 + U_{12} B_2 + U_{13} B_3] \end{vmatrix} \quad \begin{vmatrix} \left[\frac{U_{21} B_1 B_2}{\sqrt{1-B_2^2}} - U_{22}\sqrt{1-B_2^2} + \frac{U_{23} B_2 B_3}{\sqrt{1-B_2^2}}\right] \\ \left[\frac{U_{21} B_3}{\sqrt{1-B_2^2}} - \frac{U_{23} B_1}{\sqrt{1-B_2^2}}\right] \\ [U_{21} B_1 + U_{22} B_2 + U_{23} B_3] \end{vmatrix} \quad \begin{vmatrix} \left[\frac{U_{31} B_1 B_2}{\sqrt{1-B_2^2}} - U_{32}\sqrt{1-B_2^2} + \frac{U_{33} B_2 B_3}{\sqrt{1-B_2^2}}\right] \\ \left[\frac{U_{31} B_3}{\sqrt{1-B_2^2}} - \frac{U_{33} B_1}{\sqrt{1-B_2^2}}\right] \\ [U_{31} B_1 + U_{32} B_2 + U_{33} B_3] \end{vmatrix} \tag{11}$$

The matrix multiplication of equation (10) gives the original components of a position vector in terms of the primed coordinates. Equation (9) for the cylinder in the coordinate system parallel to principal axes of the anisotropic medium, becomes

$$(a_{11} x_1' + a_{12} x_2' + a_{13} x_3')^2 + (a_{21} x_1' + a_{22} x_2' + a_{23} x_3')^2 = r^2. \tag{12}$$

To replace the medium by an imaginary isotropic one, we must transform linearly to a third coordinate system according to:

$$\begin{aligned} x_1'' &= (k_0/k_{11})^{1/2} x_1', \\ x_2'' &= (k_0/k_{22})^{1/2} x_2', \\ x_3'' &= (k_0/k_{33})^{1/2} x_3', \end{aligned} \tag{13}$$

where again, k_0 is an arbitrary constant. The k_{ii} are principal hydraulic conductivity coefficients, proportional to the principal permeabilities K_{ii}, and one of the factors listed in Table 1.

One possible definition of the arbitrary constant is

$$k_0 = (k_{11} k_{22})^{1/2}, \tag{14}$$

which makes

$$\begin{aligned} x_1' &= (k_{11}/k_{22})^{1/4} x_1'', \\ x_2' &= (k_{22}/k_{11})^{1/4} x_2'', \\ x_3' &= [k_{33}^{1/2}/(k_{11} k_{22})^{1/4}] x_3''. \end{aligned} \tag{15}$$

Table 1. Conversion Factors, Permeability to Hydraulic Conductivity

To obtain conductivity in: Name	Units	Multiply absolute cgs units (cm^2) by: Factor
Darcys	cm^2	$1.0132 \cdot 10^8$
Meinzer K_s	gal/day/ft^2 water at 60° F	$1.844 \cdot 10^9$
Field Units K_F	gal/day/ft^2 water at f°	$1.844 \cdot 10^9 \cdot \mu 60/\mu f$
	ft/year water at 60° F	$0.9053 \cdot 10^{11}$
	cm/sec water at 20.2° C	$0.9772 \cdot 10^5$
	meters/day water at 20.2° C	$0.861 \cdot 10^8$
Lugeon Units	l/min/m hole/Atmos over 10 min	$0.6 \cdot 10^{10}$ (approximately)

To find how the length of the cavity is changed by the transformation, identify the center of the distal end by the vector y_i, originally at

$$y_1^0 = y_2^0 = 0,\ y_3^0 = -w,$$

then rotated to

$$y_1' = a_{31}\, y_3^0,\ y_2' = a_{32}\, y_3^0,\ y_3' = a_{33}\, y_3^0,$$

and transformed to isotropy by substitution into equations (15) with $y_3^0 = -w$.

$$y_1'' = -(k_{22}/k_{11})^{1/6}\, a_{31}\, w,$$
$$y_2'' = -(k_{11}/k_{22})^{1/6}\, a_{32}\, w,$$
$$y_3'' = -[(k_{11}\, k_{22})^{1/6}/k_{33}^{1/3}]\, a_{33}\, w.$$

The cavity length in the isotropic system is found from

$$l^2 = y_i''\, y_i'',$$

which gives:

$$l = [(k_{22}/k_{11})^{1/3}\, a_{31}^2 + (k_{11}/k_{22})^{1/3}\, a_{32}^2 + \{(k_{11}\, k_{22})^{1/6}/k_{33}\}\, a_{33}^2]^{1/2}\, w. \qquad (16)$$

Direction cosines of the axis of the cylinder are:

$$Y_i = y_i''/l.$$

The general equation for the cylindrical cavity in the isotropic system is obtained by substituting equation (15) into (12), changing it to an oblique elliptic cylinder:

$$[(k_{11}/k_{22})^{1/3}\, a_{11}\, x_1'' + (k_{22}/k_{11})^{1/6}\, a_{12}\, x_2'' + \{k_{33}^{1/3}/(k_{11}\, k_{22})^{1/6}\}\, a_{13}\, x_3'']^2 + \qquad (17)$$
$$[(k_{11}/k_{22})^{1/3}\, a_{21}\, x_1'' + (k_{22}/k_{11})^{1/6}\, a_{22}\, x_2'' + \{k_{33}^{1/3}/(k_{11}\, k_{22})^{1/6}\}\, a_{23}\, x_3'']^2 = r^2.$$

A cross-section normal to its axis is also an ellipse, defining the new cavity shape by its semi-axes. To find them, we first solve the oblique section, equation (17), for its semi-axes, then project them to the plane normal to the cylinder axis. The expanded form of (17) is:

$$\frac{(k_{11}/k_{22})^{1/2}(a_{11}^2+a_{21}^2)}{r^2}x_1''^2+\frac{2(a_{11}a_{12}+a_{21}a_{22})}{r^2}x_1''x_2''+\frac{2(k_{33}/k_{22})^{1/2}(a_{11}a_{13}+a_{21}a_{23})}{r^2}x_1''x_3''$$
$$+\frac{(k_{22}/k_{11})^{1/2}(a_{12}^2+a_{22}^2)}{r^2}x_2''^2+\frac{2(k_{33}/k_{11})^{1/2}(a_{12}a_{13}+a_{22}a_{23})}{r^2}x_2''x_3''$$
$$+\frac{(k_{33}/(k_{11}k_{22})^{1/2})(a_{13}^2+a_{23}^2)}{r^2}x_3''^2=1. \tag{18}$$

The coefficients of $x_i x_j$, as arranged here, define a symmetric matrix after first dividing off-diagonal ($i \neq j$) elements by 2. Diagonalization transforms the equation of the oblique elliptic section to a coordinate system parallel to the axis of that ellipse:

$$\begin{vmatrix} A & 0 & 0 \\ 0 & B & 0 \\ 0 & 0 & C \end{vmatrix}$$

The diagonal matrix will contain only two non-zero terms, A and B, B and C, or A and C, which are coefficients of the ellipse

$$Ax_1''^2+Bx_2''^2+Cx_2''^2=1.$$

The semi-axes are, then, two of the following:

$$L_1=(1/A)^{1/2},\ L_2=(1/B)^{1/2},\ L_3=(1/C)^{1/2}.$$

The eigenvectors must next be determined, to define the orientations of the above semi-axes of the oblique elliptic section in terms of the transformed (isotropic) coordinate system. Call these axes l_i, m_i and n_i, corresponding to the A, B, and C eigenvalues. Fig. 3 illustrates the simple projection of these eigenvalues to the plane normal to the cylinder axis:

$$\alpha=L_1[1-(Y_i l_i)^2]^{1/2},$$
$$\beta=L_2[1-(Y_i m_i)^2]^{1/2},$$
$$\gamma=L_3[1-(Y_i n_i)^2]^{1/2},$$

whichever two are pertinent.

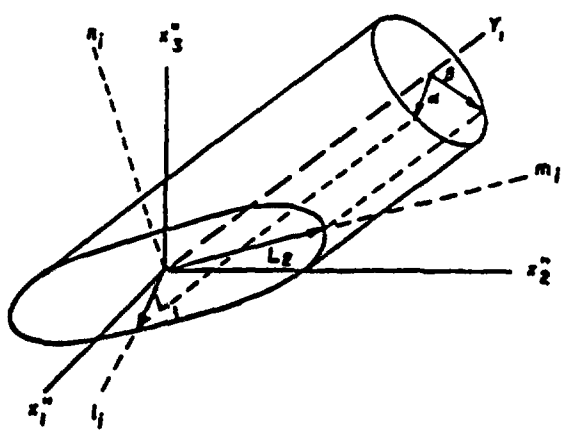

Fig. 3. The originally circular directrix of a cylinder is an oblique ellipse after transformation. The true directrix is found by projection along the axis Y_i

Umwandlungsfaktoren zur Umrechnung von Durchlässigkeit in hydraulische Leitfähigkeit. Der ursprüngliche Kreisquerschnitt eines Zylinders wird nach Transformation zu einer Ellipse. Der wahre Querschnitt wird durch Projektion in Richtung der Y_i-Achse gefunden

Facteur de transformation pour convertir la perméabilité à la conductibilité hydraulique. La section circulaire d'origine d'un cylindre est transformée à une ellipse. La section vraie est obtenue par projection en direction de l'axe Y_i

The greatest possible ellipticity would arise if the circular section in the original anisotropic medium coincided with the plane of k_{11} and k_{33}. Then

$$\alpha/\beta=(k_{33}/k_{11})^{1/2}.$$

We have described the elliptic cylinder in the fictitious isotropic medium by

radius $D/2$ of a right circular cylinder test section in an anisotropic medium. The ends of the cylinder are non-orthogonal after transformation. This will influence the shape factor when $w < D$, but may be neglected for pumping tests where w is invariably many times D.

The shape factor has been reduced to:

$$S D = f(k_{11}, k_{22}, k_{33}, \tfrac{1}{4}(k_{22}/k_{11})^{1/2} a_{12}^2 + (k_{11}/k_{22})^{1/2} a_{23}^2 + [(k_{11} k_{22})^{1/2}/k_{33}] a_{33}^2 w/D). \tag{19}$$

Maasland has studied the relation between ellipticity and the shape factor (1957, p. 244). Rather than evaluate the integral for electrostatic capacity for $\alpha \neq \beta \neq \gamma$, he employed electric analogues. He found little influence, provided that $w/D > 5$ and $1/3 < \alpha/\beta < 3$. Thus

$$S_a \cong f(l/D)$$

alone. S_a is determinable by equation (6) with less than 4 per cent error.

The limitation that k_{11}/k_{33} be less than 9 is serious only when a single, near-parallel joint set is present or dominant, for the orientation studies have indicated no cases of such strong anisotropy when more than one set of joints, in adequate samples, is present in the medium. The circular-cylinder form factor approximation is acceptable for two or three-set systems, unless, for instance, one set consists of large parallel faults, and the other conductors are tight joints. In some cases of strong anisotropy, problems may be solved by reducing to two dimensions on the plane of symmetry.

D should be the diameter of a circle having the same area as the elliptic section in the fictitious isotropic medium (Maasland, p. 284).

$$D = 2(\alpha\beta)^{1/2}. \tag{20}$$

The Glover-Cornwell equation for the shape factor of long cavities in an infinite medium is suitable for packer tests in rock, provided that w is replaced by l, equation (16), and D by equation (20). The conductivity must be determined by equation (2) and (14). Then equation (3) for the discharge is

$$Q = [(k_{11} k_{22})^{1/2}/k_{33}]^{1/2} S_a y. \tag{21}$$

A computation of discharge for one hypothetical packer test in a medium of known permeability will exemplify the method. Suppose that the diagonalized permeability tensor is

$$K_{ij} = \begin{vmatrix} 27.9 & 0 & 0 \\ 0 & 7.1 & 0 \\ 0 & 0 & 4.6 \end{vmatrix} . 10^{-6} \text{ cgs units}$$

and the matrix of direction cosines of the principal axes (row vectors) is:

$$U_{ij} = \begin{vmatrix} 0.632 & -0.770 & 0.081 \\ 0.564 & 0.386 & -0.730 \\ 0.531 & 0.507 & 0.678 \end{vmatrix}.$$

Suppose a 200-foot NX (D in equation [6] = 0.25 ft.) drill-hole is inclined 45 degrees east ($B_i = 0.0, 0.7071, -0.7071$) with one packer set 50 feet from the bottom ($w = 50$). The static water table is 40 feet below ground and the temperature [illegible] ($l_w = 40 + 75\,[2.311] = 213$ ft.).

Hydraulic conductivities are obtained by applying a factor from Table 1.

$$k_{ii} = K_{ii}(1.84 \cdot 10^{0}) \text{ gallons/day/ft}^2,$$

$$k_{11} = 5.15 \cdot 10^{4}, k_{22} = 1.31 \cdot 10^{4}, k_{33} = 0.85 \cdot 10^{4}.$$

Next, we compute the transformation matrix (equation [11]), that will rotate the drill-hole B_i to coordinates parallel to the principal conductivities.

$$a_{ij} = \begin{vmatrix} a_{11} & a_{12} & a_{13} \\ a_{21} & a_{22} & a_{23} \\ a_{31} & a_{32} & a_{33} \end{vmatrix} = \begin{vmatrix} 0.487 & 0.243 & -0.837 \\ -0.632 & -0.564 & -0.531 \\ -0.601 & 0.789 & -0.121 \end{vmatrix}.$$

The transformed test length has components

$$y_1'' = -(k_{22}/k_{11})^{1/4} a_{31} w = 0.710\,(0.601)\,50.0 = 21.2 \text{ ft.}$$

and similarly,

$$y_2'' = -(k_{11}/k_{22})^{1/4} a_{32} w = -55.6,$$

$$y_3'' = -[(k_{11} k_{22})^{1/4}/k_{33}^{1/2}]\, a_{33} w = 10.6.$$

The test length in the isotropic medium is given by equation (16) or

$$l = [(21.3)^2 + (55.6)^2 + (10.6)^2]^{1/2} = 60.1 \text{ ft.}$$

Direction cosines are

$$Y_i = 0.354, -0.924, 0.176.$$

The matrix of the cross-sectional ellipse is found by equation (18):

$$64.0 \begin{vmatrix} 1.263 & 0.475 & -0.058 \\ 0.475 & 0.190 & 0.039 \\ -0.058 & 0.039 & 0.321 \end{vmatrix}.$$

Upon diagonalization (see Long, 1961, p. 23), to slide-rule precision,

$$\begin{vmatrix} A & 0 & 0 \\ 0 & B & 0 \\ 0 & 0 & C \end{vmatrix} = \begin{vmatrix} 0.0 & 0.0 & 0.0 \\ 0.0 & 92.4 & 0.0 \\ 0.0 & 0.0 & 21.1 \end{vmatrix}.$$

The oblique elliptic section has the equation

$$92.4\,\bar{x}_2^2 + 21.1\,\bar{x}_3^2 = 1,$$

with semi-axes:

$$L_2 = 0.104, L_3 = 0.218 \text{ feet.}$$

To project these semi-axes to the plane normal to the axis of the cylinder, Y_i, the

l_2, and l_3. For each eigenvalue there are four simultaneous equations to satisfy, such as:

$$(1.263 - \lambda/64.0)\, l_1 + 0.475\, l_2 - 0.058\, l_3 = 0,$$
$$0.475\, l_1 + (0.190 - \lambda/64.0)\, l_2 + 0.039\, l_3 = 0,$$
$$-0.058\, l_1 + 0.039\, l_2 + (0.321 - \lambda/64.0)\, l_3 = 0,$$
$$l_1^2 + l_2^2 + l_3^2 = 1.$$

The solutions are direction cosines, the pertinent ones in this case being

$$m_i = 0.935, \quad 0.353, -0.036,$$
$$n_i = 0.029, -0.177, -0.984.$$

The cylinder axis Y_i makes angles with the semi-axes of the oblique ellipse having cosines

$$Y_i m_i = (0.354)(0.935) + (-0.924) \quad (0.353) + (0.176)(-0.036) = 0.001,$$
$$Y_i n_i = (0.354)(0.029) + (-0.924)(-0.177) + (0.176)(-0.984) = 0.001.$$

When such angles differ from 90 degrees, the projections of the semi-axis, L_i, into the plane normal to Y_i, give the semi-axes of the directrix of the transformed cylinder. In this case,

$$\beta = 0.104 \text{ ft.}$$

and

$$\gamma = 0.218 -$$

and $\beta/\gamma = 0.478$. Were the test oriented to attain the maximum ellipticity, then it would have been

$$\beta/\gamma = (k_{33}/k_{11})^{1/2} = 0.406.$$

Since $1/3 < \beta/\gamma < 3$, a circular cylinder will give a good approximation to the shape factor, if the circle diameter is taken to be:

$$D = 2\,(\beta\gamma)^{1/2} = 0.301.$$

Now we apply Glover's formula (6) for the shape factor of a long cylinder:

$$S_a = \frac{2\pi l}{\ln (2l/D)} = \frac{2\pi\, 60.1}{[2\,(60.1)/0.301]} = 145.0.$$

The hydraulic conductivity of the fictitious isotropic medium is

$$k = (k_{11}\, k_{22}\, k_{33}/k_0)^{1/3} = (k_{11}\, k_{22})^{1/3}\, k_{33}^{1/3} = 1.49 \,.\, 10^4 \text{ gal./day/ft}^2.$$

Then the discharge

$$Q = k\, S_a\, y,$$
$$= 1.49\,(145.0)\,213.0,$$
$$= 45\,850 \text{ gallons/day or}$$
$$= 32 \text{ gallons/minute.}$$

Such computations could be used for steady tunnel or power cavern seepage.

Three-Hole pump test for anisotropic media

If a piezometer or packer test hole is oriented parallel to one of the principal conductivity axes, this special case, discussed by Maasland (1957, p. 283), leads to equation (21).

The shape factor depends upon which axis is parallel to the drill-hole. It cannot be determined at the outset since the conductivities are unknown. Maasland's method for determining conductivities is adequate when the plane normal to the axis of the hole is one of isotropy, the hole following the unique axis. A more general method is presented below, for the case of three different principal conductivities of known direction.

To replace the real anistropic system with a fictitious isotropic one, a linear transformation only is required, since the hole already coincides with an axis. By equations similar to (13), we obtain

$$\begin{aligned} x_1' &= (k^0/k_{11})^{1/2} x_1, \\ x_2' &= (k_0/k_{22})^{1/2} x_2, \\ x_3' &= (k_0/k_{33})^{1/2} x_3, \end{aligned} \tag{22}$$

where the constant $k_0 = (k_{11} k_{22})^{1/2}$. The circular cross-section becomes an ellipse with axial ratios

$$\beta/\gamma = (k_{33}/k_{22})^{1/2}, \ \alpha/\gamma = (k_{33}/k_{11})^{1/2} \text{ or } \alpha/\beta = (k_{22}/k_{11})^{1/2},$$

depending upon which axis coincides with the hole, 1, 2, or 3, respectively. Before generalizing, let us assume that the hole follows the 3-axis, with 1 and 2 normal to the hole and $k_0 = (k_{11} k_{22})^{1/2}$. Then the semi-axes of the elliptic section in the transformed medium are

$$\alpha = (k_0/k_{11})^{1/2} D/2 \text{ and } \beta = (k_0/k_{22})^{1/2} D/2.$$

The circular section having the same area as the ellipse has diameter

$$D' = 2 (\alpha \beta)^{1/2} = D. \tag{23}$$

The cavity length w' in the fictitious isotropic medium is

$$w' = (k_0/k_{33})^{1/2} w = [(k_{11} k_{22})^{1/4}/k_{33}^{1/2}] w. \tag{24}$$

The shape factor defined by Glover's equation for a long cylindrical cavity gives a good approximation to that of an elliptical cylinder cavity if $1/3 < \alpha/\beta < 3$.

$$S_e/D' = \frac{2\pi w'/D'}{\ln (2 w'/D')},$$

$$S_e/D = \frac{2\pi (k_0/k_{33})^{1/2} w/D}{\ln \left(\frac{2 \{(k_{11} k_{22})^{1/4}/k_{33}^{1/2}\} w}{D} \right)}, \tag{25}$$

$$S_e = \frac{2\pi w (k_{11} k_{22})^{1/4}/k_{33}^{1/2}}{\ln \left(\frac{2 w (k_{11} k_{22})^{1/4}/k_{33}^{1/2}}{D} \right)}.$$

The discharge of such a piezometer or packer test in an anisotropic medium under head y is

$$Q = (k_{11}\,k_{22}\,k_{33}/k_0)^{1/2} S_e\, y = \frac{2\pi w y (k_{11}\,k_{22})^{1/2}}{\ln\left(\frac{2w}{D}(k_{11}\,k_{22})^{1/4}/k_{33}^{1/2}\right)}. \tag{26}$$

Interpreting field data, one can only assume isotropy and compute an apparent conductivity, k_{a3}, from

$$Q = k_{a3}\, S\, y,$$

where the shape factor is given by equation (6). Thus,

$$Q = k_{a3}\frac{2\pi w}{\ln(2w/D)}\, y. \tag{27}$$

Equating (26) to (27),

$$k_{a3}\frac{2\pi w}{\ln(2w/D)}\, y = \frac{2\pi w y (k_{11}\,k_{22})^{1/2}}{\ln\left(\frac{2w}{D}(k_{11}\,k_{22})^{1/4}/k_{33}^{1/2}\right)}$$

$$\frac{(k_{11}\,k_{22})^{1/2}}{k_{a3}} = \frac{\ln(2w/D) + \ln[(k_{11}\,k_{22})^{1/4}/k_{33}^{1/2}]}{\ln(2w/D)},$$

$$k_{a3}(1+e_3) = (k_{11}\,k_{22})^{1/2};\quad e_3 = \frac{\ln[(k_{11}\,k_{22})^{1/4}/k_{33}^{1/2}]}{\ln(2w/D)},$$

and similarly,

$$k_{a1}(1+e_1) = (k_{22}\,k_{33})^{1/2};\quad e_1 = \frac{\ln[(k_{22}/k_{11})^{1/4}]}{\ln(2w/D)}, \tag{28}$$

$$k_{a2}(1+e_2) = (k_{11}\,k_{33})^{1/2};\quad e_2 = \frac{\ln[(k_{11}/k_{22})^{1/4}]}{\ln(2w/D)}.$$

In equations (28), the logarithms may be taken to any base. The error term e tends to zero for such large w/D as apply to most packer tests in rock. Thus, an apparent conductivity, computed on the assumption of isotropy, approximates the geometric mean of the principal conductivities in directions normal to the hole. Reeve and Kirkham (1951) have already observed that the apparent conductivity depends largely upon the conductivity normal to the piezometer.

Inspection of equations (28) shows that for all w/D, k_a underestimates ($e > 0$) the geometric mean if the hole is drilled along a minimum conductivity axis, and over-estimates it if drilled along a maximum conductivity axis. If we limit consideration to media having $k_{11}/k_{22} < 9$, then cavities that are elliptical in the transformed medium can be adequately analyzed as equivalent circular cylinders.

We can label k_{a1}, k_{a2}, and k_{a3} the apparent hydraulic conductivities determined by three orthogonal piezometers or packer tests, each drilled parallel to a principal axis, 1, 2, or 3. As a first approximation:

$$k_{a1}^2 = k_{22}\,k_{33};\quad k_{a2}^2 = k_{11}\,k_{33};\quad k_{a3}^2 = k_{11}\,k_{22}.$$

Solved simultaneously,

$$k_{11} = k_{11}\,k_{22}/k_{a3};\quad k_{22} = k_{a1}\,k_{a2}/k_{a3}. \tag{29}$$

With these estimates, one can find by (28) the errors made in assuming k_{a1}, k_{a2}, k_{a3} to equal the geometric means of conductivities normal to each test hole. Corrected values of k_a yield improved principal conductivities by equation (29). Two or three consecutive corrections will converge on the true values.

A truly general in-situ piezometer test is yet to be devised. The present method, as well as those of Frevert and Kirkham (1948), Luthin and Kirkham (1949), Reeve and Luthin (1957), Childs (1952) and Maasland (1957) require independent knowledge or assumptions of the principal directions of hydraulic conductivity. The assumed uniqueness of the horizontal plane is usually justifiable for agricultural soils or stratified, unconsolidated deposits (Childs, 1952, p. 527; Maasland, 1957, p. 228), but even Childs' two-well system requires trial field arrangements to find maximum and minimum conductivity directions in the horizontal plane.

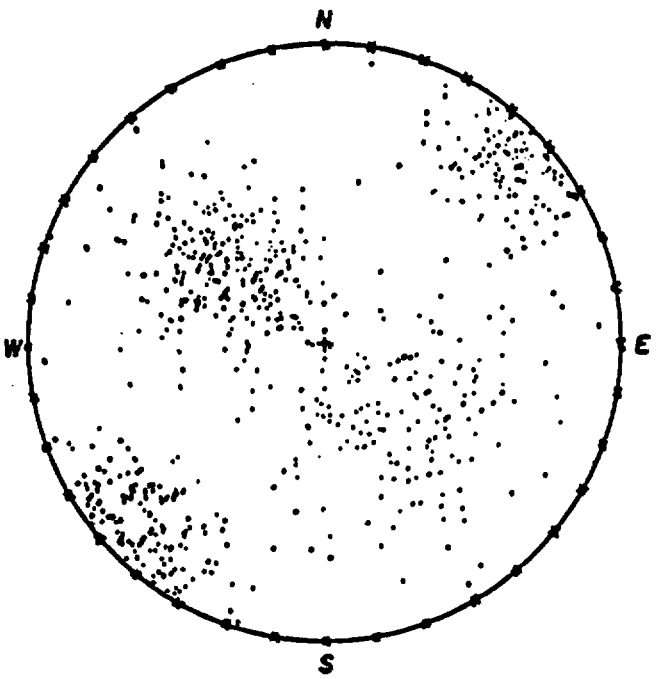

Fig. 4. Stereographic projection, upper hemisphere. Three normal joints sets with same spacing, different dispersions: $K_f = 6$, dip. 45 deg. SE; $K_f = 15$, dip. 45 deg. NW and $K_f = 30$, dip. 90 deg. SW; K_f is Fisher's (1953) dispersion coefficient

Stereographische Projektion, obere Halbkugel: drei Kluftscharen mit gleichen Abständen und verschieden starker Streuung: $K_f = 6$, Fallen 45° SE; $K_f = 15$, Fallen 45° NW, und $K_f = 30$, Fallen 90° SW; K_f ist der Streuungskoeffizient nach Fisher (1953)

Projection stéréographique, hémisphère supérieure. Trois familles de fissures normales à distances égales avec dispersion différemment grande

In the general case of anisotropy, there are six independent unknowns, three to define the orientation of axes, and three to define principal conductivities. A single determinative test for these variables would, in all likelihood, be too complex for practical use. It is thought better to continue use of other criteria for recognition of principal axes before applying a test for the three conductivities.

Such a test is the three-hole arrangement described above, also the two-well and short piezometer combination of Childs (1952). In practice, a test with three holes uniquely oriented will often prove inconvenient because of terrain limitations. Furthermore, exploratory holes drilled primarily for purposes other than pumptesting, oriented for convenience or economy between principal axes, would not be useful for analyses of this sort. Usually, some latitude of choice exists, for diamond-drill explorations are somewhat arbitrary in design, especially in preliminary stages. For purpose of permeability testing, they could be better oriented than is customary, concurrently disclosing other geological unknowns. When seepage or potential distribution is the prime problem, the entire layout should be oriented according to predetermined conductity directions.

The geometry of the system of joint sets, faults, shears, foliation and bedding determined from surface or tunnel exposures provides the only initial indication of the orientation of principal directions. A sterconet plot of joint normals offers the best tool for visualizing the symmetry of systems, and for measuring average

A principal plane lies normal to two conjugate joint sets, and the approximate angle of a principal axis between two unequal sets can be determined by their relative spacing, aperture distribution or orientation dispersion. Progressive analysis of tests and bore-hole photographs during the drilling program should normally give improved definition of axes to improve hole orientations.

As a hypothetical example of anisotropic analysis procedure, consider a foundation rock whose surface expression of jointing reveals a pattern such as is displayed in the stereonet plot of normals, Fig. 4. Three orthogonal but unequal sets are apparent. NX diamond-drill holes are then ideally inclined 45 degrees northwest and southwest, and horizontally, NE–SW, so that each coincides most faithfully with the central tendency of a joint set. Pumping tests with packers are performed as drilling progresses. For each test, discharge, static water level and gage pressure are measured, with packers set at intervals of about 25 feet. Hydraulic conductivity is computed for each test, assuming isotropic conditions, and the results for each orientation are averaged. Let these be:

$$k_{a_1} = 1.6 \cdot 10^4;\ k_{a_2} = 2.1 \cdot 10^4;\ k_{a_3} = 3.3 \cdot 10^4 \text{ gal./d. ft}^2,$$

where subscript $_1$ refers to holes dipping NW, $_2$ for holes dipping SE, and $_3$, horizontal.

According to equations (29),

$$k_{11} = k_{a_2} k_{a_3}/k_{a_1}' = 4.3;\ k_{22} = k_{a_1}' k_{a_3}/k_{a_2} = 2.5;\ k_{33} = k_{a_1} k_{a_2}\ k_{a_3} = 1.0.$$

Clearly, the direction dipping 45 degrees NW is most conductive, as might be guessed from the large number of joints parallel to this direction. The horizontal, NE–SW direction is least conductive, since fewest joints trend or intersect along this line.

Now, we can enter equations (28) with $w/D = 25/0.25 = 100$ and the above estimates. The errors that apply to

$$k_{a_3}(1 + e_3) = (k_{11} k_{22})^{1/2}, \text{ etc.}$$

are obtained

$$e_1 = -0.026;\ e_2 = 0.026;\ e_3 = 0.112.$$

Corrected, harmonic means of conductivities normal to each hole alignment are:

$$k_{a_1}' = k_{a_1}(1 + e_1) = 1.6\,(1 - 0.026) = 1.56 \cdot 10^4.$$

$$k_{a_2}' = k_{a_2}(1 + e_2) = 2.1\,(1 + 0.026) = 2.15,$$

$$k_{a_3}' = k_{a_3}(1 + e_3) = 3.3\,(1 + 0.112) = 3.7$$

and by equation (29):

$$k_{11} = 5.1;\ k_{22} = 2.7;\ k_{33} = 0.91 \cdot 10^4.$$

Again obtaining anisotropies, errors, corrected geometric means and principal conductivities, we find:

$$k_{11} = 5.2;\ k_{22} = 2.7;\ k_{33} = 0.90 \cdot 10^4.$$

Further re-estimates are unnecessary, since these values are close to the asymptotes of the principal conductivities.

Bibliography

Billings, M. P. (1942): Structural Geology. Prentice-Hall, Inc., 473 pp.

Childs, E. C. (1952): The measurement of hydraulic permeability of saturated soil in situ. I. Principles of a proposed method. Proc. Royal Soc., London, Ser. A, vol. 215, pp. 525–535.

Collins, R. E. (1961): Flow of fluids through porous materials. Reinhold Publ. Co., New York. 270 pp.

Dachler, R. (1936): Grundwasserströmungen. Springer, Vienna.

Davis, S. N. (1963): Hydrologic and geologic evaluation — Nevada test site, Interim Report. Hazleton-Nuclear Science Corp., Palo Alto, Calif., Unpubl., 25 pp.

Davis, S. N. and L. J. Turk (1964): Optimum depth of wells in crystalline rocks. Groundwater, vol. 2, no. 2, pp. 6–11.

De Mello, V. F. B. (1960): Some quantitative investigations on curtain grouting in rock foundations of earth dams. Proc. 1st Pan-Am. Conf. on Soil Mech. and Foundation Eng.

Elkins, L. F. and A. M. Skov (1960): Anisotropic spread of pressure transients delineates Spraberry fracture orientation. Trans. Amer. Inst. Min. and Met. Eng. vol. 219, p. 407.

Evans, D. D. and D. Kirkham (1950): Measurement of air permeability of soil in Soil Sci. Soc. Amer., Proc., vol. 14, pp. 65–73.

Fisher, R. A. (1953): Dispersion on a sphere. Proc. Royal Soc., London, Ser. A, vol. 217, pp. 295–306.

Frevert, R. K. and D. Kirkham (1948): A field method for measuring the permeability of soil below a water table: Proc. Hwy. Res. Bd., vol. 28, pp. 433–442.

Grant, L. M. (1964): Application of the unit take concept in evaluating grout hole drilling methods. Eng. Geology, vol. 1, no. 1, pp. 52–67.

Hvorslev, M. J. (1951): Time lag and soil permeability in ground-water observations. Bull. 36, Waterways Exper. Sta., Corps Eng. U. S. Army, Vicksburg, Miss.

Kirkham, D. (1945): Artificial drainage of land. Streamline experiments. The Artesian Basin, III. Trans. Amer. Geophys. Un., vol. 26, pp. 393–406.

Landrum, B. L. and P. B. Crawford (1960): Effect of directional permeability on sweep efficiency and production capacity. Trans. Amer. Inst. Min. and Met. Eng., vol. 219, p. 301.

Luthin, J. N. and D. Kirkham (1949): A piezometric method for measuring permeability of soil in situ below a water table. Soil Sci., vol. 68, pp. 349–358.

Lyons, M. S. (1960): Phase IV, Basic data compilation, Joint study, underground power plant, Oroville Dam site. Calif. Dept. of Water Resources, Unpubl. Rept., 3 pp, 14 figs.

Maasland, M. (1957): Soil anistropy and land drainage, in: Drainage of agricultural lands, J. N. Luthin, Ed. Amer. Soc. Agronomy, Madison, Wisc., pp. 216–285.

Reeve, R. C. and J. N. Luthin (1957): Methods of measuring soil permeability, in: Drainage of agricultural lands, J. N. Luthin, Ed. Amer. Soc. Agronomy, Madison, Wisc., pp. 395–445.

Richardson, J. T. (1948): Summary of uplift pressures at Bureau of Reclamation dams. U. S. Bur. of Reclam. Techn. Memo. 636, p. 16.

Samsioe, A. F. (1931): Einfluß von Rohrbrunnen auf die Bewegung des Grundwassers. Zeitschr. Angew. Math. und Mech., Heft 2, S. 124–135.

Scheidegger, A. E. (1960): The physics of flow through porous media. The Macmillan Co., New York. 313 pp.

Smythe, W. R. (1939): Static and dynamic electricity. McGraw-Hill Book Co., New York, 2nd Ed., 360 pp.

Snow, D. T. (1965): A parallel-plate model for permeable fractured media. Unpubl. Ph. D. thesis, Univ. of Calif., Berkeley, Calif., 331 pp.

Snow, D. T. (1967): Anisotropy of permeable fractured media, in: Hydrology and Flow through Porous Media (The Muskat Volume). R. J. M. De Wiest, Ed., Academic Press. New York, 86 pp. (in press).

Stuart, W. T. (1935): Pumping test evaluates water problem at Eureka, Nev. Min. Eng., vol. 7, no. 2, pp. 148–156.

Talobre, J. (1957): La Mechanique des Roches. Dunod, Paris, 444 pp.

Terzaghi, K. (1962): Does dam foundation engineering really lag? Eng. News-Record, Feb. 15, p. 58.

Thayer, D. P. (1962): Interim Report, Permeability study, underground power plant, Oroville Dam, Calif. Dept. of Water Resources, Unpubl. Rept., 14 pp., 17 figs. and tables.

Turk, J. L. (1963): The occurence of ground water in crystalline rocks. Unpubl. M. S. Rept., Stanford Univ., 42 pp., 26 tables.

Vreedenburgh, C. G. F. (1936): On the steady flow of water percolating through soils with homogeneous-anisotropic permeability. Proc. Intn'l. Conf. Soil Mech. and Foundation Eng., pp. 222–225.

Wahlstrom, E. E. and V. Q. Hornbach (1962): Geology of the Harold D. Roberts Tunnel, Colorado, West Portal to Station 468-40. Bull. Geol. Soc. Amer., vol. 73, no. 12, pp. 1477–1498.

Yokota, J. (1963): Experimental studies on the design of grouting curtain and drainage for the Kurobe No. 4 Dam. Felsmechanik und Ingenieurgeologie, vol. 1, no. 2, pp. 104–119.

Zangar, C. N. (1953): Theory and problems of water percolation. Eng. Monograph 8, U. S. Bur. Reclam., Denver, Colo., 76 pp.

Zangar, C. N. and H. B. Phillips (1946): Electric analogy conductivity tests for percolation out of wells. Memo to T. P. Ahrens, U. S. Bur. Reclam., Denver, Colo.